A generalised LES series approach for the modelling of premixed and non-premixed combustion

Weilin Zeng

Department of Mechanical Engineering

Supervised by

Professor Kai Luo

Dr Konstantina Vogiatzaki (University of Brighton)

A dissertation submitted in partial fulfilment

of the requirements for the degree of

Doctor of Philosophy

of

University College London

2019

Declaration

I, Weilin Zeng, confirm that the work presented in this thesis is my own. Where information has been derived from other sources, I confirm that this has been indicated in the work.

Signature:

Date:

Abstract

The research in this work aims to derive and develop an innovative series combustion sub-grid model into a robust and reliable modelling technique in the context of LES for turbulent flames. This method is a mathematical approach, and capable of predicting both premixed and non-premixed combustion regimes. The model also has the correct limiting behaviour, approaching DNS as the filter size approaches Kolmogorov scales.

In the first part of the research, the mathematical derivation of the series model is addressed and the simulation features are described. Relevant aspects about the numerical implementation are unfolded, and the potential error sources are identified.

In the second part of the work, the applications to full scale test cases are presented: i) a series of non-premixed piloted methane jet flames (Sandia Flames D and F), ii) a premixed methane piloted Bunsen jet flame and iii) a bluff-body stabilised propane premixed flame. The investigated cases involve both premixed and non-premixed combustion regimes and display complex phenomena encountered in practical combustors (flame anchoring, recirculation zones and shear layers). Subsidiary non-reacting simulations are performed for the third case to guarantee a sufficient grid resolution for the turbulent flow field.

The findings of this work demonstrate that the series model is an efficient and robust technique to predict turbulent premixed and non-premixed combustion regimes and the combustion dynamics in the context of large eddy simulation. Due to the features of no extra parameters and correct limiting behaviours, the model can be easily incorporated into other established LES programming framework.

Keywords: Series model; Large eddy simulation; Sub-grid chemical source term; premixed turbulent combustion; non-premixed turbulent combustion.

Impact Statement

An efficient and economical computational method is always of pressing need during the industrial design process. However, an accurate prediction from a computational method usually means high computational expense. Particularly in the areas of combustion and fluid mechanics, Navier-Stokes equations are notoriously difficult for finding accurate solutions.

To reconcile the conflicts between accuracy and expense, an effective and economical method is proposed in the present study. By using the method, the Navier-Stokes equations can be solved efficiently without losing the accuracy. From an academic point of view, this work will help maintain UK excellence in computational combustion. From an end-user importance point of view, this work will be of interest to a wide range of research institutes and industrial companies in the UK (e.g. engine industry), as it will contribute to the reduction of cost during the design process.

Acknowledgements

Firstly, I sincerely thank Prof. Kai Luo, the greatest supervisor, for his intelligence, passion and patience in advising my research. The past four years witnesses how I grew up from a rookie in research to a PhD candidate under his supervision. It is really an honour to be a student of him.

My special thanks are to my co-supervisor Dr Konstantina Vogiatzaki, who patiently guided me with every step of the model development, who enthusiastically encouraged me from early failures, who strictly pointed out the places where I need to improve. I feel lucky to be working with her all these years, and her devotion and attitude to research is my lifelong example.

I am also very grateful to Dr. Salvador Navarro-Martinez for his enlightenment on my research and great help with my model problems. His expertise in theory and modelling is fantastic and every conversation with him benefits me a lot. It is really a great pleasure to work with him.

I would like to thank my friends and colleagues, Dr Jiang Xizhuo, Dr Chen Zhuyang, Miao Feng, Ren Kang, Dr Wang Xujiang, Liu Jinhao, Gu Xuyi, Arthur, Dr Jeremy Nohan, Dr Daniel Baeriswyl, Dr John Vardakis, and Mariana Covarrubias Castro.

Most important, I would like to thank my parents, for their love and understanding for me. Last but not least, my gratitude is for my grandma and late grandpa, who gave me their warmest love.

Finally, I would like to acknowledge the support from Dean’s Prize Scholarship from the Faculty of Engineering Sciences, University College London and China Government Scholarship from China Scholarship Council.

To my grandma and late grandpa

Contents

List of Figures

List of Tables

Nomenclature

Roman Symbols

A	Thermal conductivity coefficient (-)
c	Species mass concentration (mol*kg^{-1})
C_{sgs}	Sub-grid coefficient (mol*kg^{-1})
C_{ϵ}	Model coefficient (-)
D	The species diffusion coefficient (-)
Da	Damköhler number (-)
Ea	The activation energy (kj/mol)
$\widetilde{e_{ij}}$	The rate of strain tensor
G	The filter kernel

$G(x,t)$	G-equation scalar field
g_i	The body forces (N)
H	Side length (m)
hrs	Hours
Ka	Karlovitz number (-)
k_b^j	The rate coefficient for the backward reaction (-)
k_f^j	The rate coefficient for the forward reaction (-)
L	Characteristic length scale of the flow (m)
Ma	Mach number
p	The static pressure (Pa)
Pr	The Prandtl number (-)
$\dot{q}$	The heat source term
q_j	The diffusive flux

Re	Reynolds number (-)
Sc	Schmidt number (-)
S_T	SGS turbulent flame speed
S_L	Laminar flame speed
t	Time (s)
T	Temperature (K)
U_{in}	Inlet bulk velocity (m/s)
u_j	The velocity component in the j-th direction (m/s)
$V_{\alpha,j}$	The diffusion velocity of species α (m/s)
$v_b^{\alpha j}$	Molar stoichiometric coefficient of species α in reaction j (right)
$v_f^{\alpha j}$	Molar stoichiometric coefficient of species α in reaction j (left)
W	The molecular weight (-)

x_j	The spatial vector (m)
Y	Species mass fraction (-)
Z	Mixture fraction in flamelet model (-)

Greek Symbols

α	Chemical species
δ_L	The laminar flame speed
δ_{ij}	The *Kronecker symbol*
Δ	The filter size
η	The flame thickness
μ	The dynamic viscosity (N*s/m2)
υ	The kinematic viscosity (m2/s)
υ_{SGS}	The SGS eddy viscosity

ρ	Density (kg/m3)
Σ_{Δ}	The SGS flame surface density
τ_{ij}	The viscous stress tensor
τ_{ij}^{SGS}	The SGS stress tensor
φ_k	Field scalar
ϕ_{α}	Reactive scalar
χ	Scalar dissipation rate
$\dot{\omega}(c)$	Chemical source term
Ω	The flow domain

Subscripts

0	Stagnation property

i, j, k	Vector components
in	Inlet parameter
l	Laminar state
t	Turbulent
b	backward
f	forward

Accents

$\bar{}$	Filtered quantity
$\tilde{}$	Favre filtered quantity
´	Fluctuating quantity

Acronyms

ADEF	Approximate Deconvolution and Explicit flame Filtering
ARM	Augmented reduced mechanism
CFD	Computational fluid dynamics
CMC	Conditional moment closure
DNS	Direct numerical simulation
ESF	Eulerian stochastic field method
FDF	Filtered density function
LDV	Laser Doppler velocimetry
LES	Large eddy simulation
PaSR	Partially stirred reactor
PISO	Pressure Implicit with Splitting of Operator
PDF	Probability density function

RANS	Reynolds-averaged navier–stokes
RMS	Root mean square
RHS	Right-hand side
SIMPLE	Semi-Implicit Method for Pressure-Linked Equations
SFS	Sub-filter-scale
SGS	Sub-grid scale

1 Introduction

1.1 Motivation and background

The history of humankind utilising combustion dated back to Stone Age, when ancestors used fire for warmth, protection, and cooking food. In 1781, James Watt invented his steam engine, thrusting Industrial Evolution all over Great Britain and the rest of the world. Ever since, combustion entered the horizons of engineers and researchers, as it occurs significantly in propulsion and energy systems, such as internal combustion engines in vehicles, gas turbines in aeroplanes, and industrial furnaces in power plants. Despite its prevailing role, new concerns arise simultaneously due to the heavy consummation of fossil fuels and the inevitable pollution of combustion products. The Paris Agreement in 2015 emphasised the significance of mitigating global warming and imposed worldwide contribution to reducing the emission of greenhouse gas. Except for the United States, Syria, Nicaragua, all nations in this planet have joined and pledged to protect the future of the Earth. To cater to the needs of pollution reduction and maintain the development of sustainability and efficiency, the combusting process should be comprehensively perceived.

Intrinsically, combustion falls into 3 regimes:

1) *Non-premixed.* In non-premixed combustion, fuels and oxidisers enter the reaction zone separately. Since mixing is perfectly sufficient and the burning speed is slower, it is easier to control but more soot is produced in this process. Diesel internal combustion engines are one of its typical applications.

2) *Premixed.* As to premixed combustion, reactants are mixed at the molecular level before ignition. In this regime, chemical reactions can occur everywhere and the flame is propagating, so that it is more difficult to harness and is subject to safety issues such as flame flashback. In spite, as the fuel and oxidiser is well defined, clean combustion is likely to be achieved in this mode, especially by means of lean mixtures. In this regard, premixed combustors or burners are a promising tendency.

3) *Partially premixed.* Partially premixed is regarded as a regime where non-premixed and premixed combustion happens simultaneously. The interactions between these two burning modes are less academic, but it shows great potential of greater efficiency and lower emission. Direct-injection compression-ignition in internal engines is a typical technology in this regime.

Above all, in most practical combustors, combustion does not appear alone, but is strongly coupled with turbulence, a fluid motion characteristic of random and chaotic 3-dimensional vortices. Turbulent vorticity modifies the structures of the flame, acting the role of enhancing mixing processes and boosting the chemistry reaction rate; over-intense turbulence may prevent the chemical reaction, resulting in flame quenching, a phenomenon concerning stability and efficiency in aeroplane engines or other large-scale combustors. In return, heat

release from the flame changes turbulence intensity through altering the kinematic viscosity. Besides, the geometry of most combustion chambers in practical combustors is complex, and different stabilising methods are employed. Due to a large number of complexities introduced by the diversified shapes of combustors and the combustion modes in these apparatuses, the turbulent reacting flows consist of an extensive range of time and length scales.

Figure 1.1 Countries that joined the Paris Climate Agreement (Source: UNFCCC)

A throughout and deep comprehension of the interactions between flames and vortex involved in turbulent combustion is essential to designing efficient combustors and necessitates the development of fundamental theories and the accumulation of investigation knowledge. To date, experimental observations are the most regularly used methodology to research turbulent combustion. Both laboratory burners and industrial combustors are investigated all across the centuries, affording abundant data for solving various practical problems

and contributing to the advancement of combustion theories. With the huge development of high-performance computing in recent decades, CFD (Computational Fluid Dynamics) is becoming an increasingly reliable and widely used approach to understand turbulent combustion mechanisms. Complementing experimental research, CFD provides a comprehensive sight into the intricate processes in the combustion chambers.

The first applicable CFD technique in history is RANS (Reynolds-averaged Navier–Stokes), whose basic concept is to average the instantaneous governing equations and close the fluctuating quantities with models(Favre, 1969). It has been widely practised in the industry due to its low computational requirement (Poinsot and Veynante, 2005). However, the complexity of flows in modern combustors restricts its accuracy, and lack of fluctuation information is another drawback in essence. On the contrary to RANS in methodology, DNS (Direct Numerical Simulation) resolves the full instantaneous governing equations without any turbulence model, thus all turbulence scales are explicitly captured with their impacts on combustion. Nevertheless, it is not affordable for industrial geometry as the computational cost is enormous. The present implementation is still limited to simple academic flows.

To compromise the conflicts between RANS and DNS, LES (Large Eddy Simulation) was invented, where a spatial or spectral filter is employed to the governing equations. Thanks to it, large scales motions are separated from the scales under the filter size, where the modelling is required. Figure 1.2 outlines the distinct features of these 3 CFD approaches.

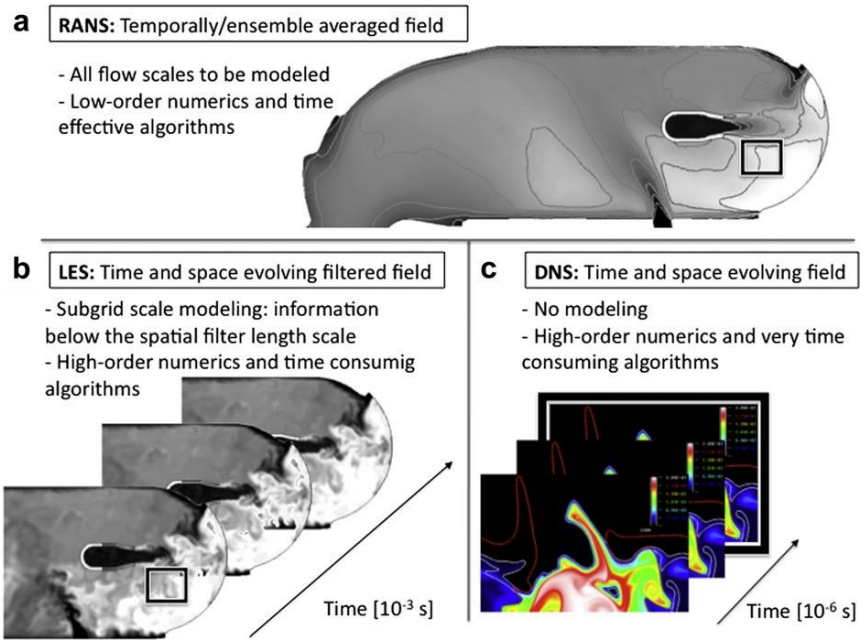

Figure 1.2 Features of RANS(Boudier et al., 2007), LES(Boudier et al., 2008) and DNS(Jiménez et al., 2002) (source: (Poinsot and Veynante, 2005))

1.2 State-of-the-art combustion models

To date, Large Eddy Simulation (LES) stands for one of the most prospective technology for the investigation of the turbulent reacting flows, especially in complex chamber geometries. With the technological advancement of high-performance computing facilities, LES has been opened an entrance to industrial practice. The key to applying LES into a reliable and accurate tool for industrial combustors is the development of precise sub-grid models for turbulent combustion. In spite that a large proportion of fluid motions are resolved straight, the influence of the sub-grid scale is significantly non-negligible in reacting flows, as combustion predominantly takes place below the

unresolved scales(Prasad, 2011). Up to now, numerous sub-grid models have been established by various researchers to probe into the interactions between turbulence and flame at the unresolved level. According to the classification of (Poinsot and Veynante, 2005, Giacomazzi et al., 2004, Gicquel et al., 2012), State-of-the-art turbulent combustion models can be categorised into 3 groups.

1.2.1 Geometric approaches

In these methods, a propagation formation is rearranged for the governing equation and sub-grid terms are modelled in consideration of the combustion modes based on the turbulent Reynolds numbers, Karlovitz number and Damköhler number. Usually, in these models, the flamelet assumption is employed: the chemical reaction happens in a thinner region than turbulence length scales and merely the effects of curvature, wrinkling and stretch influence the filtered reaction rate in the formulations of iso-c or iso-Z. In this category, the concept of flame wrinkling factors, or flame surface density can also be brought in to assess the filtered reaction rate. Both methods need the statistics of the inner structure of flames and its chemistry.

Another popular approach is artificially thickened flame, where the interaction between chemistry and transport is intentionally altered to acquire a thickened flame, which becomes resolved in the LES grids. In detail, the coefficient of turbulent transport is amplified by a specific factor. To maintain the consistency of the flame speed, the chemical source term should be shrunk by the same coefficient. Although this approach solves the thickened flame, the interaction

between combustion and turbulence is transformed from a transport-oriented combustion regime to a chemistry-oriented one, and the impact of the heat release on the flow field is hardly to be manifested sufficiently. In order to overcome it, a dynamic procedure is applied to determine the model parameters, and it has be proven to be more robust than the use of a constant factor (Wang et al., 2011, Volpiani et al., 2016, Rochette et al., 2018).

Up to now, the models in this approach remain active academically and industrially, since they are well established and refined as many are originally inherited from RANS combustion models. On the other hand, these models are on a large scale subject to the geometrical assumptions, so that the application is constrained to one fixed combustion mode, either premixed or non-premixed regime, in terms of code formalism. In addition, these models may not deal with the partially premixed regime wisely.

1.2.2 statistical models

In this category, sub-grid terms can be established via Probability Density Function (PDF) or the Filtered Density Function (FDF) in the incorporation of the filtering procedures. The main benefit of this formation is that the unsolved information can be attained with direct integration of the FDF or PDF. Under this notion, the approach can be divided into two distinctive sub-approaches.

The presumed method. In this approach, the PDF or FDF form is determined a priori and regularly the parameters employ the local quantity of the filtered value and its second filtered central moments. The conventional shapes of presumed

PDF are the beta, Gaussian, delta, and Log-normal functions. This design has been practised in the study of coal combustion(Rieth et al., 2017), partially premixed combustion(Knudsen and Pitsch, 2015), and others(Sewerin and Rigopoulos, 2018, Donini et al., 2015, Lapointe and Blanquart, 2017).

Under the same concept, the Conditional Moment Closure (CMC) model is another popular and successful realisation, where the filtered conditional terms in the transport equations can be multiplied by a presumed density function and the assessments of the sub-grid unsolved value can be generated after the integration procedures. Note that some of the conditional terms can be presented in the evolution equation. In recent years, CMC techniques have been put into use in a wide range of combustion simulations, like homogeneous charge compression ignition (Salehi et al., 2015, Salehi et al., 2017), swirling and bluff body stabilized non-premixed flames (Zhang et al., 2015, Triantafyllidis et al., 2009, Navarro-Martinez and Kronenburg, 2009), and other sophisticated combustion phenomena(Ma and Devaud, 2015, Labahn et al., 2017, Roy et al., 2015).

The transported FDF/PDF model. In this method, the evolution equations of the functions are directly resolved, and the integrating procedures of the estimated density function are executed to provide statistics for the filtered unsolved terms in the transport equations. This approach has also been applied to various kinds of combustion problems in this decade (Kuron et al., 2017, Chishty et al., 2018, Zhang and Wang, 2018, Hu et al., 2017).

In particular, Eulerian stochastic field method is the innovation and development of the transported PDF model, where the equation describing the evolution of the PDF is solved using the Eulerian stochastic fields(Mustata et al., 2006). The researchers from Imperial College London(Jones and Navarro-Martinez, 2008) and Lund University(Hodzic et al., 2017) contributed a lot to the realisation and development into large eddy simulation environment. For the past 10 years, it has been practised into many complicated combustion research (Jones et al., 2015, Gallot-Lavallée et al., 2017) and the modelling of industrial or industrial-like gas turbine engines(Jones et al., 2014, Jones et al., 2012, Bulat et al., 2014).

The development of statistical models related to PDF or FDF has been a rapid track in recent two decades, and its popularity are growing in research institutions and industrial companies. These models are on the ground of the transport or evolution equations of sub-grid density functions, where the scalar information is kept. Owing to this benefit, these methods are free from the constraining to one specific combustion regime, compared with geometric approaches. It also shows the potential of coping with complex combustion chamber shapes. However, the models may be encountered with low efficiency subject to overload computational cost, especially when detailed chemistry mechanisms are engaged.

1.2.3 The models based on turbulent mixing descriptions

In this category, Partially Stirred Reactor (PaSR) model is a typical approach to deal with the interactions between turbulence and chemistry. In this method, the mixing of reactants is supposed to occur homogeneously within the fine-scale turbulent structures. Thus, these structures are assumed to act as well-stirred reactors, with unified inner composition and temperature, and the reaction rates are theoretically high owing to favourable mixing conditions. The flow is separated into two regions: the fine-scale structure zones and the “surrounding fluid”(Le Pichon et al., 2012). This model has been mainly practised into the research of supersonic ramjet simulation (Fureby et al., 2015, Chapuis et al., 2013, Georgiadis et al., 2010)and flame stabilisation mechanisms(Zettervall et al., 2017, Fureby et al., 2014) due to its versatility and simplicity.

Another application under this notion is the Linear Eddy Model (Menon and Kerstein, 2011).In this method, the filtered profiles are mapped initially into a diagram with the PDF parameters, named triple map and aims at demonstrating the influence of vorticity on mixing and rotating as far as to the viscous scope. The reaction is considered in the one-dimensional domain. A splitting operator method is introduced to maintain the time scales within physical processes. This can also be seen as a pseudo-statistical approach. This model has been applied to partially premixed combustion (Xiao et al., 2016), auto-ignition (Oevermann et al., 2008) and others(Tsui and Bushe, 2014, Lackmann et al., 2015). One other recently applied model in this group are Eddy Dissipation

Concept, which mainly focuses on moderate or intense low oxygen dilution combustion (Lysenko et al., 2014, Lewandowski and Ertesvåg, 2018, Parente et al., 2016).

1.3 New mathematical concept of modelling turbulent combustion

In essence, large eddy simulation is a mathematical model with filtering operation on the instantaneous governing equations, separating the large scales from the small scales for modelling. As mentioned above, many modelling approaches rely heavily on the theoretical combustion fundamentals, flame geometry and combustion regimes. Besides the conventional categorisation of combustion sub-grid models in the previous part, a new mathematical concept of modelling turbulent combustion is proposed in this work. The conception is to close the LES scalar transport equations using mathematical manipulation of Taylor expansion on the filtered chemical source term.

Historically, a similar notion called the sub-filter-scale (SFS) stress model has been brought forward by researchers from Stanford University (Katopodes et al., 2000b, Katopodes et al., 2000a) and the Taylor expansion is basically on the filtered velocity field. In detail, the unsolved velocity is presented by inverse succession of Taylor series expansion on the velocity field. This presentation is

employed to assess the velocity in the same idea as the other established turbulence models. The derivation of expanding is straightforward and can be shown to be a good approximation to the unresolved velocity field, at least in low Reynolds number flows. The mathematical expansion serves to close the Navier-Stokes equations by providing an expression for the sub-grid Reynolds stress.

Furthermore, in analogy to Reynolds-averaged modelling where the Reynolds stress equations are modelled, one can derive the evolution equations for the sub-filter-scale stress. These evolution equations allow systematic evaluation of the relative contributions by advection, diffusion, dissipation, pressure, rotation, and stratication in the sublter-scale effects felt by the resolved components of the flow(Katopodes et al., 2000b). The model is compared with direct numerical simulation results and achieves good accuracy(Katopodes et al., 2000b). Later, the approach is used to simulate a neutral boundary layer flow over a rough wall and show excellent agreement with similarity theory logarithmic velocity profiles, a significant improvement over standard eddy-viscosity closures(Chow et al., 2005).

The same notion has also been wielded in the premixed combustion context. Domingo and Vervisch from Normandie Université developed a new approach to sub-grid scale modelling turbulent reacting flows(Domingo and Vervisch, 2015) and to evaluate topology-based sub-grid scale combustion models(Domingo and Vervisch, 2017) based on the SFS model. The concrete procedures are stated as: a deconvolution operator is employed from a simple

numerical treatment of the LES signal. The inversion of a discrete filter is derived in physical space from a Taylor expansion of the well-defined filtering operation, leading to explicit or implicit inverse filters, which are directly applied to the three-dimensional scalar signals over the LES grid. The non-linear terms, as the chemical sources, are then computed from the deconvoluted signals, to be filtered back over the LES mesh to advance the solution in time(Domingo and Vervisch, 2017, Domingo and Vervisch, 2015). A turbulent Bunsen flame was simulated to validate the accuracy of the model. In comparison of the SFS model, the main difference is that the Taylor expansion is applied on the scalar field rather than velocity field.

Under the enlightenment of these previous efforts, a novel sub-scale model for turbulent combustion is proposed in this work, based on a mathematical derivation. The model is grounded on Taylor series expansion of the chemical source term. The highlights of this series model are as follows. Firstly, the model is an exact solution of the filtered chemical source term. Secondly, no parameters are required to put in, and no assumption is needed for the sub-grid physics. Thirdly, the approach is not constrained to any particular combustion regime and has the potential to cope with different combustion setups.

1.4 Objectives of this work

Turbulent combustion is a complex phenomenon involved with a large range of time and length scale. Large eddy simulation in this area requires a robust and

cost-efficient combustion technique. The primary goal of this study is to derive and develop an innovative series combustion sub-grid model into a robust and reliable modelling technique in the context of LES for turbulent flames.

Firstly, the derivation is based on Taylor series expansion of the chemical source term around the filtered value. In theory, this mathematical model is capable of capturing turbulence-combustion interactions in premixed, and non-premixed combustion regimes.

Secondly, the model is numerically implemented into OpenFOAM, an open-source C++ toolbox for customised CFD numerical solvers. The solution provided by the series approach is coupled with LES governing equations to close the filtered scalar transport equation.

In order to address the predicting capability across different combustion regimes, well-established experimental flames, including Sandia flame series, a Bunsen piloted jet flame, and a bluff-body stabilised premixed flame, will be simulated with the series model. The comparison with the experimental data will be discussed in detail.

1.5 Thesis outline

This thesis is organized as follows. Chapter 2 will introduce the fundamental theory of turbulent reacting flows in the context of Large Eddy Simulation, including the governing equations, filtering operation, sub-grid stress closures and conventional combustion models. Chapter 3 will demonstrate the

mathematical derivation of the series model as well as the numerical implementation into OpenFOAM. The potential source of errors will also be addressed. Chapter 4 will present the application to simulating the Sandia flame D and F, which is featured by non-premixed premixed regimes and high Reynolds number. Chapter 5 will describe the simulation of a premixed piloted Bunsen methane flame. The last chapter will bring about the investigation of a bluff-body stabilised premixed propane flame.

2 Large eddy simulation of turbulent reacting flows

In this chapter, the theories of large eddy simulation of turbulent reacting flows will be introduced and addressed. To start with, the details of the governing equations and filtering operation will be talked about before arriving at the filtered governing equation. Next, different turbulence models are discussed for closing the unfiltered sub-grid stress term. Finally, the LES extension to turbulent reacting flow will be briefed.

2.1 Governing equations

Applying Newton`s second law to fluid motions under the continuum assumption, reacting flows can be defined by a set of governing equations, namely continuity, momentum, and species and energy equations.

Firstly, the continuity equation manages the mass conservation and can be denoted as:

$$\frac{\partial \rho}{\partial t} - \frac{\partial \rho u_j}{\partial x_j} = 0 \qquad (2.1)$$

Where ρ (kg/m^3) is the density, t (s) is time, u_j (m/s) is the velocity component in the j-th direction, x_j (m) is the spatial vector.

The momentum equation is described as

$$\frac{\partial (\rho u_i)}{\partial t} + \frac{\partial (\rho u_i u_j)}{\partial x_j} = -\frac{\partial p}{\partial x_j} + \frac{\partial \tau_{ij}}{\partial x_j} + g_i \qquad (2.2)$$

Where p (Pa) is the static pressure, and g_i (N) is the body forces per unit volume. τ_{ij} is the viscous stress tensor, and for a Newtonian fluid, it can be expressed as:

$$\tau_{ij} = \mu \left(\frac{\partial u_i}{\partial x_j} + \frac{\partial u_j}{\partial x_i} \right) - \frac{2}{3} \mu \frac{\partial u_k}{\partial x_k} \delta_{ij} \qquad (2.3)$$

where δ_{ij} is the *Kronecker symbol: δ_{ij}=1 if i=j*, 0 if not. In addition, μ (N*s/m^2) is the dynamic viscosity. With the inclusion, the momentum equation is expressed as:

$$\frac{\partial (\rho u_i)}{\partial t} + \frac{\partial \left(\partial \rho u_i u_j \right)}{\partial x_j} = -\frac{\partial P}{\partial x_j} + \frac{\partial}{\partial x_j} [\mu \left(\frac{\partial u_i}{\partial x_j} + \frac{\partial u_j}{\partial x_i} \right) - \frac{2}{3} \mu \frac{\partial u_k}{\partial x_k} \delta_{ij}] + \rho g_i \qquad (2.4)$$

Equations (2.1) and (2.4) are acknowledged as the *Navier-Stokes* equation.

In reacting flows, multiple species must be tackled, and hence the conservation for each species α is taken into consideration. The species transport equation takes the form as:

$$\frac{\partial \rho Y_\alpha}{\partial t} + \frac{\partial \rho u_j Y_\alpha}{\partial x_j} = -\frac{\partial \rho V_{\alpha,j} Y_\alpha}{\partial x_j} + \dot{\omega}_\alpha,\ \alpha=1,\ \ldots,\ Ns-1 \qquad (2.5)$$

where Y_α (-) is the mass fraction of species α, and $\dot{\omega}_\alpha$ is the reaction rate of species α. $V_{\alpha,j}$ (m/s) is the diffusion velocity of species α. In common practise, Fick`s Law is employed:

$$V_{\alpha,j} Y_\alpha = -D_\alpha \frac{\partial Y_\alpha}{\partial x_j} \qquad (2.6)$$

where D_a (m^2/s) is the species diffusion coefficient for species a. However, under the consideration (Poinsot and Veynante, 2005) that Fick`s law is only effective in binary diffusion, the assumption of equal diffusivity is usually employed(Prasad, 2011). By incorporating Equation (2.5) into Equation (2.6), the species transport can be solved in the formation:

$$\frac{\partial \rho Y_\alpha}{\partial t} + \frac{\partial \rho u_j Y_\alpha}{\partial x_j} = \frac{\partial}{\partial x_j}\left[\rho D \frac{\partial Y_\alpha}{\partial x_j}\right] + \dot{\omega}_\alpha \qquad (2.7)$$

The diffusivity coefficient D (-) can be associated with the Schmidt number, a dimensionless number defined as the ratio of momentum diffusivity (kinematic viscosity) and mass diffusivity, donated as:

$$Sc = \frac{\mu}{\rho D} \qquad (2.8)$$

Besides the species transport, the conservation of energy needs to be achieved. The energy equation is given in the form of enthalpy *h*:

$$\frac{\partial \rho h}{\partial t} + \frac{\partial \rho u_j h}{\partial x_j} = \frac{\partial p}{\partial x_j} + \tau_{ij} \frac{\partial u_j}{\partial x_j} + \dot{q} - \frac{\partial q_j}{\partial x_j} \qquad (2.9)$$

where $\dot{q}$ is the heat source term, and q_j is the diffusive flux. The pressure gradient term on the right-hand side (RHS) can be negligible if the flow is under low Mach number, but should be maintained in piston engines. On the RHS, the second term standing for viscous heating is also omitted for low Mach number flows. The third term represents the source of heat. The last term is the diffusive flux, which can be acquired with Fourier`s law.

$$q_j = -\lambda \frac{\partial T}{\partial x_j} + \rho D \sum_{\alpha=1}^{N_{sp}} h_\alpha \frac{\partial Y_\alpha}{\partial x_j} = -\frac{\mu}{Pr} \frac{\partial h}{\partial x_j} - \rho \left(\frac{1}{\sigma} - \frac{1}{Pr} \right) \sum_{\alpha=1}^{N_{sp}} h_\alpha \frac{\partial Y_\alpha}{\partial x_j} \qquad (2.10)$$

where *A* (-) is the heat diffusion or thermal conductivity coefficient. *Pr* (-) is the Prandtl number, which represents the ratio of momentum diffusivity and thermal diffusivity

Neglecting the omitted terms, the energy transport equation is formulised as:

$$\frac{\partial \rho h}{\partial t} + \frac{\partial \rho u_j h}{\partial x_j} = \frac{\partial}{\partial x_j} \left[\frac{\mu}{\sigma} \frac{\partial h}{\partial x_j} \right] + \dot{q} \qquad (2.11)$$

Subsequently, the species and energy transport equations, (2.12) and (2.19), can be unitised in a general formation with regard to a universal reactive scalar ϕ_α (species + enthalpy) needed to describe the system

$$\frac{\partial \rho \phi_\alpha}{\partial t} + \frac{\partial \rho u_j \phi_\alpha}{\partial x_j} = \frac{\partial}{\partial x_j}\left[\frac{\mu}{\sigma}\frac{\partial \phi_\alpha}{\partial x_j}\right] + \dot{\omega}_\alpha(\phi, T) \qquad (2.2)$$

2.2 Turbulence modelling

Turbulence is a phenomenon, which is encountered in everyday phenomena such as sea tides, storming clouds and cooking smoke, as well as engineering applications like propulsion engines and household furnaces. Turbulent fluid motion is characterized by irregularity, rationality, diffusivity and dissipation. Research made by Osborne Reynolds (Reynolds, 1883) revealed that turbulence takes shape when the inertia forces adequately overwhelms the viscous counterpart. The onset of turbulence is described by the Reynolds number

$$Re = \frac{UL}{v} \qquad (2.3)$$

Where U (m/s) is the characteristic flow velocity, L (m) is characteristic length scale of the flow, and v (m^2/s) is the kinematic viscosity.

The behaviour of turbulence can be illustrated by the governing equations (2.8) to (2.11). However, owing to the massive non-linear levels of the partial differential equations, analytical solutions are limited to some simple cases.

To solve for these highly coupled equations, researchers resort to numerical methods. The present approaches are mainly divided into three categories:

• Direct Numerical Simulation (DNS)

• Reynolds Averaged Navier Stokes Equations (RANS)

• Large Eddy Simulation (LES)

DNS resolves the full instantaneous governing equations without any turbulence model, thus all turbulence scales are explicitly captured with their impacts on combustion. Nevertheless, it is not affordable for industrial geometry as the computational cost is enormous. The present implementation is still limited to simple academic flows. Alternatively, the basic concept of RANS is to average the instantaneous governing equations and close the fluctuating quantities with models(Favre, 1969). It has been widely practised in the industry due to its low computational requirement (Poinsot and Veynante, 2005). However, the complexity of flows in modern combustors restricts its accuracy, and lack of fluctuation information is another drawback in nature.

To compromise the conflicts between RANS and DNS, LES (Large Eddy Simulation) was invented, where a spatial or spectral filter is employed to the governing equations. In this manner, large scales motions are separated from the scales under the filter size, where the modelling is required.

2.3 Large eddy simulation

LES applies a low-pass spatial filter to the instantaneous governing equations, separating motions of the small length scale from those of large length scale. The former, known as sub-grid scales, are rather modelled than directly

computed, while the latter are resolved. The filtered field, denoted with a bar above, is defined as:

$$\bar{\phi}(x,t) = \int_{\Omega} G(x - x'; \Delta(x)) \phi(x', t) dx' \qquad (2.4)$$

where Ω is the flow domain, and G is the filter kernel which should be positive definite. Δ is the characteristic filter width, which may alter according to the position, and is usually defined as the cubic root of the cell volume.

A widely used manner for the filtering operation is to adopt a top-hat or box filter:

$$G(x - x') = \begin{cases} \dfrac{1}{\mathrm{D}^3} & for \quad |x - x'| < \dfrac{\mathrm{D}}{2} \\ 0 & otherwise \end{cases} \qquad (2.5)$$

To tackle the density variations in reacting flows, Favre filtering operation is introduced as:

$$\tilde{\phi}(x,t) = \frac{\overline{\rho \phi(x,t)}}{\bar{\rho}} \qquad (2.6)$$

In this way, instantaneous quantities are divided into a resolved filtered mean and an unresolved sub-grid fluctuation:

$$f = \bar{f} + f' \qquad (2.7)$$

$$\phi = \tilde{\phi} + \phi'' \qquad (2.8)$$

Note that different from RANS, the filtering operation should obey these rules of manipulation below:

$$\overline{af} = a\bar{f} \quad (2.9)$$

$$\overline{f_1 + f_2} = \bar{f}_1 + \bar{f}_2 \quad (2.20)$$

$$\bar{\bar{\phi}} \neq \phi \quad (2.21)$$

$$\overline{\bar{\phi}\phi'} \neq 0 \quad (2.10)$$

$$\overline{\bar{\phi}_1\bar{\phi}_2} \neq \bar{\phi}_1\bar{\phi}_2 \quad (2.11)$$

2.3.1 Filtered Navier-Stokes equations

Applying the filtering operation to the governing equations, the filtered equations take the following forms:

Continuity:

$$\frac{\partial \bar{\rho}}{\partial t} - \frac{\partial \bar{\rho}\tilde{u}_j}{\partial x_j} = 0 \quad (2.12)$$

Momentum:

$$\frac{\partial(\bar{\rho}\tilde{u}_i)}{\partial t} + \frac{\partial(\bar{\rho}\tilde{u}_i\tilde{u}_j)}{\partial x_j} = -\frac{\partial \bar{p}}{\partial x_i} + \frac{\partial}{\partial x_j}(2\mu\tilde{e}_{ij} - \frac{2}{3}\mu\widetilde{e_{kk}}\delta_{ij}) + \frac{\partial \tau_{ij}^{SGS}}{\partial x_j} + \bar{\rho}g_i \quad (2.13)$$

where $\tilde{e}_{ij} = \frac{3}{2}\left(\frac{\partial \tilde{u}_i}{\partial x_j} + \frac{\partial \tilde{u}_j}{\partial x_i}\right)$ is the rate of strain tensor. $\tau_{ij}^{SGS} = \bar{\rho}(\widetilde{u_i u_j} - \tilde{u}_i\tilde{u}_j)$ is the unresolved Reynolds stress requires a sub-grid scale (SGS) turbulence model to close.

2.3.2 Sub-grid stress closures

The most common methods to close the unresolved SGS stress are based on the eddy viscosity assumption. The idea is to hypothesise a linear connection between the SGS shear stress and the resolved rate of strain tensor. The SGS stress tensor is estimated as follows:

$$\tau_{ij}^{SGS} \approx \frac{2}{3} k_{SGS} \delta_{ij} - 2\upsilon_{SGS} dev(\bar{D})_{SGS} \quad (2.14)$$

Where υ_{SGS} is the SGS eddy viscosity, $\bar{D}$ is the resolved rate of strain tensor, and k_{SGS} is the SGS kinetic energy.

Different approaches are used to compute this kinetic energy. The Smagorinsky model uses the algebraic local equilibrium, but the one equation eddy viscosity model solve a modelled balance equation to simulate its behaviour. The transport equation is adopted to describe the impact of k_{SGS} attributable to SGS energy production, dissipation and diffusion:

$$\frac{\partial(\rho k_{SGS})}{\partial t} + \frac{\partial(\rho \tilde{u}_j k_{SGS})}{\partial x_j} - \frac{\partial}{\partial x_j}\left[\rho(\upsilon + \upsilon_{SGS}) \frac{\partial k_{SGS}}{\partial x_j}\right] = -\rho \tau_{ij} : \bar{D}_{ij} - C_\epsilon \frac{\partial \rho k_{SGS}^{3/2}}{\Delta} \quad (2.15)$$

Where C_ϵ is a model coefficient.

The main motivation to employ the one-equation SGS models is to dismiss the insufficiency of local balance hypothesis between the SGS energy production and dissipation adopted in these algebraic models. Such a phenomenon may

appear in high Reynolds number flows and/or in the cases of coarse grid resolution.

Besides, an additional dynamic procedure can be employed to evaluate the coefficient C_ε in the transport equation using a test filter field. The field is locally constructed from the grid-scale region by applying a test filter usually 2 times larger than the conventional filter width. In this way, the coefficient is dynamically determined. This process can improve the accuracy of the SGS turbulence model, especially in the high gradient region like shear layers. Benefited from it, this method is frequently used in the following reacting simulations.

2.3.3 Filtered transport equations

After manipulation of filtering operation, the filtered scalar transport equations are described as:

Chemical species:

$$\frac{\partial \bar{\rho}\widetilde{Y_\alpha}}{\partial t} + \frac{\partial \bar{\rho}\widetilde{u_j}\widetilde{Y_\alpha}}{\partial x_j} = \frac{\partial}{\partial x_j}\left[\rho D \frac{\partial \widetilde{Y_\alpha}}{\partial x_j}\right] + \overline{\dot{\omega}_\alpha} - \frac{\partial J^{SGS}_{\widetilde{Y_\alpha},j}}{\partial x_j} \qquad (2.16)$$

Enthalpy:

$$\frac{\partial \bar{\rho}\tilde{h}}{\partial t} + \frac{\partial \bar{\rho}\widetilde{u_j}\tilde{h}}{\partial x_j} = \frac{\partial}{\partial x_j}\left[\rho D \frac{\partial \tilde{h}}{\partial x_j}\right] + \bar{\dot{q}} - \frac{\partial J^{SGS}_{\tilde{h},j}}{\partial x_j} \qquad (2.17)$$

For the sub-grid fluxes, a gradient diffusion assumption of the form:

$$J_{\alpha,j}^{SGS} = -\frac{\mu_{SGS}}{\sigma_{SGS}} \frac{\partial \phi_\alpha}{\partial x_j} \qquad (2.30)$$

where $\overline{\dot{\omega}_\alpha}$ is the unclosed chemical source term, which cannot be resolved directly and remains the most difficult task in turbulent combustion modelling.

2.4 Combustion modelling

2.4.1 Chemical reaction kinetics

Considering a reacting system of *NS* species containing *NR* reactions, the reaction rate for *k*-th elementary reaction is defined as:

$$W_j = k_{fj} \prod_{a=1}^{NS} c_a^{n_f^{aj}} - k_{bj} \prod_{a=1}^{NS} c_a^{n_b^{aj}} \qquad (2.31)$$

where n_f^{aj} and n_b^{aj} are the exponential coefficient of the forward and backward reactions,

Note that c_a (mol/L) is the species molar concentrations.

$$c_a = \frac{r Y_a}{W_a} \qquad (2.18)$$

Are the rate constants, and they are usually modelled using the empirical Arrhenius law:

$$k_{fj} = A_{fj} \exp(- \frac{E_j}{RT}) \qquad (2.19)$$

where A (-) is the pre-exponential constant, and E_j (kJ/mol) is the activation energy.

Summing all the reaction rates results in the chemical source term:

$$\dot{\omega}_\alpha = \sum_{j=1}^{NR} (\varepsilon_b^{\alpha j} - \varepsilon_f^{\alpha j}) \Omega_j \qquad (2.20)$$

where $\varepsilon_f^{\alpha j}$ and $\varepsilon_b^{\alpha j}$ the stoichiometric coefficient of the forward and backward reactions.

2.4.2 Combustion models

Most modelling methods are projected for one particular combustion regime (premixed, or non-premixed). The model developed in this work is not restricted to specific flame structures. Nonetheless, some well-established modelling approaches will be briefly reviewed in this section for the different combustion regimes.

2.4.2.1 Premixed turbulent combustion

Premixed combustion happens after the fuel and oxidiser are mixed at the molecular level. Visually, it is featured by a thin flame front. When turbulence is

introduced, things become different. Fist, turbulence wrinkles the flame front, and in extreme situations, quenches the flame. In turn, combustion generates heat release, which leads to speeding up of flows and gaseous kinematic viscosity increase. The former is the source of flame-generated turbulence, while the latter may laminarise the flow field. These turbulence-combustion synergies bring in a broad range of time and length scales, adding difficulties to modelling. To cope, a large number of approaches were proposed in recent decades.

1, G-equation

The G-equation models employ a prospect that if the flame thickness is thin and the flame front can be defined as a surface propagating, the evolution equation can be expressed by the so-call G-equation:

$$\frac{\partial \bar{\rho}\tilde{G}}{\partial t} + \frac{\partial \bar{\rho}\tilde{u}_i\tilde{G}}{\partial x_j} = \rho_0 \bar{s}_T \left|\nabla \bar{G}\right| \qquad (2.21)$$

Where $\bar{s}_T$ is SGS turbulent flame speed, and it can be modelled by another equation:

$$\frac{\bar{s}_T}{s_L} = 1 + a\left(\frac{\bar{u}'}{s_L}\right)^n \qquad (2.22)$$

Where $\bar{u}'$ is the SGS turbulence level.

G-equation models enjoy a lot of popularity as an LES approach into turbulent premixed combustion, has been applied to practical combustors(Janicka and

Sadiki, 2005). Nevertheless, it has some defections. As the accurate definition of the turbulent flame speed is difficult, the models for approximation are not applicable universally. On the hand, the assumption of very thin flame front is not persuasive, and turbulence can have significant distortion on flame surface.

2, Artificially thickened flames

In this approach proposed by (Butler and O'rourke, 1977), the thin flame front is artificially thickened, and it can be calculated on a coarse grid. In the light of laminar premixed combustion theories, the flame speed and the flame thickness are defined as:

$$\bar{s}_L^0 \propto \sqrt{FD\frac{\dot{\bar{\omega}}}{F}} = s_L^0 \qquad (2.23)$$

$$\bar{\delta}_L^0 \propto FD / \bar{s}_L^0 \propto F\delta_L^0 \qquad (2.24)$$

where D is the thermal diffusivity. Then, consider increasing the thermal diffusivity by a factor and decreasing the mean chemical source term by the same magnitude, and the flame speed stays unchanged. After modification, the expression becomes:

$$\bar{s}_L^0 \propto \sqrt{FD\frac{\dot{\bar{\omega}}}{F}} = s_L^0 \qquad (2.39)$$

$$\bar{\delta}_L^0 \propto FD / \bar{s}_L^0 \propto F\delta_L^0 \qquad (2.40)$$

As long as F is large enough, the thickened flame front can be calculated on the mesh. Now that the reaction rate is achieved in the form of Arrhenius law, flame phenomena (for example, ignition, quenching, stabilisation) can be

maintained, and no sub-models are needed. Nevertheless, when the flame front is thickened by F, the Damkohler number is reduced by F, meaning that the interactions between turbulence and chemistry are altered. This approach has been used widely to study practical combustion problems in gas turbines and other industrial combustors(Colin et al., 2000, Wang et al., 2011, Proch et al., 2017).

3, Flame surface density (FSD)

It is clear that LES meshes are too coarse to resolve the premixed flame front on. However, according to the study (Boger et al., 1998), the filtered progress variable can still be calculated if a physical space Guassian filter is adopted. The closure for flame surface density model is expressed as:

$$\overline{r S_d \left|\nabla c\right|} \approx r_u S_L \mathrm{S_D} \qquad (2.41)$$

Where r_u is the density of unburned gas, and $\mathrm{S_D}$ is the SGS flame surface density.

To evaluate the flame surface density, there are different methods via algebraic expression(Boger et al., 1998), similarity models(Knikker et al., 2004), or solving balance equations(Hawkes and Cant, 2000).

2.4.2.2 Turbulent non-premixed combustion

Turbulent non-premixed combustion is another common phenomenon in engines and other industrial combustors. In structure, it is not essential to

necessitate a perfect mixing of fuel and oxidiser, contrary to premixed combustion. Besides, since the flame does not propagate, undesirable issues like flashback and auto-ignite can be avoided more easily.

1, Linear Eddy Model (LEM)

In linear eddy model, convection and diffusion are regarded as two different processes. SGS chemical reaction and turbulent mixing are described based on a one-dimensional problem(McMurtry et al., 1993). Firstly, turbulent stirring is seen as a re-arrangement process acting on a reference scalar field. Secondly, molecular diffusion and chemistry are resolved through a balance equation:

$$\frac{\partial \rho Y_i}{\partial t} = \frac{\partial}{\partial x}(\rho D_i \frac{\partial Y_i}{\partial x}) + \dot{\omega}_i \qquad (2.42)$$

In this formulation, detailed chemistry can be easily included. Besides, the filtered species fractions and temperature can be estimated directly without other models. Unfortunately, these explicit solutions in each grid give rise to computational overload.

2, Flamelet model

The idea of this approach is that chemical reaction happens so fast that its scale is smaller than the small scales of turbulence. Under this assumption, the reaction zone can be seen as laminar, and diffusion process is normal to the mixture surface. The species transport equations can be expressed as:

$$\frac{\partial Y_i}{\partial t} - \rho \frac{\chi}{2} \frac{\partial^2 Y_i}{\partial Z^2} - \dot{\omega}_i = 0 \qquad (2.43)$$

A steady flamelet assumption is usually adopted due to its simple form. However, when it comes to a slow chemical process such as pollutant generation and heat radiation, it suffers from inaccuracy. Under such circumstances, an unsteady formation should be considered. Current application in LES are (Saghafian et al., 2015, Perry et al., 2017, Philip et al., 2015)

3, transported probability density function

The idea of probability density function (PDF) model is representing flow variables with a one-point, one-time joint PDF. The filtered unclosed terms can be obtained through solving the transport equation in the formation of PDF. Since the PDF transport equation introduces a lot of dimensionalities, statistic approaches like Monto Carlo method and stochastic fields method(Jones et al., 2014) are applied to reduce the high computational load.

Many researchers (Jangi et al., 2015, Kuron et al., 2017, Wang and Kim, 2015, Yadav et al., 2013) have proved transported PDF is a very precise model in predictions of turbulent non-premixed combustion. One major benefit of this method is from the explicit expression of the chemical source term, and various flame behaviours like auto-ignition and quenching can be captured. However, one big setback is the high computational cost from solving a great many independent variables. Besides, lack of an appropriate mixing model constrains this model.

4, Presumed PDF

To mitigate expensive computing cost of the transported PDF method, presumed PDF is introduced. Although the PDFs can present any shape in modeling combustion, they share some behaviour in common and thus can be presumed a certain shape. In many cases, a p-function is assumed. In this way, much computational load is reduced. However, the drawback also comes from the presumed shape, which is very difficult to define when it deals with the multi-dimensional joint-PDFs. This area is also very active in the context of LES in recent years(Baurle and Girimaji, 2003, Lempke et al., 2013, Salehi et al., 2013).

2.4.2.3 Partially premixed combustion

In this regime, the flow field is characterized by simultaneous occurrences of both premixed combustion features like extinction or flame propagation, and typical non-premixed combustion phenomena like mixing-controlled reactions. It is encountered in many modern practical combustors. To tackle the flame complication, a combustion model capable of all regimes is required.

Successful approaches in recent years are flamelet/progress-variable model(See and Ihme, 2015, Knudsen and Pitsch, 2015, Nambully et al., 2014), conditional moment closure model(Coriton et al., 2015, Kronenburg and Stein, 2017) , dynamic thickened flame model(Esclapez et al., 2015), stochastic fields PDF model(Jones and Prasad, 2010).

2.4.3 Brief analysis

Although the theoretical potential of these methods to predict transient phenomena is already widely accepted, in reality, it does not guarantee that it is applicable. A major limitation of LES when applied to industrial-like configurations is the uncertainties introduced by the SGS models. These models, depending on the assumptions they are derived, have limitations in the physics they can represent. Also, some models do not have the correct limiting behaviour as the grid size approached the Kolmogorov scale.

Another problem with LES is the high computational overload. In most LES studies presented in the literature, this results from the higher grid resolution and smaller time-steps in comparison to RANS as well as the use of SGS turbulent combustion models over the whole computational domain, even in areas that not much information in reality lies “below” the grid size. Although the issue of overload resulting from the grid resolution has been addressed by adaptive grid methodologies, less tried are adaptive turbulent combustion models. Apart from adding to the computational cost, non-adaptive models also lead to wrong predictions in some areas. It should be noted that for example most turbulence models are derived based on the idea of enforcing energy dissipation from large scales to smaller ones. However, in more laminarised areas of the flow, the assumption of turbulence cascade fails and the models overestimate the local energy dissipation.

Due to these deficiencies, a new series approach will be presented to provide a new look into turbulent combustion modelling.

2.5 Summary

This chapter serves as theory fundamentals for large eddy simulations of turbulent reacting flows. In the beginning, the governing equations of turbulent reacting flows are addressed. With the notion of filtering operation, the filtered balance equations for LES are arrived at. To close the SGS stress term, a one equation eddy viscosity model is introduced and analysed along with its dynamic procedures. To solve for the turbulent flames, chemical kinetics are introduced. Common combustion approaches in the context of LES are presented and discussed in different combustion regimes.

3 Series Approach for Turbulent Combustion Modelling

In this chapter, the focus is on the development of the series model. Starting points are the mathematical procedures of derivation, which is the emphasis of this work. Then, the implementation into OpenFOAM is addressed. Next, theoretical analysis is introduced to identify the characteristics of the model. Finally, the error sources of the model are briefly discussed.

3.1 Mathematical derivation

In this study, the series SGS model is derived following a mathematical approach, where the multiple-dimensional Taylor series expansion of the unfiltered chemical source term is introduced. As shown in Equation (2.34), the chemical source term is a highly non-linear formation, which can vary sharply in space, besides, it is not differential in physical space. Thus, the series expansion is performed in the scalar space around the filtered value. For simplicity, the formalism is presented first for a single reactive scalar (the extension to multiple variables will be shown in the following sections):

$$\dot{\omega}(c) \approx \dot{\omega}(\bar{c}) + \left.\frac{\partial \dot{\omega}}{\partial c}\right|_{c=\bar{c}} \delta c + \frac{1}{2}\left.\frac{\partial^2 \dot{\omega}}{\partial c^2}\right|_{c=\bar{c}} (\delta c)^2 + \ldots \quad (3.1)$$

Where the species molar concentration $c = \frac{\rho Y}{W}$, W is the molecular weight.

Inside this equation, the term $\delta c = (c - \bar{c})$ is hardly to be predicted in the frame of large eddy simulation. In this sense, a transformation is added to the above equation, which is the highlight of the derivation:

$$\delta c = \frac{\partial c}{\partial x_i} \delta x_i = \frac{\partial c}{\partial x_i} (x_i - \bar{x}_i) \quad (3.2)$$

Then, Equation (3.1) takes the form as:

$$\dot{\omega}(c) \approx \dot{\omega}(\bar{c}) + \left.\frac{\partial \dot{\omega}}{\partial c}\right|_{c=\bar{c}} \frac{\partial c}{\partial x_i} \delta x_i + \frac{1}{2}\left.\frac{\partial^2 \dot{\omega}}{\partial c^2}\right|_{c=\bar{c}} \left(\frac{\partial c}{\partial x_i} \delta x_i\right)^2 + \ldots \quad (3.3)$$

More specifically:

$$\dot{\omega}(c) \approx \dot{\omega}(\bar{c}) + (x_m - \overline{x_m}) \left.\frac{\partial \dot{\omega}}{\partial c}\right|_{c=\bar{c}} \frac{\partial c}{\partial x_m} +$$

$$(x_m - \overline{x_m})(x_n - \bar{x}_n) \frac{1}{2}\left.\frac{\partial^2 \dot{\omega}}{\partial c^2}\right|_{c=\bar{c}} \frac{\partial c}{\partial x_m} \frac{\partial c}{\partial x_n} + \ldots \quad (3.4)$$

Note for compactness, index notation is employed in the equations.

Now filtering operation (for details, the reader can refer to the equations (2.14) and (2.15)) is applied. All terms with odd powers of x, y, and z are eliminated as a result of symmetry. This elimination is identical to the reported Taylor

series expansion of velocity field(Katopodes et al., 2000a, Katopodes et al., 2000b, Chow et al., 2005) and of species scalar(Domingo and Vervisch, 2015, Domingo and Vervisch, 2017).

Then, the equation is organized as:

$$\overline{\dot{\omega}(c)}=\dot{\omega}(\bar{c})+\frac{\Delta_x^2}{24}\frac{\partial^2\dot{\omega}}{\partial c^2}\bigg|_{c=\bar{c}}\overline{\left(\frac{\partial c}{\partial x}\right)^2}+\frac{\Delta_y^2}{24}\frac{\partial^2\dot{\omega}}{\partial c^2}\bigg|_{c=\bar{c}}\overline{\left(\frac{\partial c}{\partial y}\right)^2}+\frac{\Delta_z^2}{24}\frac{\partial^2\dot{\omega}}{\partial c^2}\bigg|_{c=\bar{c}}\overline{\left(\frac{\partial c}{\partial z}\right)^2}+$$

$$\frac{\Delta_x^4}{1152}\frac{\partial^4\dot{\omega}}{\partial c^4}\bigg|_{c=\bar{c}}\overline{\left(\frac{\partial c}{\partial x}\right)^4}+\frac{\Delta_y^4}{1152}\frac{\partial^4\dot{\omega}}{\partial c^4}\bigg|_{c=\bar{c}}\overline{\left(\frac{\partial c}{\partial y}\right)^4}+\frac{\Delta_z^4}{1152}\frac{\partial^4\dot{\omega}}{\partial c^4}\bigg|_{c=\bar{c}}\overline{\left(\frac{\partial c}{\partial z}\right)^4}+\frac{\Delta_x^2\Delta_y^2}{1728}\frac{\partial^4\dot{\omega}}{\partial c^4}\bigg|_{c=\bar{c}}\overline{\left(\frac{\partial c}{\partial x}\right)^2\left(\frac{\partial c}{\partial y}\right)^2}+$$

$$\frac{\Delta_x^2\Delta_z^2}{1728}\frac{\partial^4\dot{\omega}}{\partial c^4}\bigg|_{c=\bar{c}}\overline{\left(\frac{\partial c}{\partial x}\right)^2\left(\frac{\partial c}{\partial z}\right)^2}+\frac{\Delta_z^2\Delta_y^2}{1728}\frac{\partial^4\dot{\omega}}{\partial c^4}\bigg|_{c=\bar{c}}\overline{\left(\frac{\partial c}{\partial z}\right)^2\left(\frac{\partial c}{\partial y}\right)^2}+O\left(\Delta^6\right) \qquad (3.5)$$

As the filtering operation is isotropic, the equation can be rearranged in the form as:

$$\overline{\dot{\omega}(c)}=\dot{\omega}(\bar{c})+\frac{\Delta^2}{24}\frac{\partial^2\dot{\omega}}{\partial c^2}\bigg|_{c=\bar{c}}\left[\overline{\left(\frac{\partial c}{\partial x}\right)^2}+\overline{\left(\frac{\partial c}{\partial y}\right)^2}+\overline{\left(\frac{\partial c}{\partial z}\right)^2}\right]+\frac{\Delta^4}{1152}\frac{\partial^4\dot{\omega}}{\partial c^4}\bigg|_{c=\bar{c}}\left[\overline{\left(\frac{\partial c}{\partial x}\right)^4}+\overline{\left(\frac{\partial c}{\partial y}\right)^4}+\overline{\left(\frac{\partial c}{\partial z}\right)^4}\right]+$$

$$\frac{\Delta^4}{1728}\frac{\partial^4\dot{\omega}}{\partial c^4}\bigg|_{c=\bar{c}}\left[\overline{\left(\frac{\partial c}{\partial x}\right)^2\left(\frac{\partial c}{\partial y}\right)^2}+\overline{\left(\frac{\partial c}{\partial x}\right)^2\left(\frac{\partial c}{\partial z}\right)^2}+\overline{\left(\frac{\partial c}{\partial z}\right)^2\left(\frac{\partial c}{\partial y}\right)^2}\right]+O(\Delta^6) \quad (3.6)$$

For turbulent scalar signals, the fourth order terms were not found to play a major role, and the filtering may be achieved with only the second-order derivatives(Katopodes et al., 2000a) Such approximate filtering has already been used in the atmospheric boundary layer scalar transport(Chow et al., 2005)

and also combustion context, to perform a priori tests of SGS modelling from the filtering of DNS data(Moureau et al., 2011).Terms of $O(\Delta^4)$ and higher are neglected. Numerical schemes for scalar gradients in LES of reactive flows are often second order and therefore retaining the terms O(Δ^4) the series model will only be sixth-order accurate if the order of the overall scheme will change to the same order (Domingo and Vervisch, 2015). The final expressions are arrived at:

$$\overline{\omega(\dot{c})}=\dot{\omega}(\bar{c})+\frac{\Delta^2}{24}\frac{\partial^2\dot{\omega}}{\partial c^2}\Big|_{c=\bar{c}}\overline{\left(\frac{\partial c}{\partial x_i}\right)^2}+O(\Delta^4) \qquad (3.7)$$

The same procedures can be applied to the chemical source term, which is a function of multiple species, temperature and pressure:

$$\overline{\dot{\omega}_\alpha(\varphi_1, \varphi_2, \ldots,\varphi_k)}=\dot{\omega}_\alpha(\overline{\varphi_1}, \overline{\varphi_2}, \ldots,\overline{\varphi_k})$$

$$+\frac{\Delta^2}{24}\frac{\partial^2\dot{\omega}_\alpha(\varphi_1, \varphi_2, \ldots,\varphi_n)}{\partial\varphi_m\partial\varphi_n}\Big|_{(\varphi_1, \varphi_2, \ldots,\varphi_k)=(\overline{\varphi_1}, \overline{\varphi_2}, \ldots,\overline{\varphi_k})}\times\overline{\frac{\partial\varphi_m}{\partial x_i}\frac{\partial\varphi_n}{\partial x_i}}+O(\Delta^4) \quad (3.8)$$

Note for compactness, index notation is employed in the equations.

Inside the equation, the filtered scalar gradient term is not closed. Similarly, it takes the form of scalar dissipation term:

$$\overline{\frac{\partial\varphi_m}{\partial x_i}\frac{\partial\varphi_n}{\partial x_i}}=\frac{\partial\overline{\varphi_m}}{\partial x_i}\frac{\partial\overline{\varphi_n}}{\partial x_i}+X_{SGS} \qquad (3.9)$$

Where χ_{SGS} behaves in analogy to a sub-grid scalar dissipation rate, and it accounts for the effects of un-resolved scalar gradients. In the present work, an algebraic approach (Knudsen et al., 2012) is employed as:

$$\chi_{SGS}=C_{SGS}\frac{\partial\overline{\varphi_m}}{\partial x_i}\frac{\partial\overline{\varphi_n}}{\partial x_i} \qquad (3.10)$$

In the context of non-premixed combustion, C_{SGS} is widely chosen to be 0.1 following (Navarro-Martinez and Kronenburg, 2007, Branley and Jones, 2001). For premixed combustion, C_{SGS} can be presumed as 0 or 0.1 for lack of relevant empirical values reported in previous research. Another method to model the scalar dissipation type term is transport equation models, as (Knudsen et al., 2012) proposed and tested on a non-premixed auto-ignition jet flame. The results showed better accuracy over the algebraic approach. However, its employment still remains within non-premixed scopes and introduces more complexity.

In this way, the model is explicitly closed as:

$$\overline{\dot{\omega}_\alpha(\varphi_1,\varphi_2,\ldots,\varphi_k)}=\dot{\omega}_\alpha(\overline{\varphi_1},\overline{\varphi_2},\ldots,\overline{\varphi_k})$$

$$+\frac{\Delta^2}{24}\frac{\partial^2\dot{\omega}_\alpha(\varphi_1,\varphi_2,\ldots,\varphi_n)}{\partial\varphi_m\partial\varphi_n}\bigg|_{(\varphi_1,\varphi_2,\ldots,\varphi_k)=(\overline{\varphi_1},\overline{\varphi_2},\ldots,\overline{\varphi_k})}\frac{\partial\overline{\varphi_m}}{\partial x_i}\frac{\partial\overline{\varphi_n}}{\partial x_i}+O(\Delta^4) \quad (3.11)$$

The series model can be understood as a combination of a chemical source term neglecting SGS terms (seen as a no-model or perfectly mixed

closure) and a SGS contribution which depends on the square of the filter width, and the model is fourth-order accuracy in terms of Taylor series expansion:

$$\overline{\dot{\omega}(\varphi)}=\dot{\omega}(\overline{\varphi})+\dot{\omega}_{SGS} \qquad (3.12)$$

Note that the second derivative of the chemical source term is conducted on the scalar space. It has analytical solutions in the forms of Arrhenius laws, but numerical procedures are needed when temperature is involved as a variable. This is because the temperature appears in the power of the exponent function, as shown in Equation (2.33).

3.2 Numerical Implementation in OpenFOAM

The series model is implemented based on the OpenFOAM platform. OpenFOAM is a C++ toolbox for the development of customised numerical solvers, and pre-/post-processing utilities for the solution of continuum mechanics problems, including computational fluid dynamics (CFD). These advanced CFD features are essential for modelling industrial fires where the scale is large, and the geometry is complex. The advantages of OpenFOAM using object-oriented programming techniques are fully illustrated in the article(Weller et al., 1998).

In practice, the series model is incorporated in the reactingFoam solver through the scalar transport equations, which is a solver for turbulent reacting flows based on the chemical reactions. To be specific, the library *combustionModel* is modified to import the sub-grid part of the series model into the source term

interface; In order to utilise the information of Arrhenius reaction rate and gradient, the library *chemicalModel* is called. Then, the series model is coupled through the scalar transport equation with LES equations in the frame of a new reactingFoam-like solver. Note that PIMPLE algorithm is employed to deal with iterative procedures for coupling equations for momentum and mass conservation. It is a combination of PISO (Pressure Implicit with Splitting of Operator) and SIMPLE (Semi-Implicit Method for Pressure-Linked Equations) (Jang et al., 1986). In terms of the local strong scalar gradients introduced by discontinuous chemical source term, one fifth of the unfiltered term is restricted for the SGS part. The numerical structures of the series model is shown in Figure 3.1.

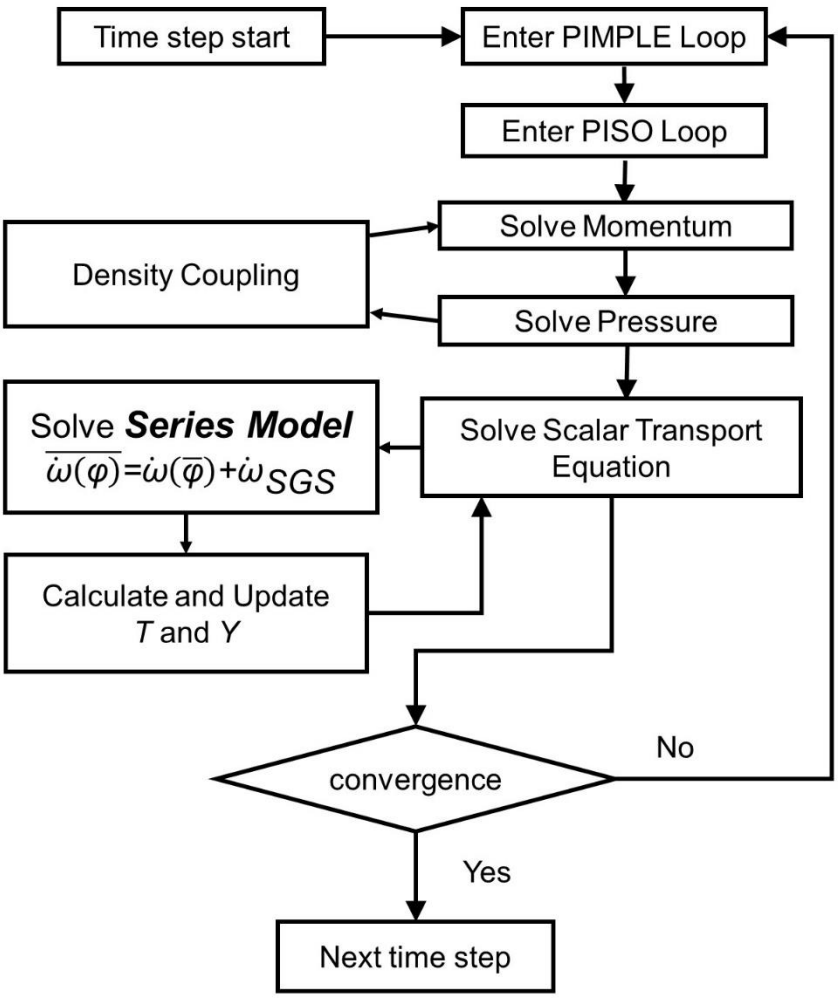

Figure 3.1 The numerical structures of the series model

3.3 Characteristics of the series model

As the full expression of the series model is arrived at, the features of the new sub-grid model can be analysed theoretically.

Firstly, the series model is a mathematical approach other than the conventional models. It has no assumption regarding the combustion regime

and, *a-priori*, the model could be applied to both premixed, and non-premixed premixed combustion regimes. This characteristic will be presented in the following chapters.

Secondly, although similar approaches (Villasenor et al., 1992) had been tried within the RANS context, they were not successful. In RANS the non-linear terms of the series expansion ($\dot{\omega}_{\mathrm{flucturation}}$) can have values much higher than the first order term, because of the large temporal fluctuations. This makes the model very sensitive to the modelling of the terms ($\overline{Y_F"Y_O"}, \overline{Y_F"T"}$). In LES, on the contrary, the magnitude of these terms is smaller given a relatively better-resolved grid that is always necessary to capture (non-reactive) flow characteristics related to features above the Taylor scale.

Besides, all the information for the model is obtained from the flow field. The accuracy level of the method is determined by the Taylor series order.

Last but not least, the model also predicts the correct limiting behaviour, and the sub-grid contribution reduces with the square of the filter size, approaching DNS as Δ approaches Kolmogorov scales. This is clearly shown in Equation (3.10).

3.4 Error analysis

Although the series model is derived in a mathematical approach and the formulation is explicit in theory, computational errors can inevitably be introduced when applied to numerical simulation of LES like other well-

established sub-grid combustion models. In the analysis, the sources of error potentially come from these aspects as flows:

Firstly, the influence of higher order terms.

The accuracy of the model is mainly determined by order of Taylor series, as same as other Taylor series expansion in mathematical nature. In application, terms of the fourth and higher order are neglected, due to that commonly the fourth orders were not found to play a major role. Nevertheless, under some extreme conditions like deflagration and detonation, the higher order signal can significantly affect the flow field. In these cases, the neglecting of higher orders may lead to inaccuracy of predicting the sub-grid influence. On the other hand, another difficulty comes from a theoretical derivation. Katopodes (Katopodes et al., 2000a, Katopodes et al., 2000b) pointed out that the filtering may be achieved with only the second-order derivatives. However, in general, numerical schemes for scalar gradients in LES of reactive flows are often second order and therefore retaining the $O(\Delta^4)$ the terms will be accurate (Domingo and Vervisch, 2015).

Secondly, the approximation of the scalar gradient term

The approximation in the equation (3.9) could be inaccurate in some poorly resolved premixed flames, where the unfiltered scalar gradients are much larger or smaller than filtered ones. This can be improved by employ a more refined mesh, or adding a *sub-grid* mixing model, or a scalar dissipation type approximation.

Thirdly, the numerical scheme for gradients

In turbulent flames, the scalar gradient can be quite strong especially in the shear layers introduced by the discontinuous chemical source term. This will give rise to inaccuracy in the prediction of the numerical scheme. Under this circumstances, a specific numerical treat should be employed with limiting behaviours. Another solution is to increase the mesh resolution near the strong gradient areas.

Fourthly, the chemical mechanisms.

The series model consists of a second derivative of the chemical source term in the expression. If the chemical mechanism used is not accurate, it will influence not only the chemical contribution to the flow field but also the prediction of the sub-grid scale quantity. Potentially, a more detailed mechanism would provide better accurate prediction, however, it would introduce more computational load. The choice of a well-established chemical scheme is very crucial.

3.5 Examination scope within this study

The application of the series model in this work will be limited to turbulent reacting flows at low Mach numbers (Ma < 0.8), as the governing equations in the solver are under low Mach number assumptions. The validation experimental cases are selected within this range.

Besides, the soot effect is negligible. In the Sandia flame cases, the jet fluid is a mixture of three-parts air and one-part CH4 by volume. This mixture significantly reduces the problem of fluorescence interference from soot precursors, allowing improved accuracy in the scalar measurements. In the Bunsen flame and bluff-body stabilised flame, the lean premixed combustion generates soot-free flames. Meanwhile, thermal radiation is not reported to play a significant role in these above flames, and is not considered in this study. Most published LES simulation of the investigated cases neglected these 2 factors as well.

3.6 Summary

In this chapter, a new series approach for combustion modelling in LES is derived and introduced. At first, the mathematical procedures of derivation are addressed. The principle notion is based on Taylor series expansion of the unclosed source term around the filtered value. An important step within is to transform the differentials in the scalar field, which is hardly to be determined, to those in the physical space.

Then, the model is implemented into the reactingFoam solver on the platform of OpenFOAM. PIMPLE algorithms are employed to deal with the couple of density and pressure. The detailed code structure is shown in the flowchart.

Next, theoretical analysis is introduced to identify the characteristics of the model. The model is independent of combustion regimes and free from other

parameters. Besides, the model has the properties of limiting behaviour when the filter size approach Kolmogorov scales.

Finally, the error sources of the model are briefly discussed. Four potential sources are identified, that is, the influence of higher order terms, the scalar gradient term, the numerical scheme, and the chemical mechanisms. Besides, the control measures to reduce them is also brought forward. The examination scope is outlined as well.

The following chapters are devoted to full scale test cases using the series model derived in this chapter. In Chapter 4, Sandia flame series in the non-premixed premixed regime will be simulated, followed by the computation of a Bunsen piloted premixed flame in Chapter 5. Finally, the results of a bluff-body stabilised premixed flame will be discussed in Chapter 6.

4 Simulation of Sandia Flame Series

In this chapter, the simulation of Sandia flame D and F is presented to demonstrate the capability of the series model in predicting turbulent non-premixed combustion. The simulation is conducted in two grid resolutions, and no SGS model is employed as a comparison test.

4.1 Introduction

The Sandia Flames represent an ideal validation benchmark, as they encompass a range of turbulent burning regimes from a simple non-premixed flame (Flame D) to flames with strong extinction and re-ignition (Flames F) in essentially the same geometric configuration(Jones and Prasad, 2010). Since release, they have been widely used for model verification. Table 4.1 lists the details of previous Sandia flames LES simulation cases.

Table 4.1 Survey of previous Sandia Flames LES simulation cases (mostly in recent ten years)

Researchers	**Simulation targets**	**Turbulent SGS closures**	**Turbulent reacting LES closures**	**Simulation domain**	**Grid resolution**	**Chemistry mechanism**	**Code**
Thomas Jaravel(Jaravel et al., 2018)	Flame D	SIGMA eddy viscosity model	Direct integration of reduced chemical kinetics	40D× 40D× 138D	375 million tetrahedral elements(unstructured meshes)	GRI 2.0 and 3.0	AVBP solver co-developed by CERFACS and IFPEN
Wei Zhao(Zhao, 2017)	Flame D and F	Dynamic Smagorinsky model	multi-environment PDF model	(8-44D) × 2π× 80D	197 × 101 × 64(cylindrical coordinates)	Reduced GRI 3.0	Self-developed house code
A.W. Vreman(Vreman et al., 2008, Vreman et al., 2009)	Flame D and F	An eddy-viscosity model	presumed β-pdf and thickened flame approach	40D× 40D× 150D	128 × 128 × 320(Cartesian coordinates)	GRI 3.0	Self-developed house code
Matthias Ihme(Ihme and Pitsch, 2008b, Ihme and Pitsch, 2008a)	Flame D and E	Dynamic Smagorinsky model	Extended flamelet/progress variable model	26.5D× 2π × 80D	160× 64× 256 (cylindrical coordinates)	GRI 2.11	Self-developed house code
W.P. Jones(Jones and Prasad, 2010)	Flame D-F	Smagorinsky model	Eulerian stochastic field method	20D× 20D× 50D	81 × 81 × 160 (Cartesian coordinates)	augmented reduced mechanism of GRI3.0	Self-developed house code
Radu Mustata(Mustata et al., 2006)	Flame D	Eddy viscosity model	Eulerian Monte Carlo field method	40D× 40D× 84D	68 × 68 × 106 (Cartesian coordinates)	Jones and Lindstedt 4-step mechanism	Self-developed house code

Venkatramanan Raman(Raman and Pitsch, 2007)	Flame D and E	Dynamic Smagorinsky closure	Lagrangian filtered-density approach	20D× 2π × 80D	256 × 128 × 32 (cylindrical coordinates)	GRI-2.11	Self-developed house code
A. Garmory(Garmory and Mastorakos, 2011)	Flame D and F	dynamic Smagorinsky model	Conditional Moment Closure	20D× 20D× 80D	1.3M nodes (CMC grids)	ARM2 chemistry	Self-developed house code
Y Ge, M.J.Cleary (Ge et al., 2011, Ge et al., 2013, Cleary et al., 2009)	Flame D-F	dynamic Smagorinksy Model	hybrid Eulerian LES/sparse-Lagrangian MMC model	35D× 2π × 35D	512 × 55 × 32 (cylindrical coordinates)	GRI-3.0	Self-developed house code
DA Lysenko(Lysenko et al., 2014)	Flame D	one equation eddy viscosity model	Eddy Dissipation Concept	21D× 2π × 73D	240 × 60 × 90 (cylindrical coordinates)	GRI3.0 and Single Step mechanism	OpenFOAM
H. Pitsch (Pitsch and Steiner, 2000)	Flame D	Smagorinsky model	Lagrangian Flamelet Model	15D× 2π × 80D	110× 48× 192 (cylindrical coordinates)	GRI 2.11	Self-developed house code
MRH Sheikhi(Sheikhi et al., 2005)	Flame D	modified kinetic energy viscosity model	Flamelet model	15D× 15D× 80D	101 × 101 × 91(Cartesian coordinates)	GRI 2.11	Self-developed house code
Navarro-Martinez(Navarro-Martinez et al., 2005)	Flame D	Smagorinsky model	Conditional Moment Closure	8D× 8D× 80D	96 × 96 × 320 Cartesian coordinates)	Detailed mechanism by Meyer	Boffin

4.2 Test case formulation

4.2.1 Experimental setup

Experimentally, Sandia Flames are a well-documented series of six piloted methane/air jet flames (A-F), which share the same geometric configuration and species composition of the main, pilot and co-flow inlet jets, but are different in the main and pilot inlet velocities. The cases selected here for validation are Flame D and F; Flame D presents a small degree of extinction and re-ignition, with Flame F approaching blow-off. These flames have been studied experimentally on a piloted burner at Sydney University(Masri et al., 1996) by Barlow (Barlow and Frank, 1998) who measured the temperature and species field, and Schneider (Schneider et al., 2003) who provided LDV velocity details. The burner has an inner nozzle with a diameter D = 7.2 mm, where the fuel is injected at different bulk velocities 49.5m/s and 65m/s for Flame D and F respectively, corresponding to a Reynolds number of Re = 22400 and 44800. The main fuel is a mixture of 25% methane and 75% air by volume, which generates soot-free flames. The pilot nozzle extends to a diameter of 18.2mm, which is coaxial to the main jet. From it exits a lean (Φ = 0.77, T = 1880K) mixture of C_2H_2, H_2, air, CO_2, and N_2 with the same nominal enthalpy and equilibrium composition as methane/air at this equivalence ratio. The flow rates to the main jet and the pilot are scaled in proportion for the C-F series, so that the energy release of the pilot is approximately 6% of the main jet for each

flame. Surrounding the pilot nozzle air streams at a velocity of 0.9m/s. The burner exit is positioned approximately 15 cm above the exit of the vertical wind tunnel. Table 5.2 outline the length scale parameters of the Sandia Flames D and F.

Table 4.2 Parameters for the Sandia Flames

Parameter	Expression	Value
Main jet nozzle diameter (Characteristic Length)	D	7.2mm
Integral Length Scale	L_I $(=D)$	7.2mm
Bulk Inlet Velocity (Characteristic Flow Velocity)	U_{in}	Flame D: 49.6m/s ~ Flame F: 99.2m/s
Macroscopic Reynolds Number	Re_{sh}	Flame D: 24,000 ~ Flame F: 48,000
Inlet Temperature	T_{in}	298K
Nominal Pressure	P	101kPa
Kolmogorov Length Scale	$Re_{sh}^{-3/4}D$	Flame D: 3.7 μm ~ Flame F: 2.2 μm
Cold Flow Filter Width (Pope's Criterion(Wang et al., 2011))	$\triangle=0.083L_I$	0.60 mm
Shear Layer Fluctuation measured (Schneider et al., 2003)	u'	Flame D: 6.1m/s ~ Flame F: 13.2m/s
Integral Time Scale	$t_I= L_I / u'$	Flame D:1.2ms ~ Flame F:0.56ms
Kolmogorov Time Scale	$Re_{sh}^{-1/2}t_I$	Flame D: 7.7 μs ~ Flame F: 2.5 μs
CFL Criterion Time Scale	$C_{max}\triangle/(U_{in}+U_{sound})$	Flame D: 1.5 μs ~ Flame F: 1.3 μs

4.2.2 Simulation setup

According to Table 4.1, the radial solution domain widely chosen ranges from 15D to 40D, while the axial part from 35D to 150D. In this paper, the domain for Flames D and F is extend to 70D in the axial direction(Previous studies(Elbahloul and Rigopoulos, 2015, Jones and Prasad, 2010) suggest that clapping the grids to 50D doesn't affect the results), and in the radial direction it has an increase from 15D to 30D in order to capture the downstream flame/temperature expansion. The grid used is mostly aligned with polar coordinates, but in the centre, a square section (o-grid) is applied to avoid very fine meshes in the centreline. Two resolutions are employed: a fine grid of 210 nodes in the radial direction, 83 points in the tangential direction, and 48 points in the azimuthal direction; and a coarse one, which is approximately downscaled with a factor of 1.5 in each direction (139, 61, 36). The sketch of simulation domain and grid allocation is shown in Figure 5.1.

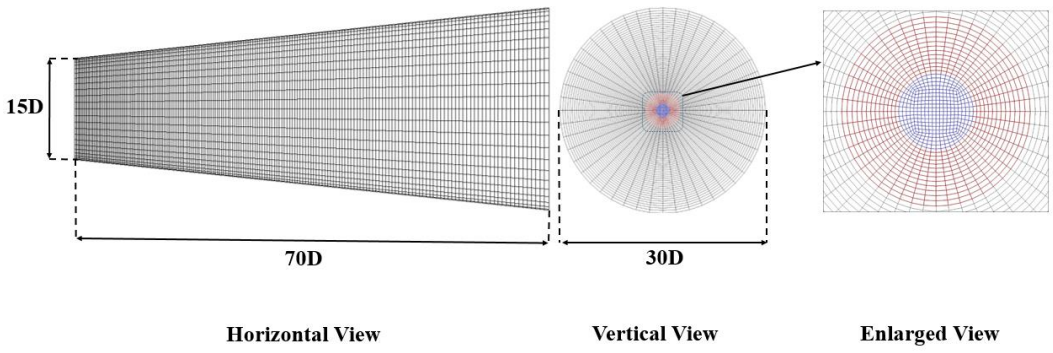

Figure 4.1 A sketch of simulation domain and grid allocation. Blue area: main jet. Red area: pilot stream**.**

At the inlet boundary, the mean velocity profiles are prescribed with the detailed flow field experimental data(Schneider et al., 2003) 1mm above the nozzle exit. The inflow turbulence intensities is imposed with the method of random spots by Kornev and his co-workers (Kornev and Hassel, 2007a, Kornev and Hassel, 2007b, Kornev et al., 2007). For the species, flat profiles are specified using the measurements of Barlow(Barlow and Frank, 1998). Free slip conditions are used for the lateral boundary, while a non-reflecting outflow conditions are used at the outflow plane. For time marching, a second order implicit backward differencing scheme is employed. A variable time step is utilised, with compressible Courant number restriction of 0.2. The chemical mechanism used in the present work is the refined one proposed by Jones and Lindstedt (Jones and Lindstedt, 1988) with 4 reactions and 7 species. Besides the series model, a no SGS model neglecting the SGS part in the chemical source term ($\overline{\dot{\omega}_\alpha(\varphi_1, \varphi_2, \ldots, \varphi_k)} = \dot{\omega}_\alpha(\overline{\varphi_1}, \overline{\varphi_2}, \ldots, \overline{\varphi_k})$) is employed to be a comparison test.

4.3 Results and analysis

4.3.1 Instantaneous flow-field structures

Snapshots of the instantaneous fields for Flame D and F are shown in Figure 4.2. From the temperature distribution in Figures 4.2(a) and 4.2(d), the flame structure displays the conventional characteristics of non-premixed combustion (Poinsot and Veynante, 2005) : an initial region close to the injection nozzle where the flame is thin and a subsequent zone where the hot product fills the majority of the downstream realm. From the reaction zone depicted in Figures

4.2(b) and 4.2(e), the flame structure exhibits two reaction zones separated by pilot jet: the inner part is located in the junction between fuel and pilot jet, where the reactant mixture is ignited by the pilot stream; the outer part is roughly between pilot and co-flow, where the fuel in the pilot jet mixes with the air and burns. Figures 4.2(c) and 4.2(f) show that the SGS contribution to the source term appears in the reaction zone accordingly, where the series model functions. For both Flames D and F, high SGS levels are located in the inner reaction zone, and in this region (see Figures 4.2(b) and 4.2(e)), the reaction rate is also far larger than in the outer part. This is due to intense mixing and combustion happening in the interface between the fuel stream and hot pilot jet. Besides, it indicates important sub-grid turbulence-chemistry interactions herein. Compared with Flame D, both the maximum absolute value and SGS level of CH_4 reaction rate in Flame F increase. It is attributed to the high Reynolds number, and consequently, intense turbulence enhanced combustion.

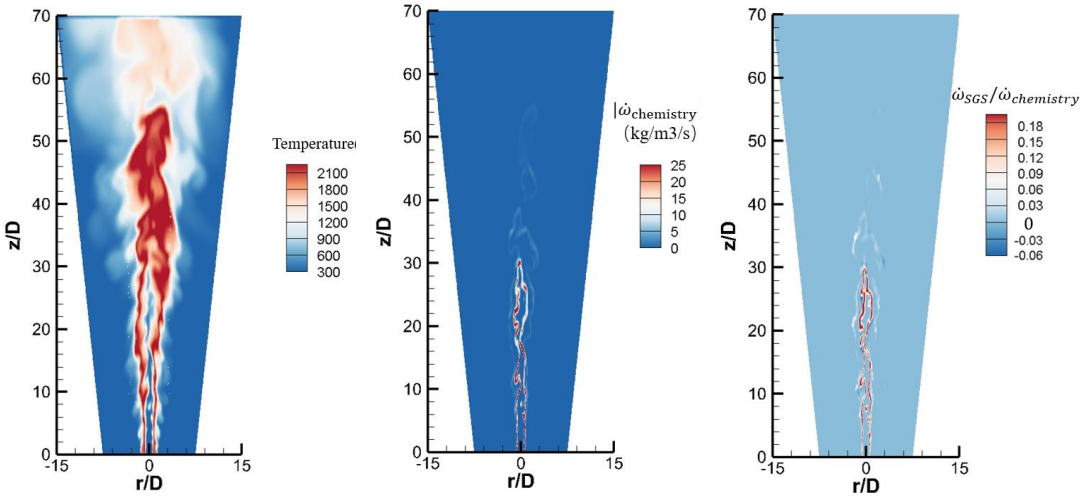

a. Temperature (Flame D) **b. absolute value of the CH_4 reaction rate (Flame D)** **c. SGS contribution ratio of CH_4 reaction rate (Flame D)**

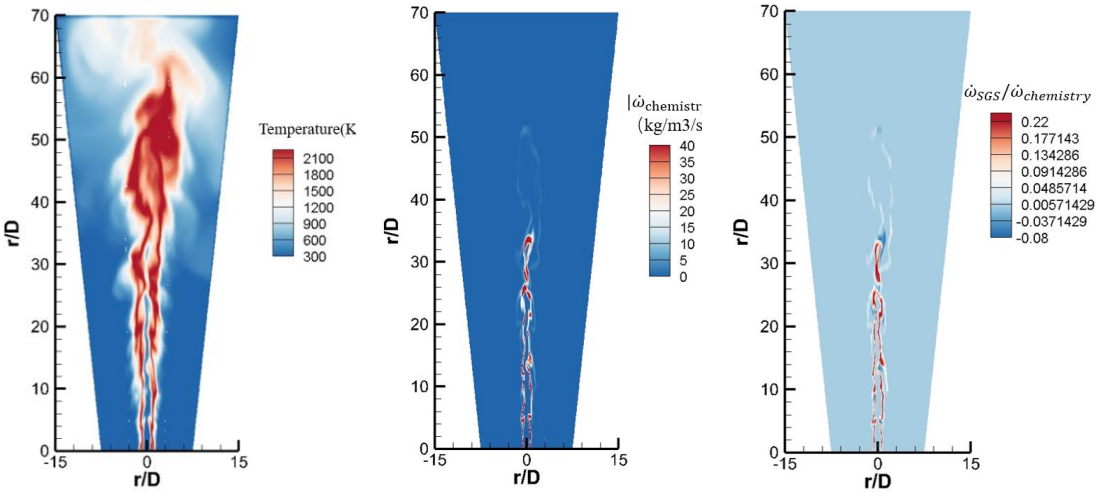

d. Temperature (Flame F) **e. absolute value of the CH_4 reaction rate (Flame F)** **f. SGS contribution ratio of CH_4 reaction rate (Flame F)**

Figure 4.2 Instantaneous snaps of temperature, CH_4 reaction rate and SGS contribution ratio for Flame D and F

4.3.2 Statistical flow-field results

4.3.2.1 Flame D

To compare, a set of published Flame D predictions by (Mustata et al., 2006) are imported in the following results plots, and are called the Mustata predictions hereby. The main reason to select this publication as a reference is that it adopts the same 4-step chemistry mechanism and employs the advanced Eulerian stochastic field method (ESF) for combustion modelling. For SGS stress, the eddy viscosity model is used while in this work dynamic procedures are added. The numerical computations were carried out with a parallelized (by domain decomposition) second-order accurate finite-volume code called BOFFIN (boundary fitted flow integrator). The results presented are carried with a grid resolution of 1,001,952 cells, specifically, 84*84*142 nodes, while the fine mesh in this study uses 836,640 cells. The domain size has dimensions 40D*40D*84D, which is a little larger than the series model simulations. All boundary conditions are the same as those in this work, except on the spanwise surfaces of the computational domain a “wind-tunnel” (Dirichlet type, with the same magnitudes as the inflow extremities) condition is imposed.

Statistical collection is performed over 16 burner flow-through times based on the jet bulk velocity. Prior to that, 10 burner flow-through times are simulated to ensure the flows established. All simulations are performed on the UK national supercomputing service Archer with 480 2.7 Ghz processors. The total simulation time for no SGS model, series model in coarse grids, and series

model in fine grids are respectively 27hrs, 36hrs, and 71hrs. In comparison, the simulation time for 22 flow through times on a Beowulf with 16 Pentium 4, 2.8-GHz/2.0-GB nodes interconnected with Myrinet in Mustata`s simulation is 21 days.

Figure 4.3 shows the mean and RMS temperature distribution along the centreline and radial profiles at axial distributions. Along the centreline, the mean temperature, accordingly the flame location, is well reproduced for the series model in 2 grids, and so are the Mustata predictions. The temperature RMS keeps the same level as the experimental data, although slightly over-prediction appears in the upstream before z/D =30. Besides, the RMS profile along the centreline duplicates the observations in the experiments that the minimum arises around the location of the maximum mean profile. Mustata`s results predicted a very close RMS level to the fine resolution simulation of the series model. However, this feature is not reproduced by the no SGS model. For the radial distribution, the maximum temperatures at 15D and 30D are overpredicted by 200K or so, and the over predictions are also detected in the outer zone (fuel-lean side) at 7.5D and 30D positions. The discrepancies may originate from the thermal radiation that is not considered in LES simulations. The over predictions are also spotted in Mustata`s simulations. At the downstream 45D location, both series model and the ESF model predict a good agreement with experiments. Overall, the series model is better at capturing the temperature trend than no SGS model, especially along the centreline. When the grid is refined, the results improve, and it is more evident in the downstream.

The mean mixture fraction distribution along the centreline and radial profiles at axial distributions is depicted in Figure 4.4. The definition of mixture fraction in this study is the same as the official documents of Sandia Flame series, following Bilger, except that only the elemental mass fractions of hydrogen and carbon are included. This is because the jet and coflow boundary conditions for the elemental oxygen mass fraction are relatively close, and shot noise in the measurements of elemental oxygen mass fraction causes additional noise in the mixture fraction as normally defined (Barlow and Frank, 1998). The definition is:

$$F = \frac{\frac{0.5(YH-Y2H)}{WTH} + \frac{2(YC-Y2C)}{WTC}}{\frac{0.5(Y1H-Y2H)}{WTH} + \frac{2(Y1C-Y2C)}{WTC}} \qquad (4.1)$$

Where

YH = H element mass fraction in the measured sample,

YC = C element mass fraction in the measured sample,

Y1H = H element mass fraction in main jet stream,

Y1C = C element mass fraction in main jet stream,

Y2H = H element mass fraction in coflow stream,

Y2C = C element mass fraction in coflow stream,

and *WTH* = 1.008, *WTC* = 12.011 are atomic weights.

Observed from the centreline profiles, the series model predicts reasonably accurate agreement with measurements in the fine grid, only with small over-prediction from Z/D=10 to 40, illustrating that the shapes of the flame are reproduced correctly. The fine grid results are very close to the Mustata predictions, in which the mixture fraction is over predicted before Z/D=20. In the coarse grid, the profile tends to extend beyond the experimental data on a larger scale, but the series model still behaves much better than the no SGS model does. On the other hand, the radial profiles of mixture fraction at different locations show a good agreement with experiments. Slight over-predictions are observed in the outer (fuel-lean side) regions at Z/D =30 and 45 respectively, indicating downstream radial overspreading of the jet. These over-estimations are more apparent for the no SGS model. In Mustata`s predictions, the ESF model generate slight under-estimations at the locations Z/D = 7.5 and 15.

Figure 4.5 describes the mean and RMS velocity distribution along the centreline. Clearly, both the mean quantities and RMS are reasonably well predicted for the series model in two grids, albeit with some acceleration after 15D. These discrepancies are more obvious in the no SGS model results. In this regard, the ESF model predicts a better agreement with experimental data.

Figures from 4.6 depicts the mean and rms profile of CH_4 mass fractions along the centreline and radial distribution at different axial location. As the centreline profiles show, the reactants CH_4 consume faster than the experiments, identical to the predicted temperature trend. The discrepancies are also spotted in the Mustata predictions. For the radial profiles at different axial locations, both the

series model and ESF model predict a good trend, though the under-predictions are found on the fuel-rich side at the locations z/D = 7.5, 15 and 30 as well. It can be attributed to the limitations of the simplified mechanism used here. The findings of Roomina *et al.* (Roomina and Bilger, 2001) and Mustata *et al.* (Mustata et al., 2006) suggest that the C1 scheme in the mechanism gives rise to an over-prediction of reaction rates on the fuel-rich side of the non-premixed flames. Besides, the global reaction mechanism suffers from the shortcomings of predicting intermediates as it is susceptible to diffusive transport (Jones and Lindstedt, 1988). The large discrepancy at the location z/D = 4.5 for the no SGS model is due to the fact that the centreline profile is over predicted. It shows the inefficiency of the no SGS model in a coarse grid resolution and the importance of a robust combustion model.

Figures from 4.7 shows the mean and rms profile of O_2 mass fractions along the centreline and radial distribution at different axial location. As the centreline profiles show, the oxidizer consumes faster than the experiments, identical to the predicted CH_4 trend. The discrepancies are also spotted in the Mustata predictions. For the radial profiles at different axial locations, both the series model and ESF model predict a good trend, though the under-predictions are found on the fuel-rich side at the locations z/D = 15 and 30 as well. It can be attributed to the same reason of the limitations of the simplified mechanism explained in the CH_4 predictions.

Figure 4.8 describes the mean and rms profile of CO_2 mass fractions along the centreline and radial distribution at different axial location. Along the centreline,

the mean profile is well reproduced for the series model in 2 grids, and so are the Mustata predictions. The RMS values keep the same level as the experimental data, although slightly over-prediction appears in the upstream before z/D =30. For the radial distribution, an overall agreement with experimental data is achieved by the series model, except that the maximum value at x/D=15D are slightly overpredicted. Mustata`s results predicted a very close mean level to the fine resolution simulation of the series model, though the positions of the maximum are slightly under-estimated at location x/D = 7.5 and 30. Overall, the series model is better at capturing the CO_2 trend than no SGS model, especially along the centreline. When the grid is refined, the results improve, and it is more evident in the downstream.

Figure 4.9 depict the mean and rms profile of H_2O mass fractions along the centreline and radial distribution at different axial location. Observed from the centreline comparison, the mean profile is well reproduced for the series model and the ESF model in the Mustata predictions. The RMS values keep the same level as the experimental data, although slightly over-prediction appears in the upstream before z/D =30. For the radial distribution, an overall agreement with experimental data is achieved by the series model, except that the maximum value at x/D=7.5, 15, and 30 are slightly overpredicted. Mustata`s results predicted a very close mean level to the experimental, though the positions of the maximum are slightly under-estimated at location x/D = 7.5 and 30. Overall, the series model is better at capturing the H_2O trend than no SGS model, especially along the centreline. When the grid is refined, the results improve.

Figures 4.10 and 4.11 exhibit the mean and rms profile of CO and H_2 mass fractions along the centreline and radial distribution at different axial location respectively. The mean profile of the both intermediates CO and H2 are excessively over-predicted, and this is also evident in the Mustata simulation. It is almost out of the same mechanism reasons mentioned above, as explained in the part of CH_4 predictions.

For all the results, improvements are observed with grid refinement, especially in terms of the prediction of the temperature and mixture fraction. Overall, the differences in the results obtained with the two grids are relatively small and this indicates that the mesh resolution is sufficient and the model shows good grid sensitivity. Compared with the non-model simulation, the series model significantly improves mean and fluctuation predictions of the scalar and velocity fields.

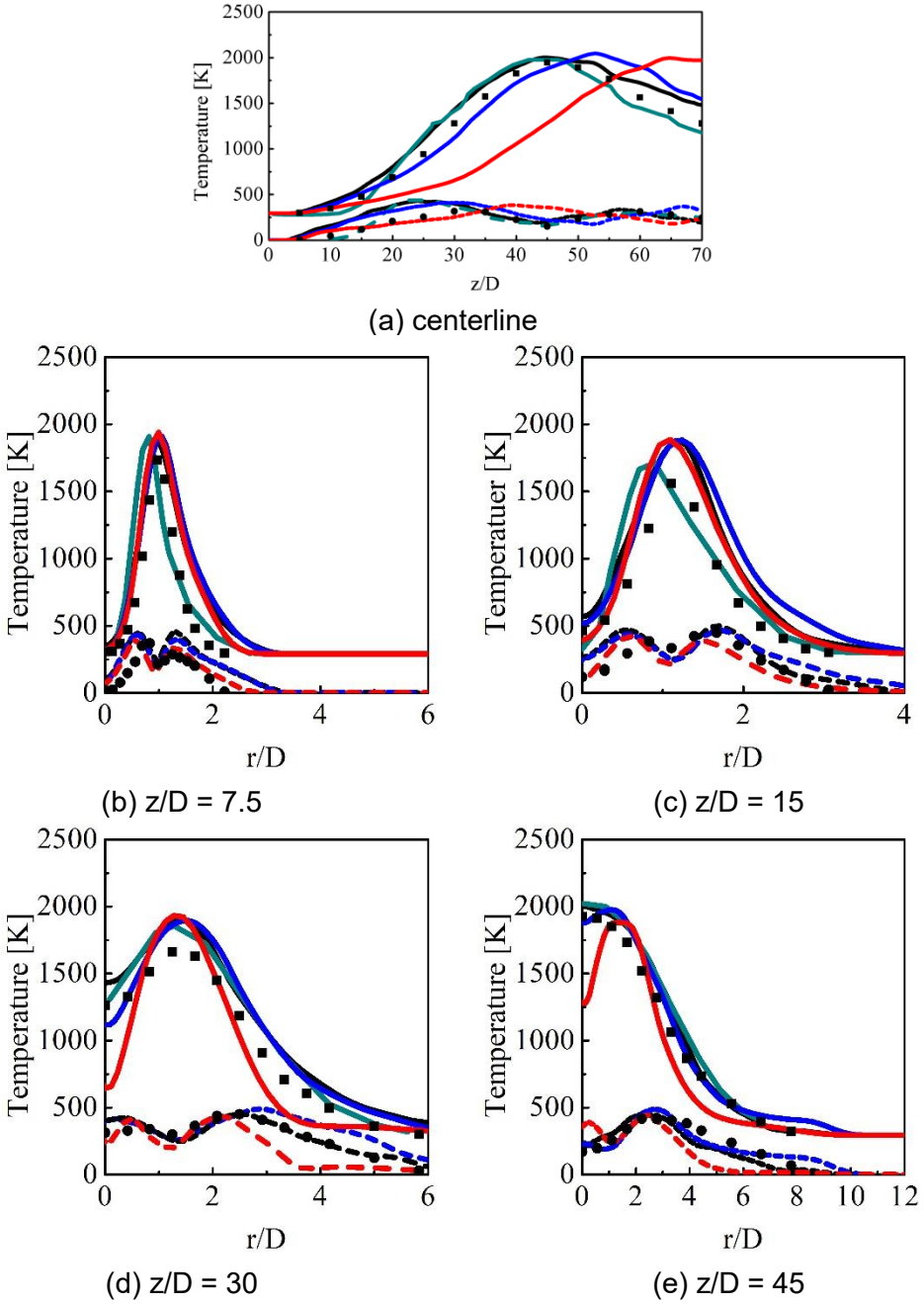

Figure 4.3 Mean and rms profiles of temperature along the centreline and at different axial locations. Black solid line: mean value of series model in fine grid (i). Blue solid line: mean value of series model in coarse grid (ii). Red solid line: mean value of no-SGS model in coarse grid (iii). Square scatter: mean experimental data (Barlow and Frank, 1998) (iv). Black dashed line: rms value of series model in fine grid (v). Blue dashed line: rms value of series model in coarse grid (vi). Red dashed line: rms value of no-SGS model in coarse grid (vii). Round scatter: rms experimental data (Barlow and Frank, 1998) (viii). Green solid line: mean value of ESF model in Mustata`s simulations (Mustata et al., 2006) (ix).

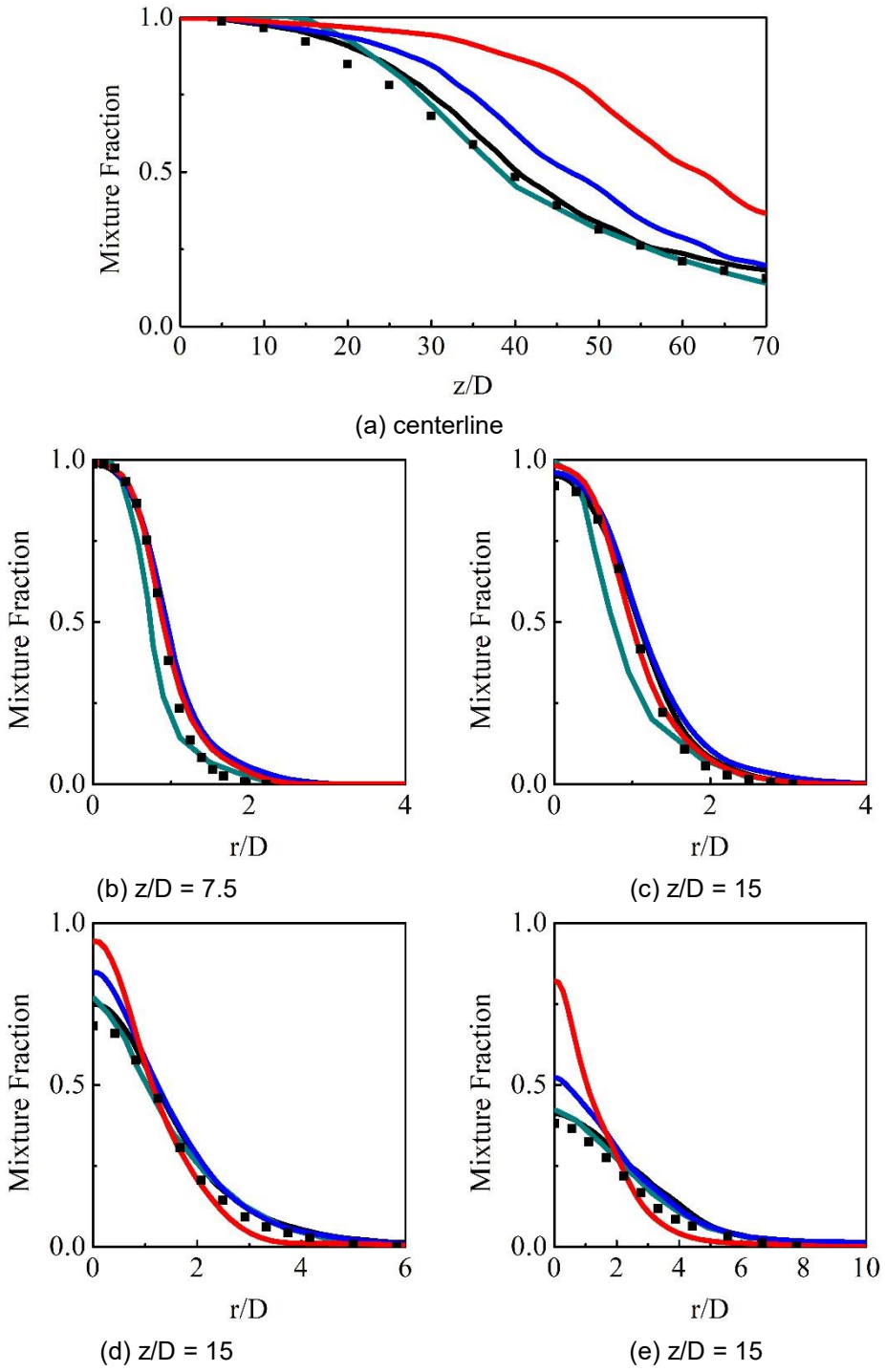

Figure 4.4 Mean profiles of mixture fraction (-) along the centreline and at different axial locations. Black solid line: series model in fine grid (i). Blue solid line: series model in coarse grid (ii). Red solid line: no-SGS model in coarse grid (iii). Square scatter: experimental data (Barlow and Frank, 1998) (iv). Green solid line: mean value of ESF model in Mustata`s simulations (Mustata et al., 2006) (v).

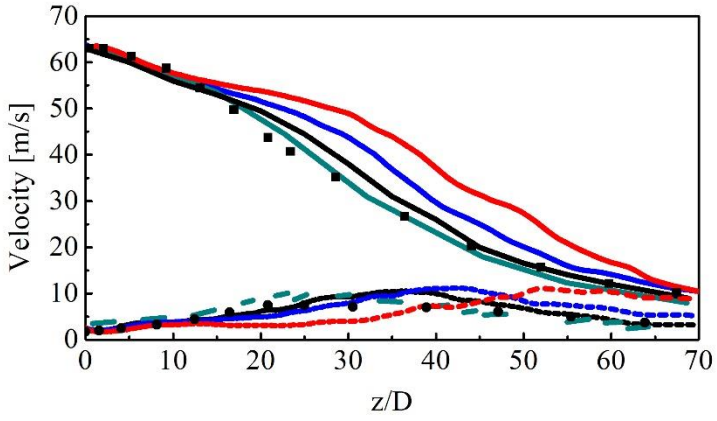

Figure 4.5 Mean and rms profiles of axial velocity along the centreline. Black solid line: mean value of series model in fine grid (i). The figure notation is the same as Figure 4.3.

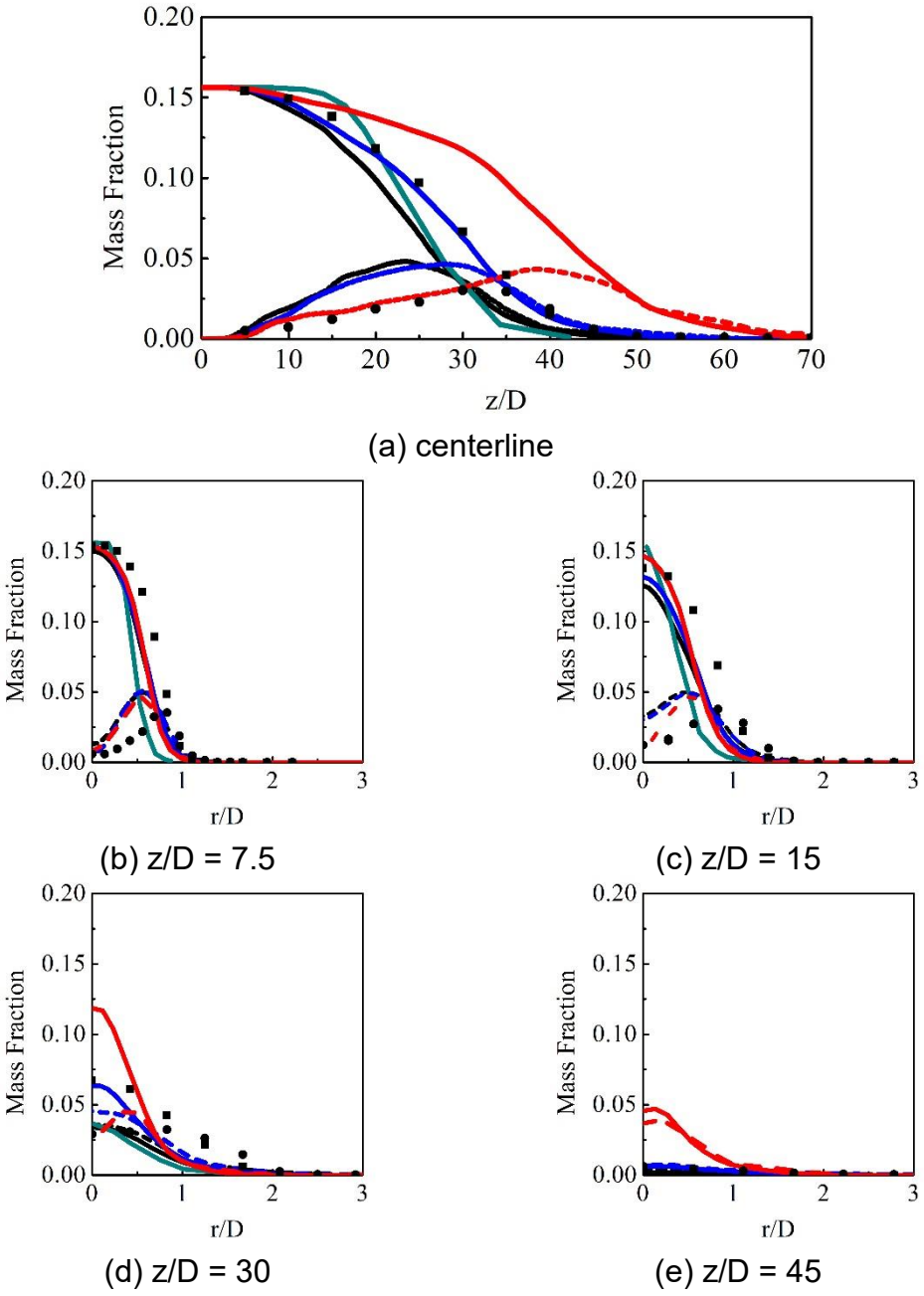

Figure 4.6 Mean and rms profiles of CH_4 mass fraction along the centreline and at different axial locations. The figure notation is the same as Figure 4.3.

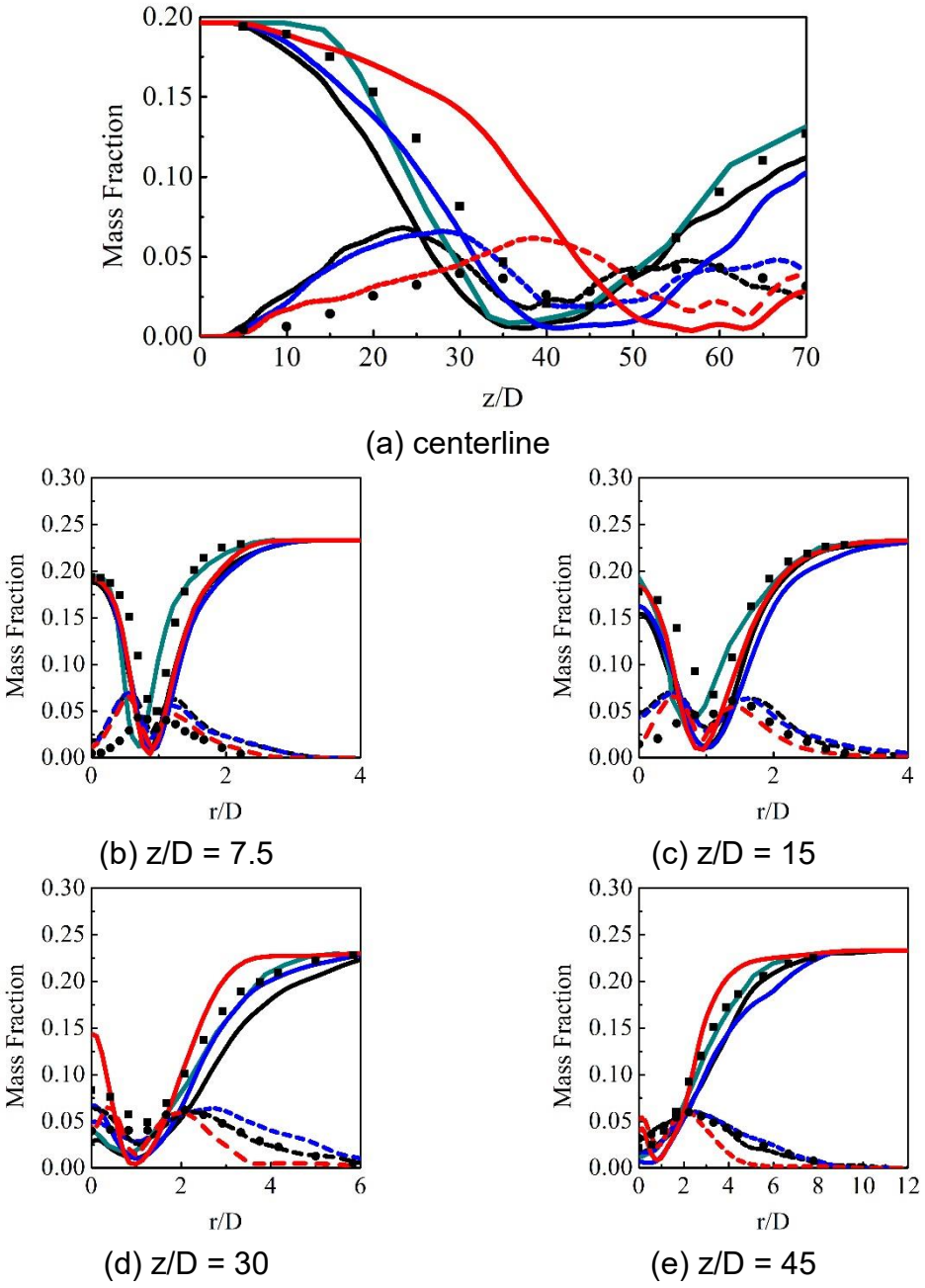

Figure 4.7 Mean and rms profiles of O_2 along the centerline and at different axial locations. The figure notation is the same as Figure 4.3.

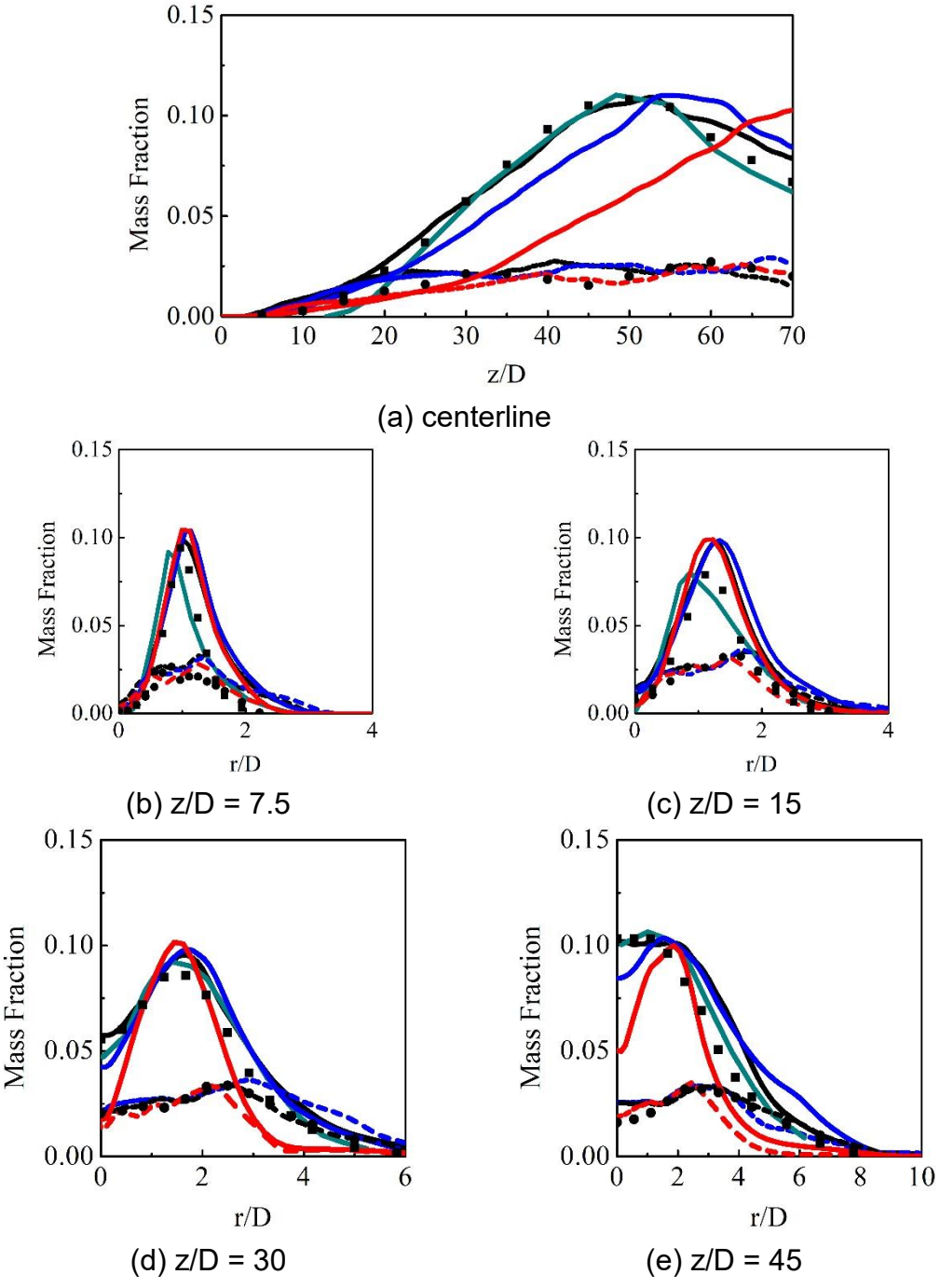

Figure 4.8 Mean and rms profiles of CO_2 along the centerline and at different axial locations. The figure notation is the same as Figure 4.3.

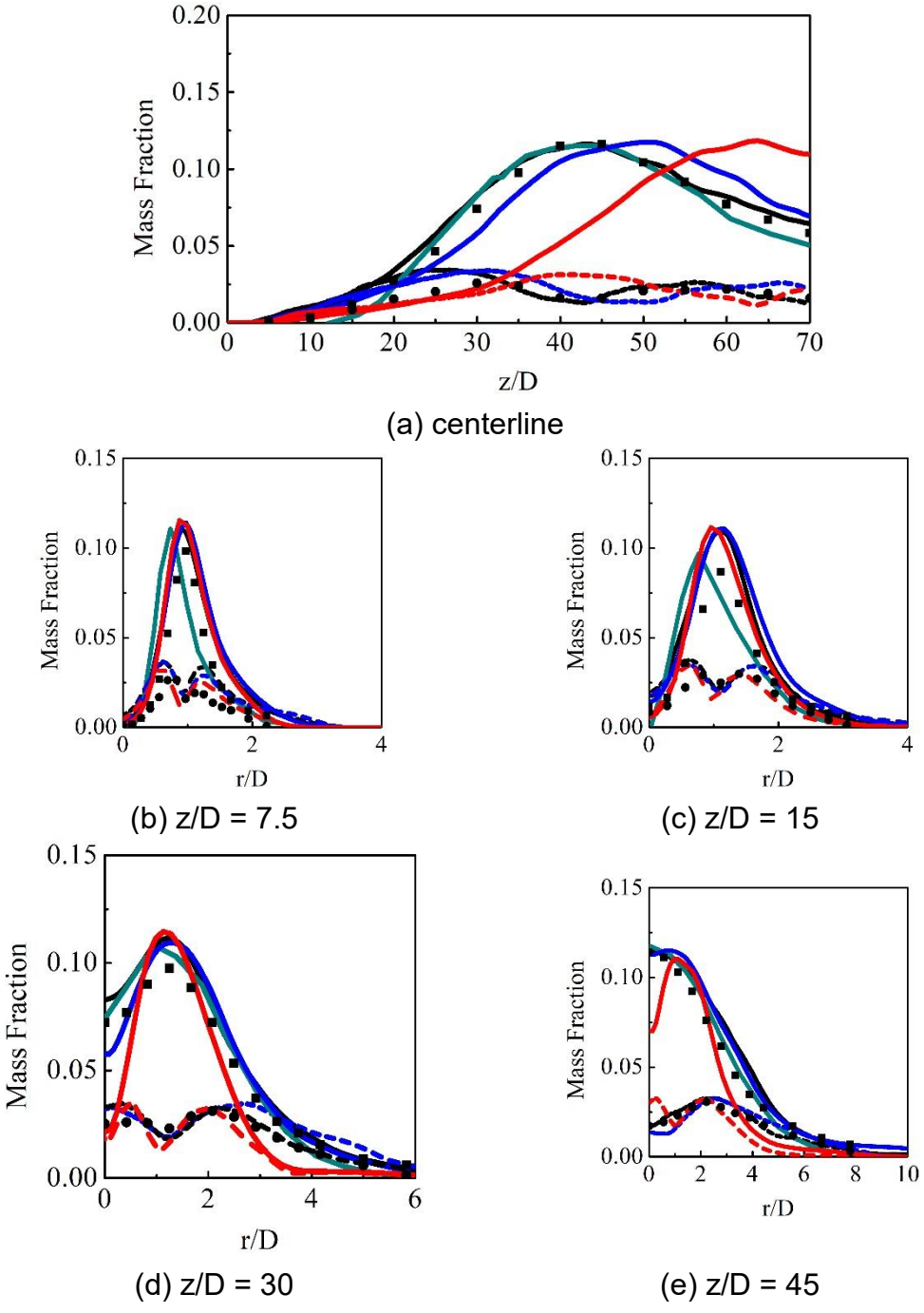

Figure 4.9 Mean and rms profiles of H_2O along the centreline and at different axial locations. The figure notation is the same as Figure 4.3.

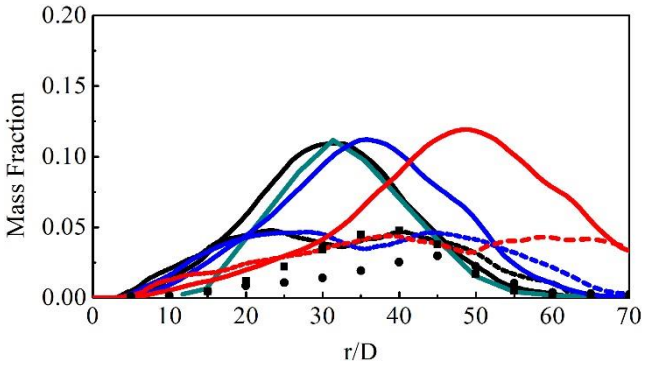

Figure 4.10 Mean and rms profiles of CO along the centreline and at different axial locations. The figure notation is the same as Figure 4.3.

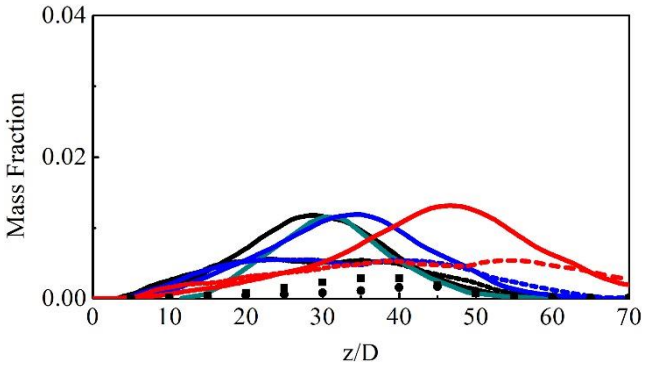

Figure 4.11 Mean and rms profiles of H_2 along the centreline and at different axial locations. The figure notation is the same as Figure 4.3.

4.3.2.2 Flame F

To compare, a set of published Flame F predictions by (Jones and Prasad, 2010) are imported in the following results plots, and are called the Jones results hereby. The main reason to select this publication as a reference is that it features the Eulerian stochastic field (ESF) method for combustion modelling. Besides, an augmented reduced mechanism (ARM) derived from the full GRI 3.0 mechanism is incorporated to describe the chemical reaction. For SGS stress, the dynamic Smagorinsky model is employed while the dynamic eddy viscosity model is used in this work. The numerical computations were carried out with a parallelized (by domain decomposition) second-order accurate finite-volume code called BOFFIN (boundary fitted flow integrator). The results presented are carried with a grid resolution of 81*81*160 nodes. The domain size has dimensions 20D*20D*50D, which is smaller than the series model simulations, so that the mesh is much more refined than that in this work. All boundary conditions are the same as those in this work, except a convective outflow condition has been applied at the outflow plane.

Statistical collection is performed over 16 burner flow-through times based on the jet bulk velocity. Prior to that, 10 burner flow-through times are simulated to ensure the flows established. All simulations are performed on the UK national supercomputing service Archer with 480 2.7 Ghz processors. The total simulation time for no SGS model in coarse grids, series model in coarse grids, and series model in fine grids are respectively 21hrs, 31hrs, and 59hrs. In comparison, The simulations were performed on a CRAY XT4 (AMD 2.6 GHz

dual core Opteron processor) on 512 CPU's, with about 1.5 days required for 15-20 flow through times.

Figure 4.12 depicts the mean and RMS profile of temperature along the centreline and radial distribution at different axial locations. Along the centreline, the profiles are reasonably accurate for the series model. An over-prediction of the mean temperature is notable, starting from z/D=15 to z/D=40, while an under-prediction is observed after z/D=55 in coarse grid resolution. Just like Flame D results, the RMS profile also duplicates the observations in the experiments that the minimum arises around the location of the maximum mean profile. This feature is not sensed by no SGS model either. For the radial profiles, the maximum temperatures are over-predicted by a larger margin than Flame D, and these similar observations are found in (Elbahloul and Rigopoulos, 2015, Vreman et al., 2008, Jones and Prasad, 2010). It could be attributed to the inaccuracies of the mechanism (either detailed or simplified) at high Reynolds number and the thermal radiation that is not considered in LES simulations. The Jones results produce a generally better agreement with the experimental data, but still suffer from over predictions of the peak temperature. However, it is also interesting to note that RMS profiles are reasonably good, except some minor discrepancies at 15D and 30D. The no SGS model behaves relatively bad especially at capturing the centreline trends.

The mean mixture fraction profile along the centre line and at different axial locations is depicted in Figure 4.13. The definition of mixture fraction here is the same as Equation 4.1 in the Flame D analysis. As can be observed at the

centreline, good agreement with measurements is obtained for the series model, with small over-prediction at the location Z/D=15 to 45. Remarkably, looking at the radial profiles, , there are very few discrepancies (except for slight over-predictions at the location z/D = 30) on both the fuel-rich and fuel-lean side, indicating the shape of the flame is accurately reproduced and there is no radial overspreading of the jet in the prediction of the series model. In this regard, the ESF model performs slightly better than the series model, in spite of the same over estimation at the location z/D = 30. For no SGS model, the difference from the experimental measurements is larger in the upstream and downstream right after z/D = 15.

Figure 4.14 describes the mean and RMS velocity distribution along the centreline. Clearly, both the mean quantities and RMS are reasonably well predicted for the series model in 2 grids, albeit with some minor acceleration after z/D = 20 in coarse grids and some slight under-prediction z/D = 45 in both meshs. For the no SGS model, the mean velocity is largely over-estimated right after z/D =20, and the over-estimation is also observed in the downstream after z/D= 40.

Figures from 4.15 depicts the mean and rms profile of CH_4 mass fractions along the centreline and radial distribution at different axial location. As the centreline profiles show, the reactants CH_4 consume faster than the experiments, identical to the predicted temperature trend. Such trends are also spotted in the Flame D predictions. For the radial profiles at different axial locations, the series model predicts a good trend, though the under-predictions are found on the fuel-rich

side at the locations z/D = 7.5, 15 and 30 as well. For the Jones simulations, the ESF model generates some over predictions on the fuel-rich side at the locations z/D = 15 and 30. For the RMS fluctuations, the ESF model performs better than the series model. It could be attributed to the detailed chemistry mechanism used and the much higher grid resolution in Jones simulation.

Figures from 4.16 shows the mean and rms profile of O_2 mass fractions along the centreline and radial distribution at different axial location. As the centreline profiles show, the oxidizer consumes faster than the experiments, identical to the predicted CH_4 trend. The discrepancies are also spotted in the Flame D predictions. It can be attributed to the same reason of the limitations of the simplified mechanism explained in the Flame D predictions. For the radial profiles at different axial locations, both the series model and ESF model predict a reasonable trend, though the under-predictions are found on the fuel-rich side at the locations z/D = 7.5, 15 and 30. For the RMS profile, the ESF performs better at capturing the fluctuations.

Figure 4.17 describes the mean and rms profile of CO_2 mass fractions along the centreline and radial distribution at different axial location. Along the centreline, the mean profile is well reproduced for the series model in 2 grids. The RMS values keep the same level as the experimental data, although slightly over-prediction appears in the upstream before z/D =30. For the radial distribution, an overall reasonable agreement with experimental data is achieved by the series model, except that the maximum value at x/D=7.5, 15 and 30 are overpredicted. Jones results predicted a better mean level to the

fine resolution simulation of the series model, though the peak mass fractions are also over predicted like the series model at location x/D = 7.5, 15 and 30. For the RMS value, both the ESF model and series model reproduce the fluctuation trend and level well.

Figure 4.18 depict the mean and rms profile of H_2O mass fractions along the centreline and radial distribution at different axial locations. Observed from the centreline comparisons, the mean profile is well reproduced for the series model, although some minor over-predictions are spotted before x/D = 40. The RMS values keep the same level as the experimental data, although slightly over-prediction appears in the upstream before z/D =30. For the radial distribution, an overall reasonable agreement with experimental data is achieved by the series model, except that the maximum value at x/D=7.5, 15, and 30 are slightly overpredicted. Jones results predicted a better mean level to the fine resolution simulation of the series model, though the peak mass fractions are also over predicted like the series model at location x/D = 7.5, 15 and 30. For the RMS value, both the ESF model and series model reproduce the fluctuation trend and level well. Overall, the series model is better at capturing the combustion product trend than no SGS model, especially along the centreline. When the grid is refined, the results improve.

Figures 4.19 and 4.20 exhibit the mean and rms profile of CO and H_2 mass fractions along the centreline and radial distribution at different axial location respectively. The mean profile of the both intermediates CO and H2 are

excessively over-predicted. It is almost out of the same mechanism reasons mentioned above, as explained in the part of Flame D predictions.

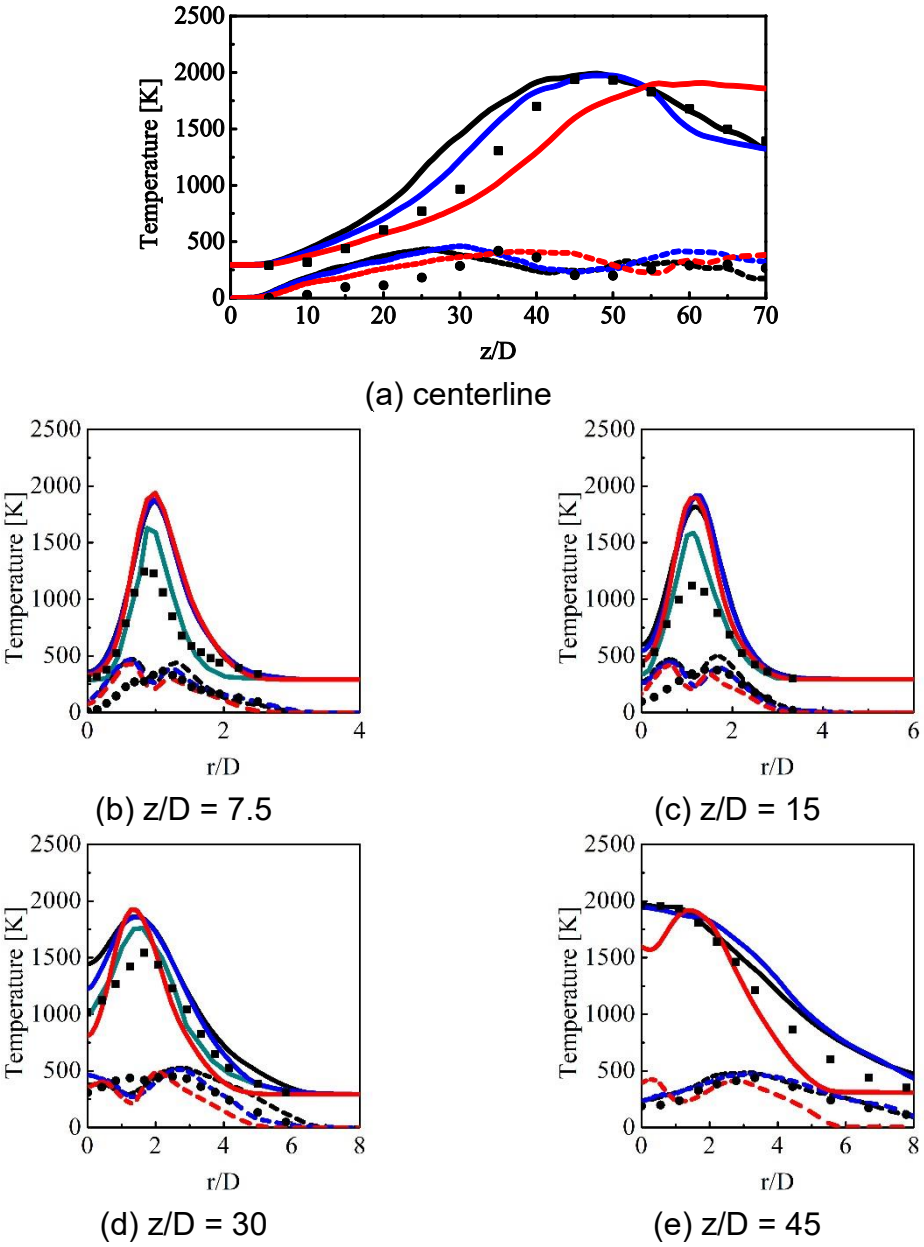

Figure 4.12 Mean and rms profiles of temperature along the centreline and at different axial locations for Flame F. Black solid line: mean value of series model in fine grid (i). Blue solid line: mean value of series model in coarse grid (ii). Red solid line: mean value of no-SGS model in coarse grid (iii). Square scatter: mean experimental data (Barlow and Frank, 1998) (iv). Black dashed line: rms value of series model in fine grid (v). Blue dashed line: rms value of series model in coarse grid (vi). Red dashed line: rms value of no-SGS model in coarse grid (vii). Round scatter: rms experimental data (Barlow and Frank, 1998) (viii). Green solid line: mean value of ESF model in Jones simulations (Jones and Prasad, 2010) (ix). Green dashed line: rms value of ESF model in Jones simulations (Jones and Prasad, 2010) (ix).

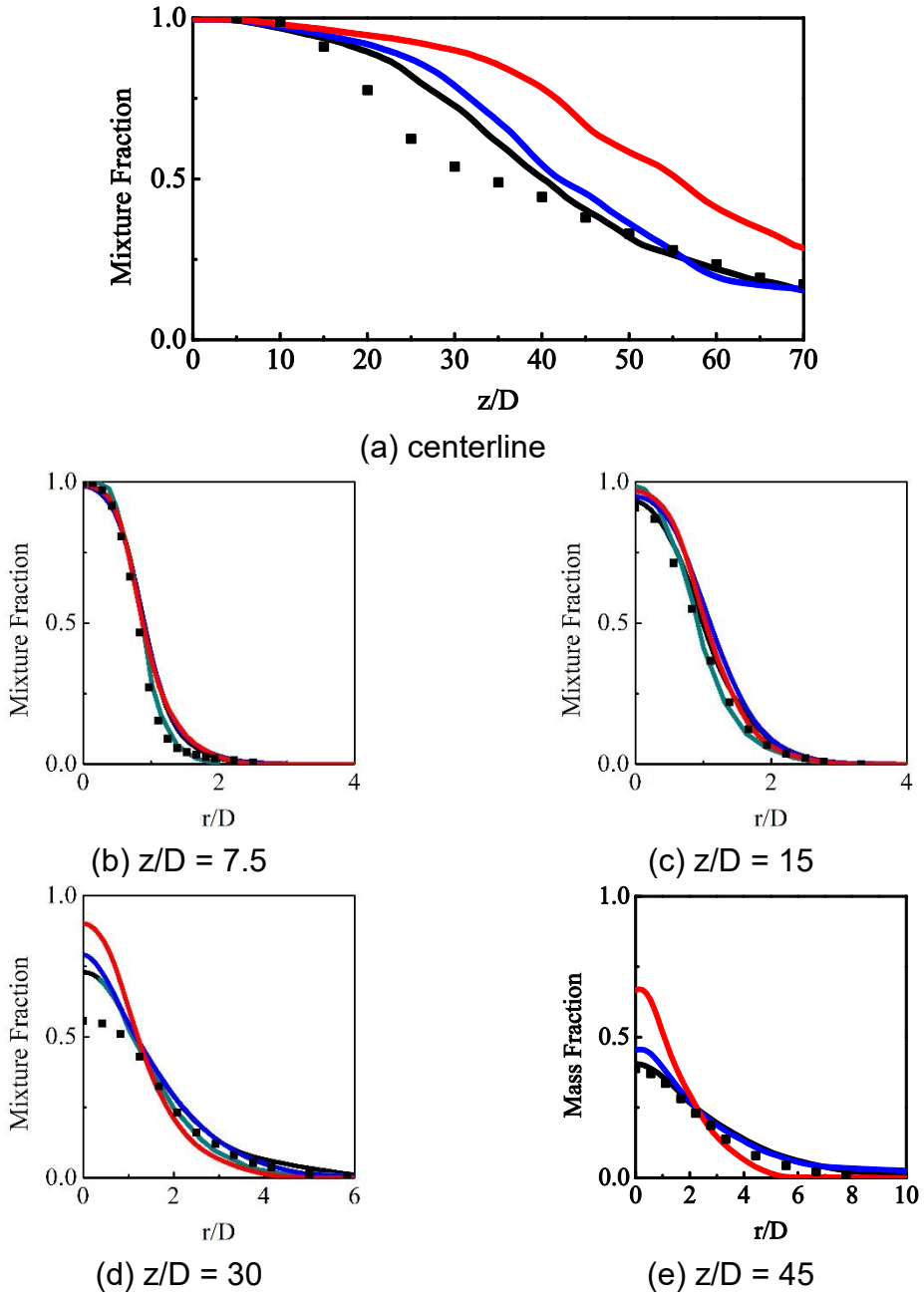

Figure 4.13 Mean profiles of mixture fraction (-) along the centerline and at different axial locations for Flame F. Black solid line: series model in fine grid (*i*). Blue solid line: series model in coarse grid (*ii*). Red solid line: no-SGS model in coarse grid (*iii*). Square scatter: experimental data (Barlow and Frank, 1998) (*iv*). Green solid line: mean value of ESF model in Jones simulations (Jones and Prasad, 2010) *(v).*

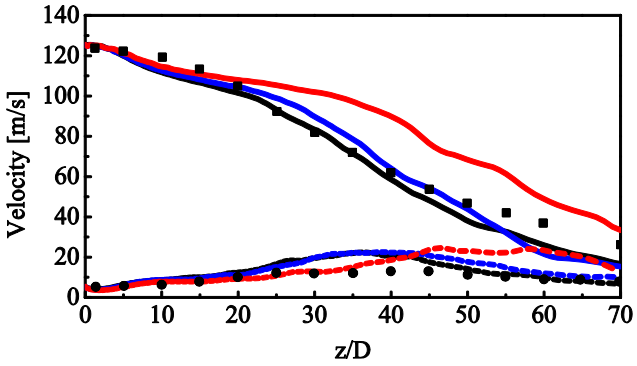

Figure 4.14 Mean and rms profiles of axial velocity along the centreline for Flame F. The figure notation is the same as Figure 4.12.

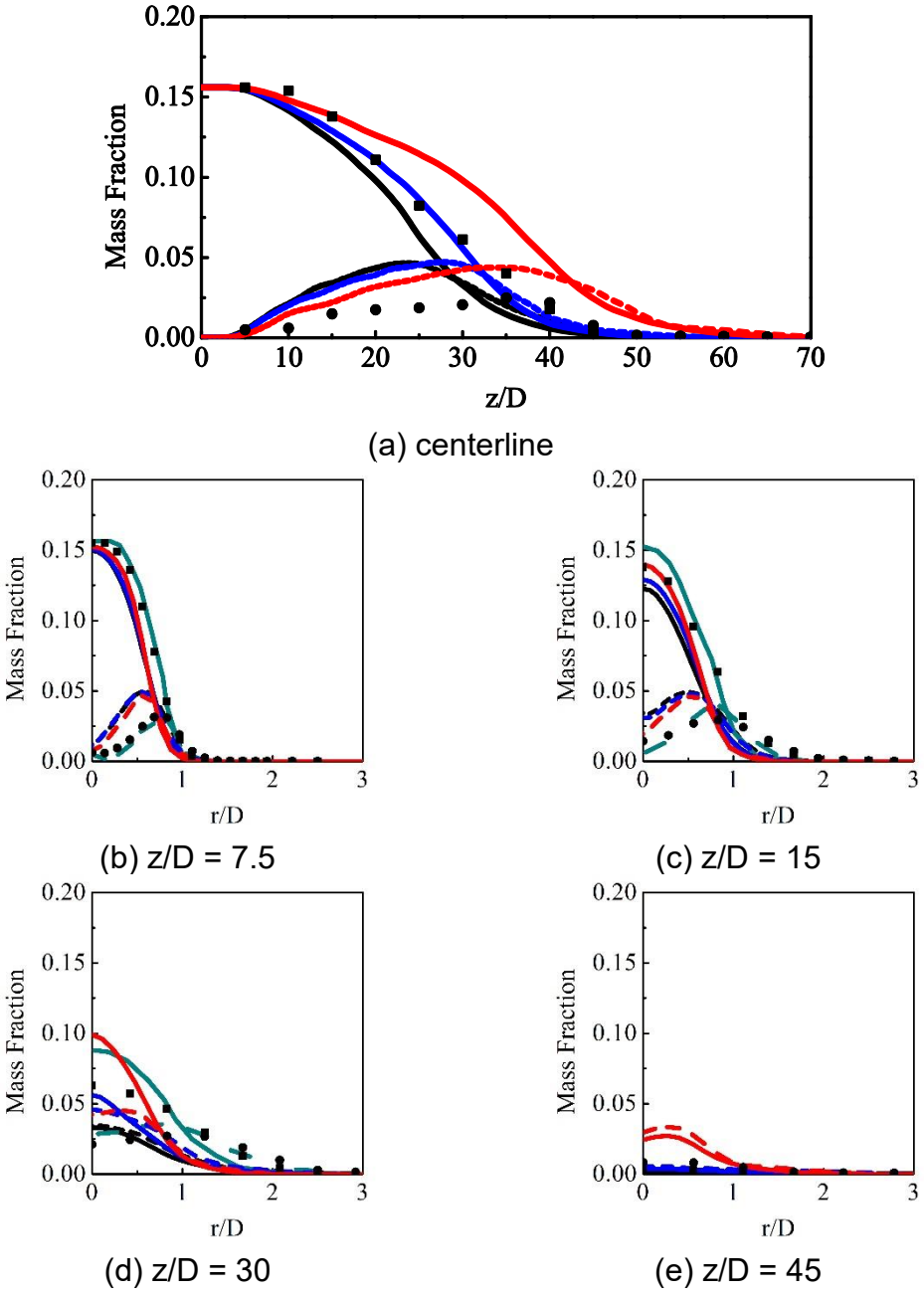

Figure 4.15 Mean and rms profiles of CH_4 mass fraction along the centerline and at different axial locations for Flame F. The figure notation is the same as Figure 4.12.

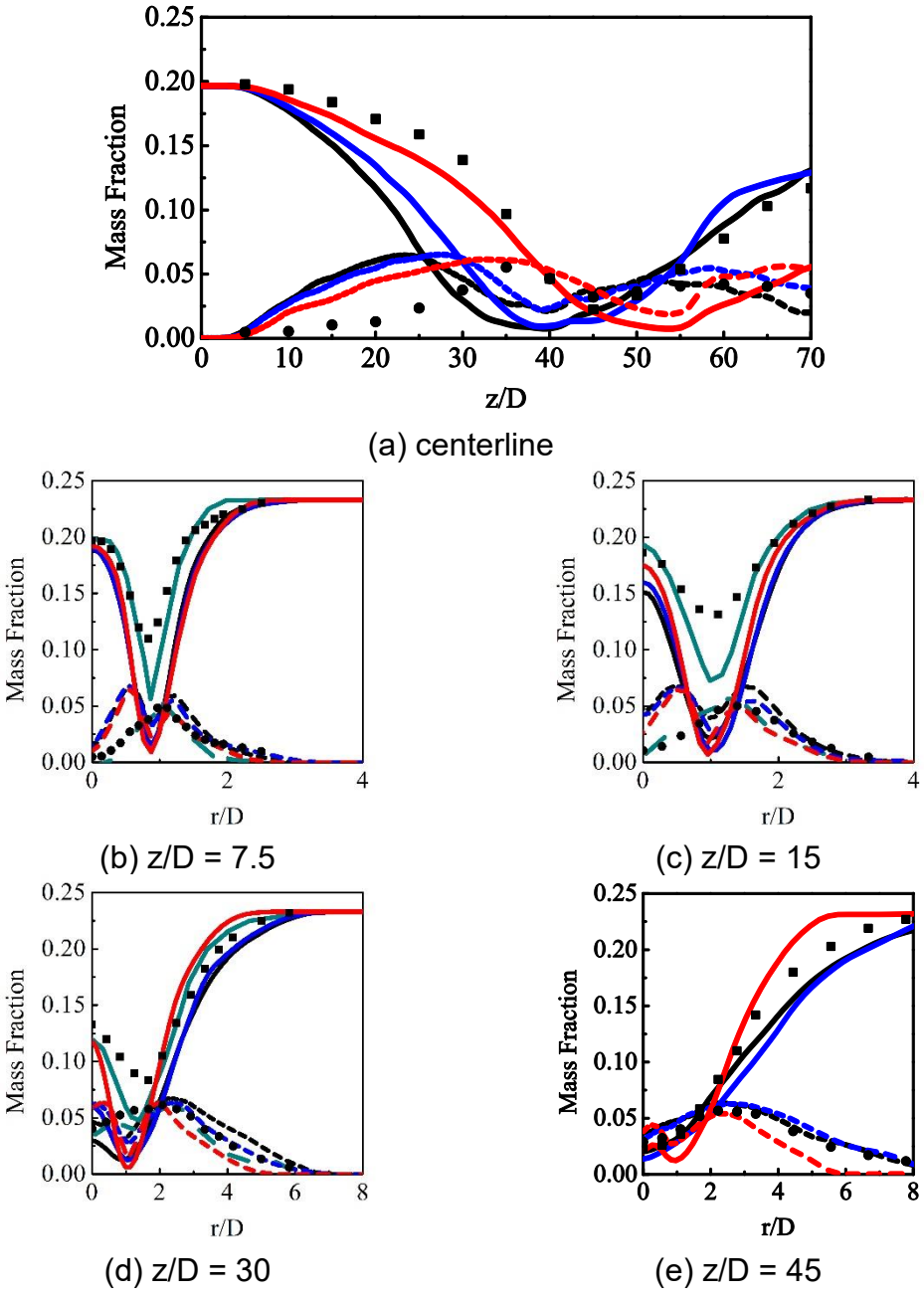

Figure 4.16 Mean and rms profiles of O_2 along the centerline and at different axial locations for Flame F. The figure notation is the same as Figure 4.12.

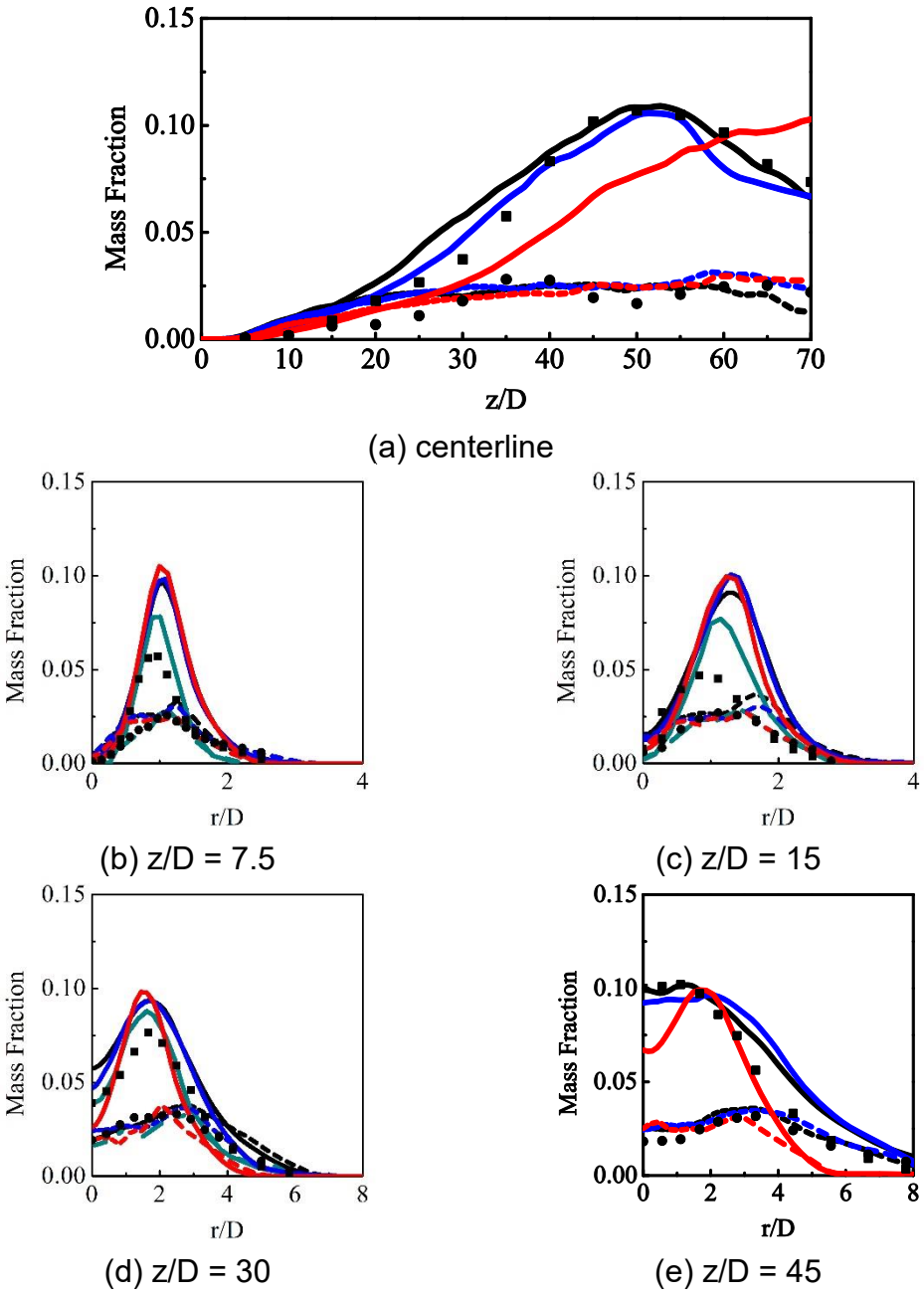

Figure 4.17 Mean and rms profiles of CO_2 along the centerline and at different axial locations for Flame F. The figure notation is the same as Figure 4.12.

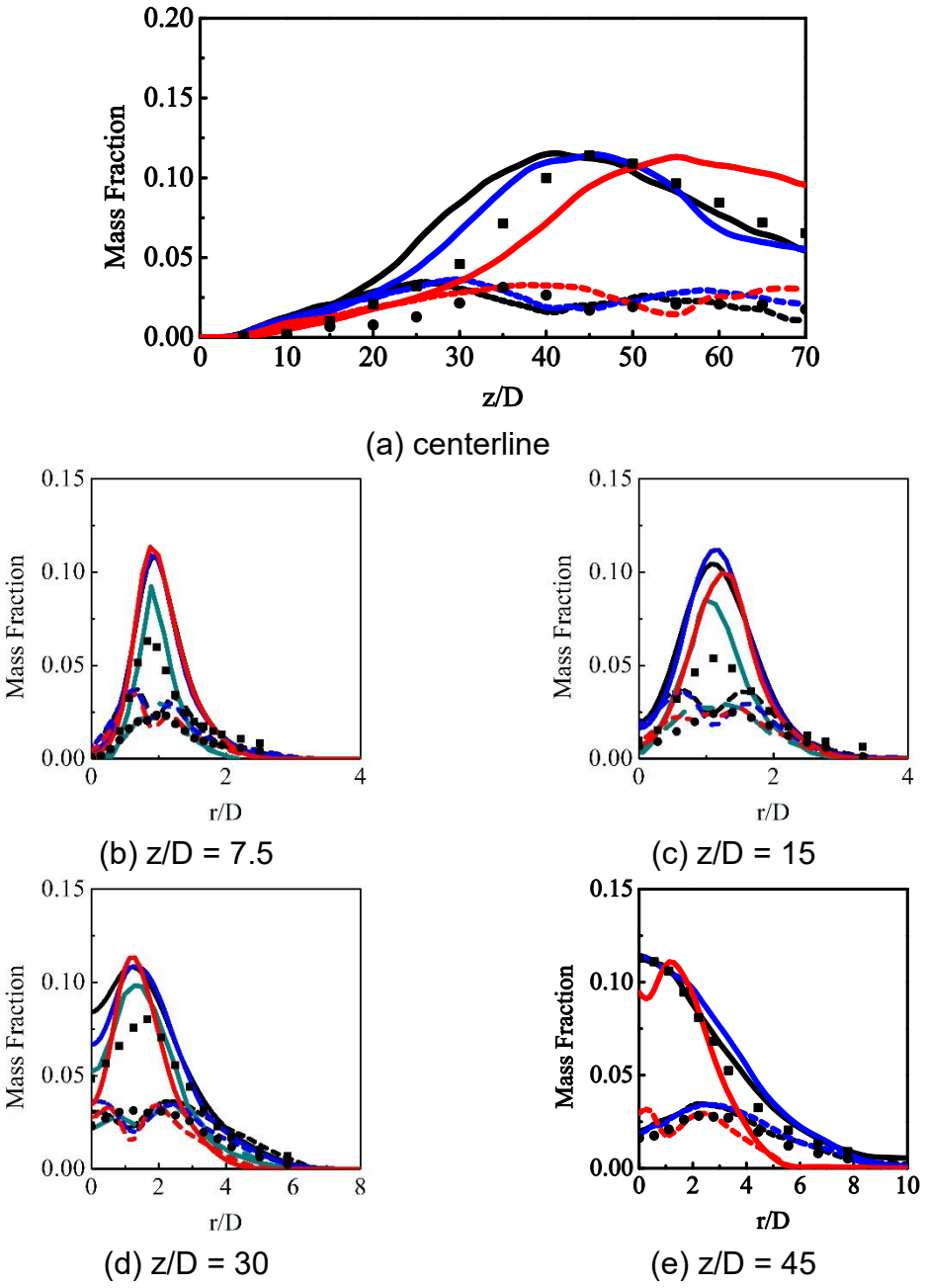

Figure 4.18 Mean and rms profiles of H_2O along the centerline and at different axial locations for Flame F. The figure notation is the same as Figure 4.12.

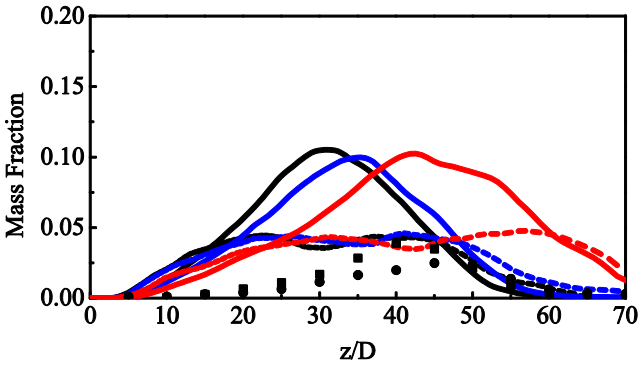

Figure 4.19 Mean and rms profiles of CO along the centerline and at different axial locations for Flame F. The figure notation is the same as Figure 12.

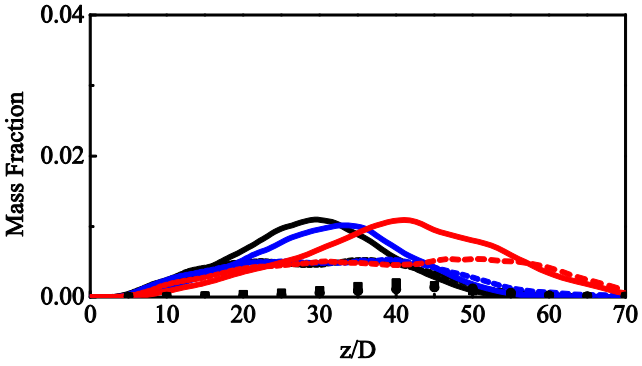

Figure 4.20 Mean and rms profiles of H_2 along the centerline and at different axial locations for Flame F. The figure notation is the same as Figure 12.

4.4 Summary

Sandia flame D and F were simulated using LES with the series method and no SGS model in comparison. Two grid resolutions aligned with polar coordinates are generated, with a square section (o-grid) in the centre to avoid too dense meshes in the centreline. The chemistry is described by a well-established 4-step mechanism with 7 species.

The results of the series model present generally very good agreement with the experimental data. The velocity field was captured very well. The mean and rms profiles of the mixture fraction, temperature and mass fractions of CH_4, O_2, CO_2, and H_2O were reasonably well reproduced for both Flame D and F. The discrepancies that arise in the intermediates H_2 and CO could probably be attributed to limitations in the simplified reaction mechanism used in the simulation.

Compared with Mustata`s simulation, the series model behaves similarly well to the ESF model in Flame D prediction, except the velocity field where the ESF model produce more accurate results, but the series model obtain better performance in mixture fraction reproducing.

Combining the Jones` results, both the series model and ESF model reproduce reasonably good trends of temperature and species fields in Flame F. The main discrepancy of both models comes from the over-prediction of the maximum temperature and species fields, though ESF model behaves better in this

regard. This can be improved potentially by increasing the grid resolution and adopting more detailed chemistry mechanisms.

In relation to the no SGS model, the series model accomplished a much better predicting capability. Refining the mesh resolution, the series model shows a good grid sensitivity.

The overall findings exhibit that series model is capable to reproduce non-premixed flames in high Reynolds number and provide a reasonably accurate prediction of the temperature, velocity and species fields.

5 Simulation of a Bunsen premixed flame

The previous chapter exhibited the capability of the series model to predict non-premixed turbulent combustion, and Sandia series piloted jet flames were reproduced well. The incentive of this chapter is to complement the previous studies and display the feasibility of the series model to predict premixed combustion accurately.

5.1 Introduction

For the feasibility of premixed combustion predicting, the F3 methane/air turbulent Bunsen flame studied experimentally by Chen (Chen et al., 1996) is chosen. The experimental object is a typical turbulent premixed flame with abundant velocity, temperature and scalar experimental database provided by (Chen et al., 1996), and has been used for model validation in LES by numerous researchers. Table 5.1 lists the literature review of the details of previous F3 flames LES simulation cases.

This chapter will be organized as the following parts. Initially, the experimental configuration and simulation setup will be presented with the flow length scale analysis. Next, instantaneous observations of the flame structure will be

presented. Last, Flow and flame statistics will then be compared with the experimental data.

5.2 Test case formulation

5.2.1 Experimental setup

A detailed depiction of the Bunsen burner setup is described in the article (Chen et al., 1996) is chosen for tests. Figure 5.1 shows the schematic of the burner design. The burner has an inner nozzle with a diameter D = 12 mm, where the fuel (a stoichiometric mixture of methane and air) is injected at different bulk velocities 30m/s, corresponding to a Reynolds number of Re = 23, 000. Surrounding the main fuel jet, a laminar pilot stream (the burning products of a stoichiometric mixture of methane and air) is generated by an array (1165 holes of the diameter 1 mm) of small jets issued through a cooled perforated plate to stabilize the turbulent flame(Dodoulas and Navarro-Martinez, 2013), and the outer diameter is 68mm. Outward, the fresh air is entrained as a form of a low-velocity co-flow. The experimental archive consist of radial distribution of the mean velocity, the mean and fluctuation of the temperature, the turbulent kinetic energy, as well as the mean mass fraction of CH_4, O_2, H_2O, CO_2, OH, and CO. The error in measuring the velocity and temperature is estimated to be 1% and 10%, while it becomes larger in terms of species mass fractions (for CH_4, CO_2, and CO, it is between 8 % and 15 %; in regard to O_2, OH and H_2O, it is around 20 % to 25 %.). In the diagram of the premixed regimes, the F3 flame is in the thin reaction zone, more precisely near the flamelet regime.

Table 5.1 Survey of previous F3 Bunsen Flames LES simulation cases (mostly in recent ten years)

Researchers	Turbulent SGS closures	Turbulent reacting LES closures	Simulation domain	Grid resolution	Chemistry mechanism	Code
(Pitsch and De Lageneste, 2002, de Lageneste and Pitsch, 2000)	Smagorinsky model	*G*-field	4D×4D×20D	64×64 × 296 (Cartesian coordinates)	GRI-MECH 2.11	Code of Center for Turbulence Research
(Knudsen and Pitsch, 2008)	Germano model	*G*-field and dynamic propagation model	6D×6D×30D	117 × 64 × 323(cylindrical coordinates)		In-house code
(Dodoulas and Navarro-Martinez, 2013)	Smagorinsky model	Eulerian stochastic fields approach	5D×5D×15D	56 × 36 × 112(Cartesian coordinates)	ARM for NO	BOFFIN
(De and Acharya, 2009a, De and Acharya, 2009b)	Dynamic Smagorinsky model	artificially thickened flame model	4D×4D×20D	94*64*300 (cylindrical coordinates)	A 2-step mechanism	In-house code
(Langella et al., 2015, Langella et al., 2017, Langella and Swaminathan, 2016)	Smagorinsky model	Dynamic modelling and Assumed PDF	20D×20D×40D	1.5 minion cells(Cartesian coordinates)	augmented reduced mechanism of GRI3.0	In-house code
(Wang et al., 2011)	dynamic Smagorinsky model	Dynamic thickened flame model	40D×40D×120D	Unstructured meshes	A single-step mechanism	In-house code

(Domingo and Vervisch, 2015, Domingo and Vervisch, 2017)	Vreman model	approximate deconvolution and explicit flame filtering	8D×8D×16D	194 × 194 × 306(Cartesian coordinates)	GRI	In-house code
(Volpiani et al., 2017)	Smagorinsky model	dynamic thickened flame model	40D×40D×120D	Unstructured meshes	A 2-step mechanism	In-house code
(Lindstedt and Vaos, 2006)	second moment closures	Transported PDF	Lagrangian particle	Lagrangian particle	Lindstedt reduced mechanism	In-house code
(Stöllinger and Heinz, 2008)	linear stress model	PDF method	6.5D×20D	70 * 220 (2D simulation)	DRM22	In-house code
(Schneider et al., 2005)	Smagorinsky model	G-equation	6D×6D×45D	345,000 cells (cylindrical coordinates)	Schmidt mechanism	FASTEST-3D

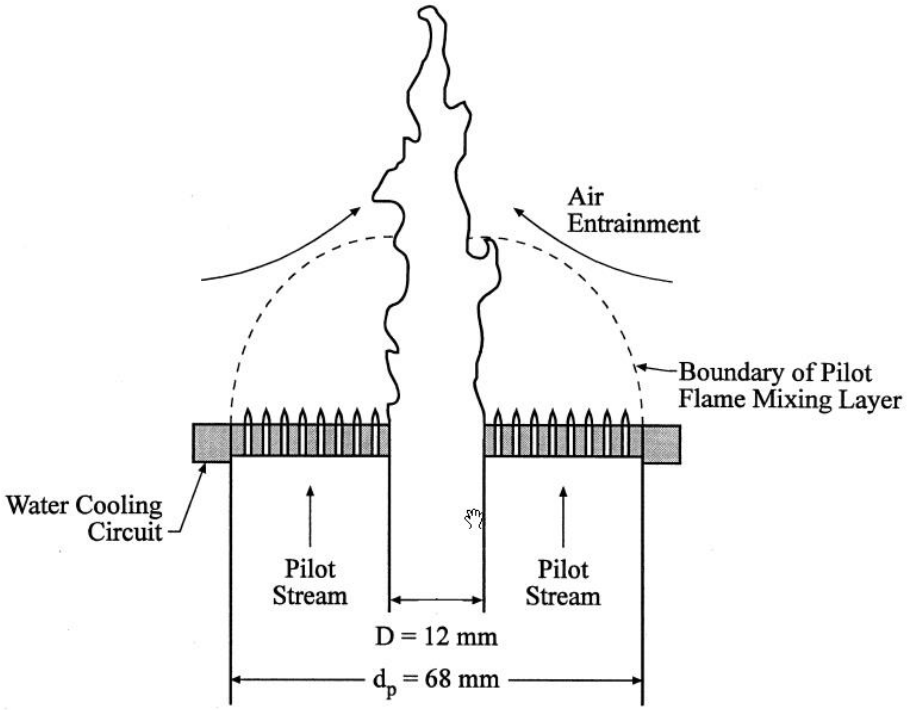

Figure 5.1 The burner design(Stöllinger and Heinz, 2008)

5.2.2 Simulation setup

The parameters for the F3 Bunsen flame is described in Table 5.2. It can be a guideline for the simulation setup. The computational domain is extended to 30D downstream the nozzle, and in the radial direction it is 12D in order to capture the downstream flame/temperature expansion. As Table 5.1 summarizes, the chosen domain is sufficient for the flame propagation. The grid used is mostly aligned with polar coordinates, but in the centre, a square section (*o*-grid) is applied to avoid very fine meshes in the centerline. Two resolutions are employed: a fine grid of 200 nodes in the radial direction, 81 points in the tangential direction, and 48 points in the azimuthal direction; and a coarse one,

which is approximately downscaled with a factor of 1.5 in each direction (134, 58, 36). Grids are stretched in both radial and axial directions to capture the strong gradients that stems close to the inlet and in the shear layers. The sketch of simulation domain and grid allocation is shown in Figure 5.2.

Table 5.2 Parameters for the F3 flame

Parameter	Expression	Value
Main jet nozzle diameter (Characteristic Length)	D	12mm
Integral Length Scale	L_I (=D)	12mm
Bulk Inlet Velocity (Characteristic Flow Velocity)	U_{in}	30m/s
Macroscopic Reynolds Number	Re_{sh}	23,000
Inlet Temperature	T_{in}	298K
Nominal Pressure	P	101kPa
Kolmogorov Length Scale	$Re_{sh}^{-3/4}D$	6.4 μm
Cold Flow Filter Width (Pope's Criterion(Wang et al., 2011))	$\triangle=0.083L_I$	0.996mm
Shear Layer Fluctuation (meatured)	u'	2.1m/s
Integral Time Scale	$t_I= L_I / u'$	5.7ms
Kolmogorov Time Scale	$Re_{sh}^{-1/2}/t_I$	1.2us
CFL Criterion Time Scale	$C_{max}\triangle /(U_{in}+U_{sound})$	2.6us

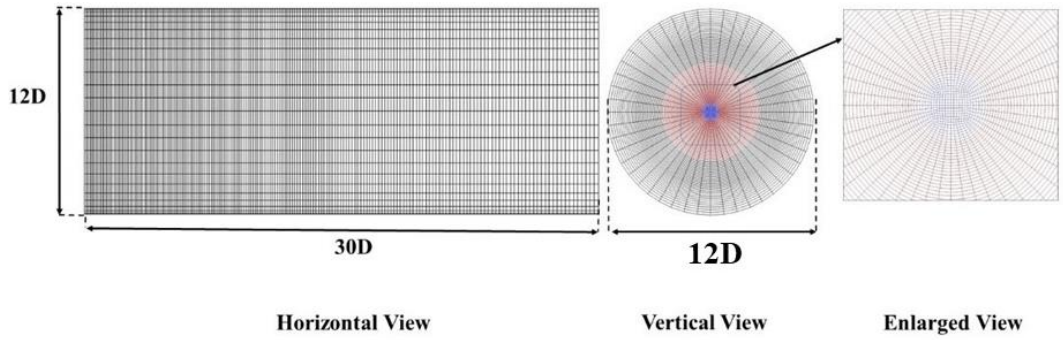

Figure 5.2 A sketch of simulation domain and grid allocation. Blue area: main jet. Red area: pilot stream.

At the inlet boundary, the mean velocity profiles are prescribed with the detailed flow field experimental data (Chen et al., 1996) above the nozzle exit. The inlet turbulence intensities is imposed with the method of random spots by Kornev and his co-workers(Kornev and Hassel, 2007a, Kornev and Hassel, 2007b, Kornev et al., 2007). For the main jet species, flat profiles are specified using the measurements(Chen et al., 1996). The pilot composition was computed using chemical equilibrium and for enthalpies corresponding to adiabatic conditions as well as for 10% heat losses to the burner(Lindstedt and Vaos, 2006). The pilot temperature is 2005K. Free slip conditions are used for the lateral boundary, while a non-reflecting outflow conditions are used at the outflow plane. A second order implicit backward differencing scheme is employed for time marching. A variable time step is utilised, with compressible Courant number restriction of 0.2. The chemical mechanism used in the present work is the one proposed by Jones and Lindstedt (Jones and Lindstedt, 1988) with 4 reactions and 7 species. Statistical collection is performed over 15 burner flow-through times. Prior to that, 8 burner flow-through times are simulated to

ensure the flows established. Besides the series model, a no SGS model neglecting the SGS part in the chemical source term ($\overline{\dot{\omega}_\alpha(\varphi_1, \varphi_2, \ldots, \varphi_k)} = \dot{\omega}_\alpha(\overline{\varphi_1}, \overline{\varphi_2}, \ldots, \overline{\varphi_k})$) is employed to be a comparison test.

5.3 Results

5.3.1 Flame structure

Snapshots of the instantaneous temperature, velocity and species distribution in a fully-developed flow field are shown in Figure 5.3. They are taken from the fine grid simulation. From the temperature field, the flame structure displays the conventional characteristics of premixed combustion: the flame is divided by the flame front (represented by the heat release) into two distinct regions, hot product zone and unburn mixture region. The high temperature pilot stream continuously ignites the unburnt mixture from the main jet. The much larger velocity in the pilot acts a role in stabilizing the burnt product. Meanwhile, air entrainment happens between the pilot and coflow streams. The highest temperature arises in the vicinity behind the flame front. Observing the O2, air entrainment happens near the region of pilot jet. For the major product, H2O and CO2 continuously convect downstream after generation near the reaction region. The velocity field is turbulent and gradually decreases along the centerline. However, it is worth noting that in the area from z/D=6 to z/D=12, the axial velocity is accelerated. This is due to the heat release from the reaction zone and identical to the experimental observation(Chen et al., 1996). Overall,

the shape of the flame (temperature and species fields) is largely distorted on the account of turbulence.

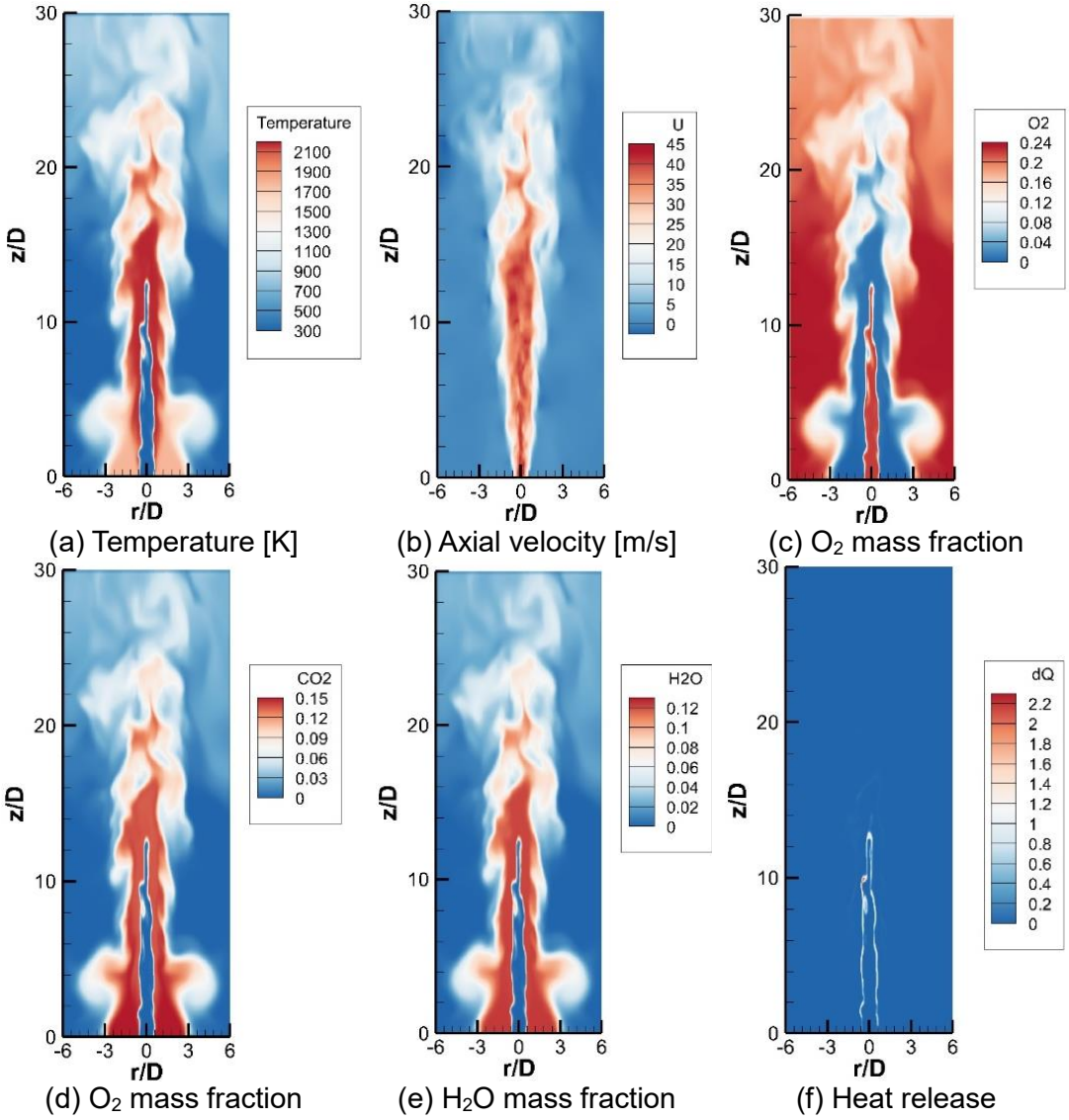

(a) Temperature [K] (b) Axial velocity [m/s] (c) O_2 mass fraction

(d) O_2 mass fraction (e) H_2O mass fraction (f) Heat release

Figure 5.3 The instantaneous field of temperature, axial velocity, heat release and species mass fractions.

5.3.2 Statistical results

To compare, a set of published F3 predictions by (Domingo and Vervisch, 2015) are imported in the following results plots, and are called the Domingo results. The main reason to select this publication as a reference is that it adopts a similar mathematical approach based on Taylor series expansion for combustion closures, as pointed out in Part 1. The difference is that the series expansion is on the scalar field rather than the chemical source term in this study. The model is called ADEF (Approximate Deconvolution and Explicit flame Filtering). Besides, an augmented reduced mechanism (ARM) derived from the full GRI 3.0 mechanism is incorporated to describe the chemical reaction. For SGS stress, the Vreman model is employed while the dynamic eddy viscosity model is used in this work. The numerical computations were carried out with using the SiT-Com parallel flow solver. This solver is based on an explicit Finite Volumes scheme for Cartesian grids. The Navier–Stokes equations are in their fully compressible form together with scalars balance equations. The results presented are carried with a grid resolution of 194*194*306 nodes. The domain size has dimensions 8D*8D*16D, which is smaller than the series model simulations, so that the mesh is much more refined than that in this work. The inlet boundary conditions are the same as those in this work, while other boundary conditions are not specified in the publication.

Statistical collection is performed over 15 burner flow-through times based on the jet bulk velocity. Prior to that, 8 burner flow-through times are simulated to ensure the flows established. All simulations are performed on the UK national supercomputing service Archer with 480 2.7 Ghz processors. The total simulation time for no SGS model, series model in coarse grids, and series model in fine grids are respectively 21hrs, 28hrs, and 67hrs.

Figures 5.4 and 5.5 respectively depict the radial profiles of mean temperature and mean progress viarable defined by $c = (T-T_u)/(Tb-T_u)$ at different axial locations. Here, T_u = 298K is the temperature of co-flow air, T_b=2248K is the adiabatic temperature of the flame, T is the local mean temperature. The trends of the mean temperature and progress variable radial distribution present overall good agreement with the experimental measurements, though their maxima are over-predicted especially closer to the nozzle. However, different researchers (Dodoulas and Navarro-Martinez, 2013, de Lageneste and Pitsch, 2000, De and Acharya, 2009a, Lindstedt and Vaos, 2006) obtained the same discrepancies related to experimental measurements (largely extending 10–25 % experimental uncertainties) using both global and detailed mechanisms. This is due to the uncertainties of temperature fields in the pilot stream, where a large portion of heat is lost to the burner exteriors. Besides, it may also originate from the thermal radiation that is not considered in LES simulations. On top of this, a lower temperature can be set on the pilot boundary layer in future studies.

Figure 5.6 shows the radial profiles of mean axial velocity for both grid resolutions at different axial locations. In overall, the series model predicts the

velocity distribution very well in both meshes. At axial locations z/D= 2.5, 4.5, 6.5, the velocity is slightly over-predicted. At the further downstream location z/D = 85, a larger under-prediction is observed in coarse grids results, while good match is achieved in fine grids. In Domigo`s simulation, the ADEF model performs slightly better than the series model, with minor under-predictions at the locations z/D = 25 and 85.

The radial profiles of CH_4 mass fraction at different axial locations are pointed out in Figure 5.7. On the whole, the series model obtains a good agreement with the experimental data, with some under-predictions on the fuel-lean sides. Compared with the Domingo`s simulations, the ADEF model performs a little worse than the series model, with under-estimations on the both fuel-lean and fuel-rich sides at all the locations. For the no SGS model, the results suffers mainly from the over predictions on the fuel-rich side at the downstream locations z/D = 6.5 and 8.5.

Figure 5.8 describes the radial profiles of O_2 mass fraction at different axial locations. The distribution of the oxidizer, indicating the entrainment of co-flow air, is reasonably reproduced by the series model in both grid resolutions. Slight under-predictions are observed on the fuel-rich side, and minor over-predictions are spotted on the fuel-lean side at the locations z/D = 6.5 and 8.5. The ADEF model behaves very similarly to the series model in fine grids in the upstream, but obtains more under-predictions near the centerline at the locations z/D = 6.5 and 8.5. For the no SGS model, the results are on the whole worse than the series model, especially on the fuel-lean side.

Figure 5.9 outlines the radial profiles of CO_2 mass fraction at different axial locations. The distribution of the combustion product achieves a reasonably good agreement by the series model in both grid resolutions. Slight under-predictions are observed on the fuel-lean side; at the locations z/D = 2.5, 6.5 and 8.5, the results improve with the increase of grid resolutions. The ADEF model also obtains good predictions, with minor under-predictions on the fuel-lean side at the location z/D = 6.5 and slight over-estimation on the fuel-rich side at the location z/D = 8.5. For the no SGS model, the results are overall worse than the series model, especially on the fuel-lean side.

Figure 5.10 outlines the radial profiles of H_2O mass fraction at different axial locations. The distribution of the combustion product achieves a strikingly good agreement by the series model, especially in the fine grid resolution. Very slight over-predictions are observed around the peak value at the location z/D = 6.5. The results improve with the increase of grid resolutions. For the Domingo`s simulation, the ADEF model also obtains worse predictions than the series model in the fine grid, mainly due to the over-predictions on the fuel-rich side at the locations z/D = 4.5, 6.5 and 8.5. For the no SGS model, the results are overall worse than the series model, especially on the fuel-lean side. Notably, near the edge, more discrepancies are found in the no SGS model results, this is probably due to the O_2 over-prediction in Figure 5.8. The no SGS model doesn’t reproduce the air entrainment from the coflow air reasonably.

The mean mass fraction distribution of CO is displayed in Figure 5.11 Surprisingly, the radial profiles of the intermediate species CO are accurately

captured under the consideration of the simple 4-step mechanism used. For the ADEF model, the results are worse than the series model, as the location and value of the mass fraction peak are under-predicted. Generally, with the series model, the CO products are less sensitive to grid resolutions than major species, as much less difference is found with grid refinement.

In order to investigate influence of the temperature discrepancies, a new progress variable is established based on a linear combination of species mass fractions(Ihme et al., 2012):

$$c^* = \frac{Y_{CO_2} + Y_{CO}}{(Y_{CO_2} + Y_{CO})_{pilot}} \tag{5.1}$$

The radial distribution is depicted in Figure 5.12 and compared with experimental measurements. In this sense, the progress variable based on species demonstrates a reasonable and much better agreement than the progress variable defined by temperature. The trend is obvious even in the vicinity near the nozzle exit, where large discrepancies in the mean temperature are detected. It suggests that the temperature prediction is subjective to heat loss uncertainties in the pilot stream, and a simulation with a portion upstream of the nozzle exit should be a feasible option to solve the problem.

Comparing the predictions between the coarse and fine meshes, it is apparent to conclude that both the progress variable, axial velocity and the mean mass fractions for all species are reproduced more precisely in the fine mesh than the coarse grid results. In particular, the coarse grid simulation underestimates

the progress variable and the product of H_2O and CO_2 at all axial locations. It is due to larger portion energy resolved with grid refinement and the good limit features of the series model. Compared between 2 models, no SGS model behave much worse, especially in reproducing the species and progress variable as expected, as it lacks of capturing the information below sub-grid scales.

It is also interesting to compare with the simulations of (Domingo and Vervisch, 2015), who adopted a similar approach of employing the Taylor expansion of scalar field. In contrast, the fine grid results of the series model perform better in capturing the CH_4, CO_2, H_2O and CO, and slightly worse in predicting the velocity field. Considering that Domingo simulation employs better grid resolution and detailed chemistry mechanism, the series model shows the potential improvement in further adjustments (like using finer mesh or/and more detailed chemistry).

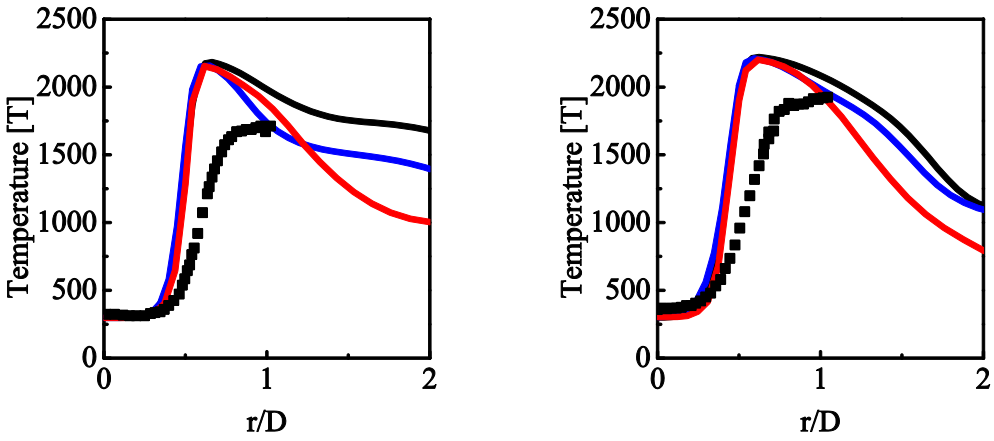

(a) z/D = 2.5

(b) z/D = 4.5

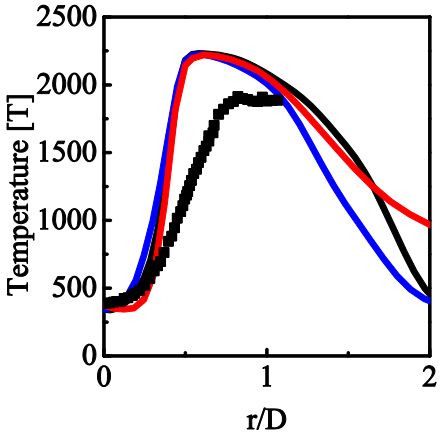

(c) z/D = 6.5

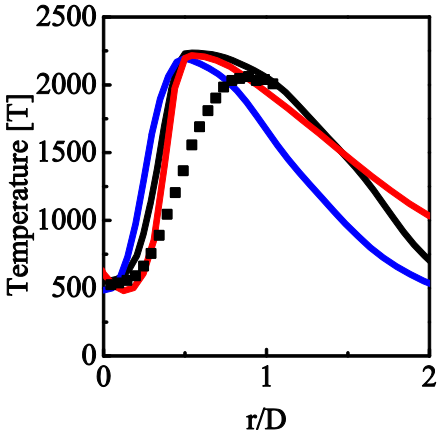

(d) z/D = 8.5

Figure 5.4 Mean profiles of temperature at different axial locations. Black solid line: series model in fine grid (i). Blue solid line: series model in coarse grid (ii). Red solid line: no-SGS model in coarse grid (iii). Square scatter: experimental data (Chen et al., 1996) (iv).

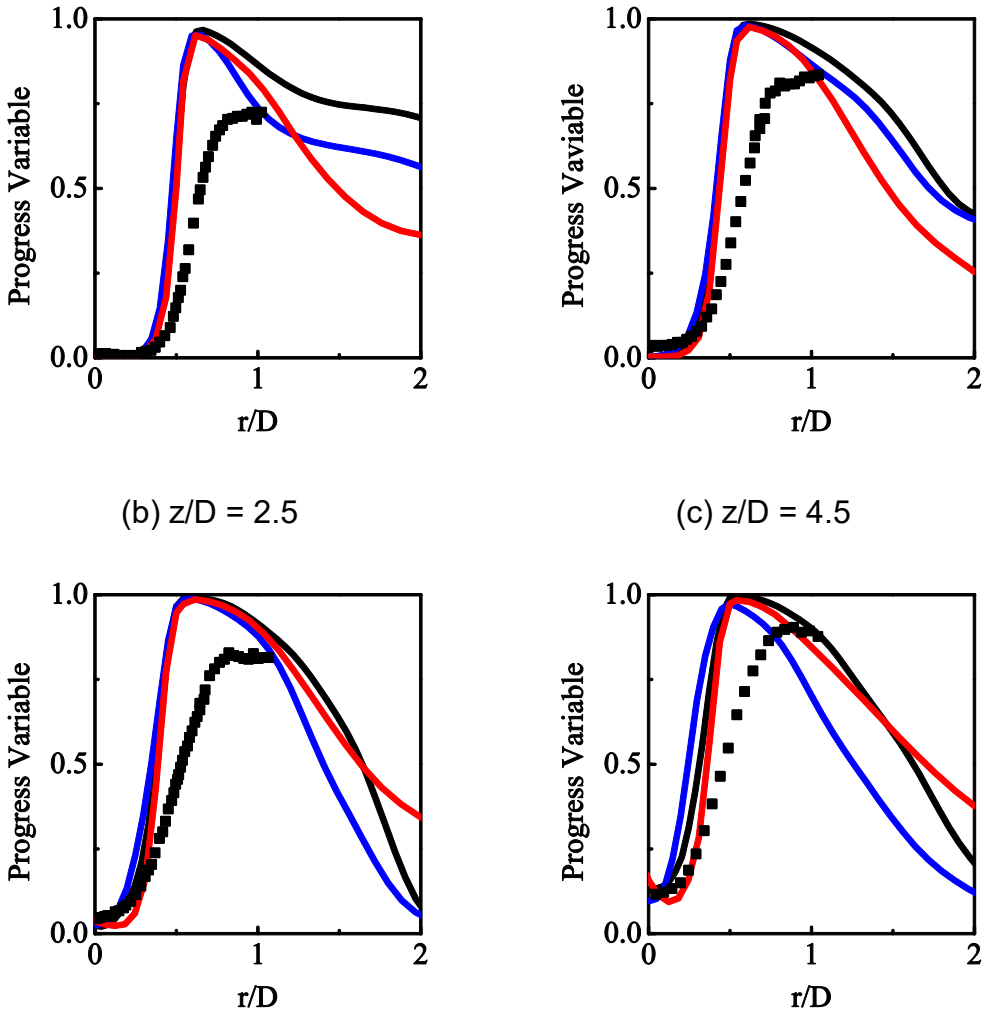

(b) z/D = 2.5

(c) z/D = 4.5

(d) z/D = 6.5

(e) z/D = 8.5

Figure 5.5 Mean profiles of progress viable c (temperature based) at different axial locations. Black solid line: series model in fine grid (i). Blue solid line: series model in coarse grid (ii). Red solid line: no-SGS model in coarse grid (iii). Square scatter: experimental data (Chen et al., 1996) (iv).

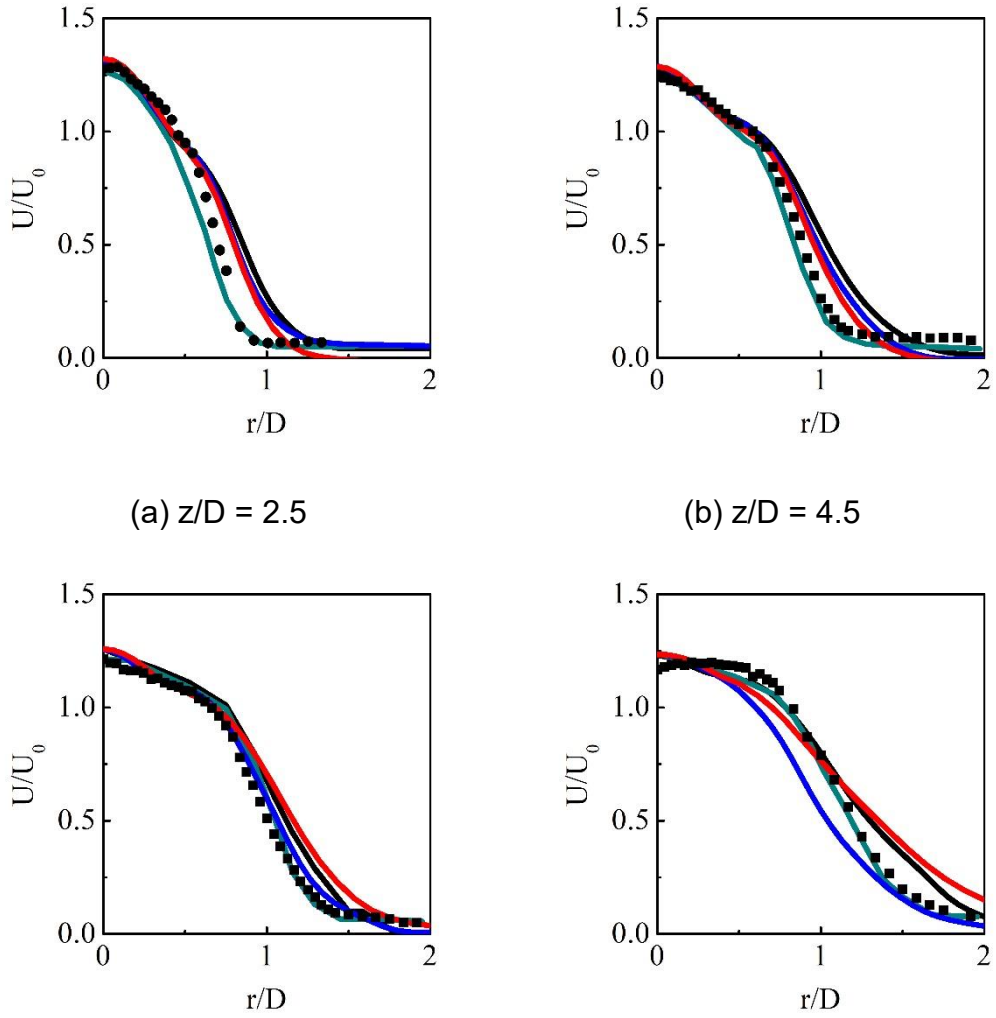

(a) z/D = 2.5

(b) z/D = 4.5

(c) z/D = 6.5

(d) z/D = 8.5

Figure 5.6 Mean profiles of axial velocity at different axial locations. Black solid line: series model in fine grid (i). Blue solid line: series model in coarse grid (ii). Red solid line: no-SGS model in coarse grid (iii). Square scatter: experimental data (Chen et al., 1996) (iv). Green solid line: the Domingo`s simulation (Domingo and Vervisch, 2015) (v)

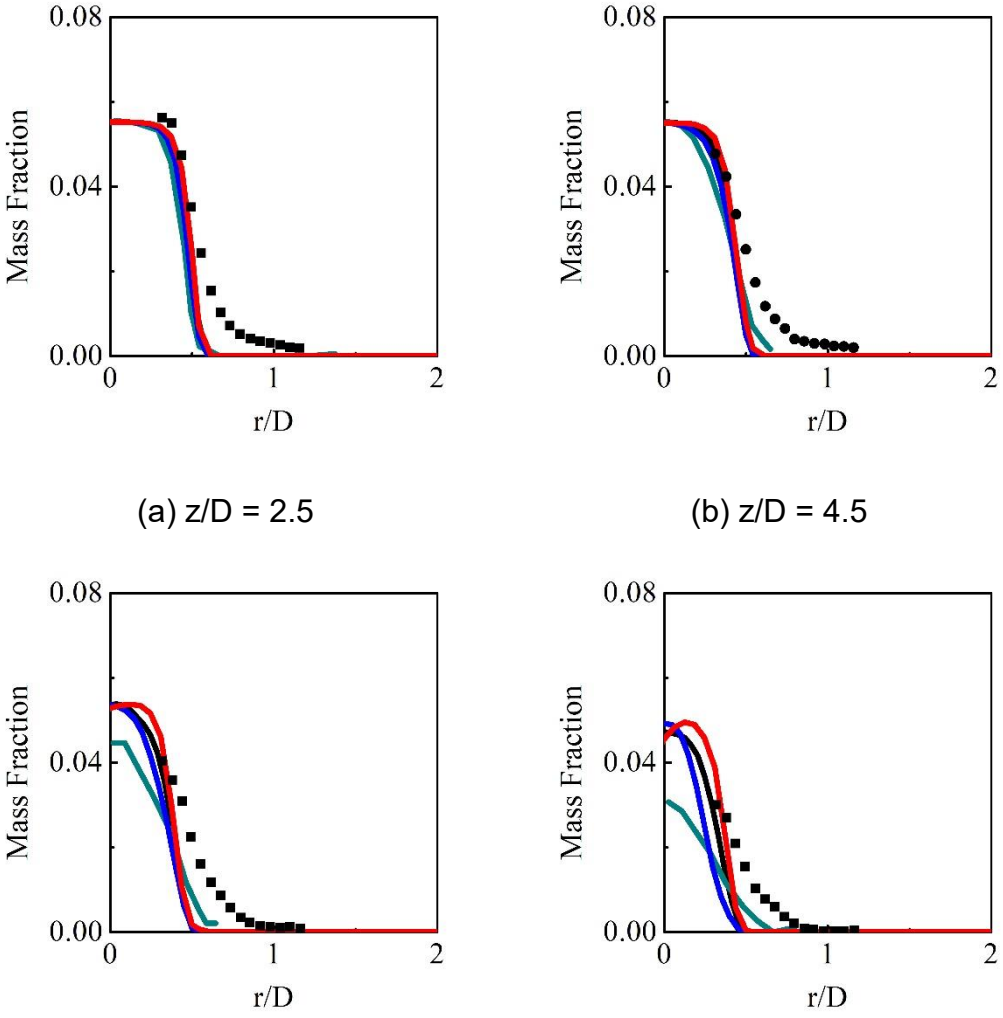

(a) z/D = 2.5

(b) z/D = 4.5

(c) z/D = 6.5

(d) z/D = 8.5

Figure 5.7 Mean profiles of CH_4 mass fraction at different axial locations. The figure notation is the same as Figure 5.6.

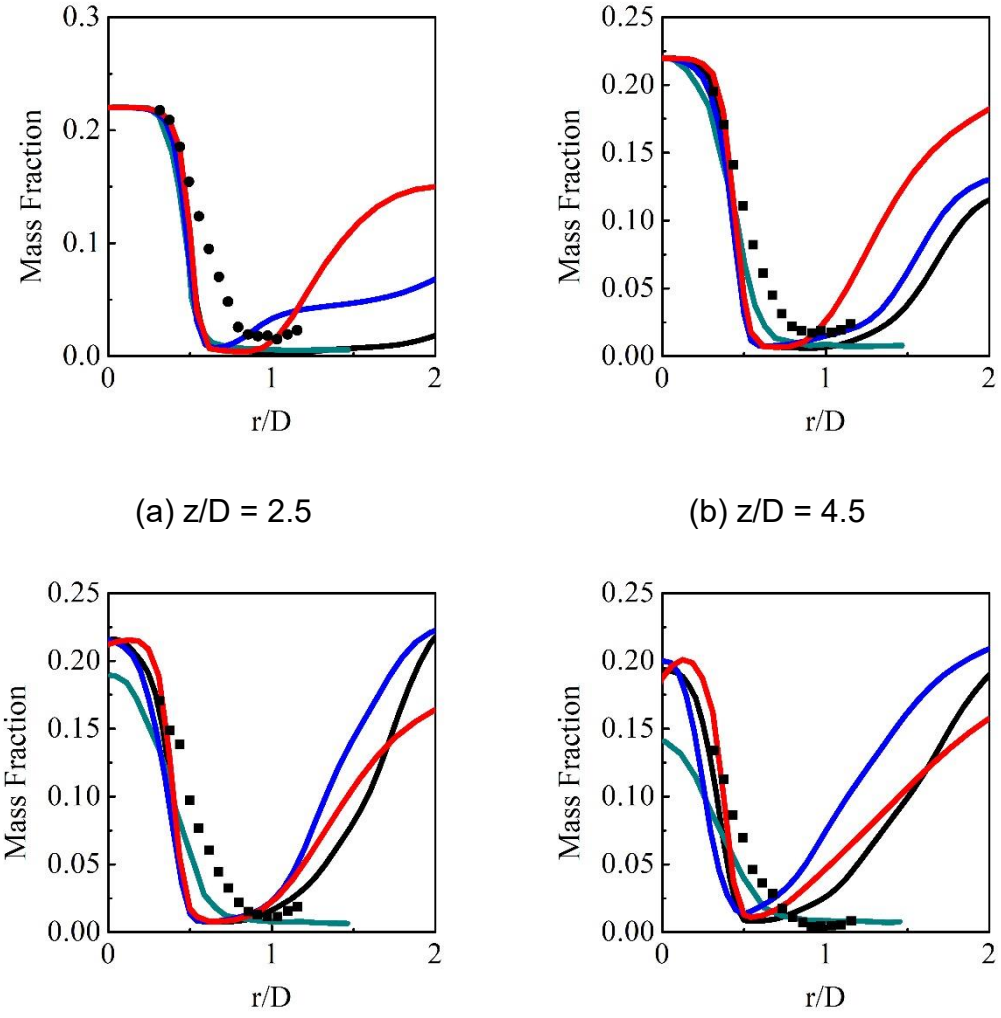

(a) z/D = 2.5

(b) z/D = 4.5

(c) z/D = 6.5

(d) z/D = 8.5

Figure 5.8 Mean profiles of O_2 mass fraction at different axial locations. The figure notation is the same as Figure 5.6.

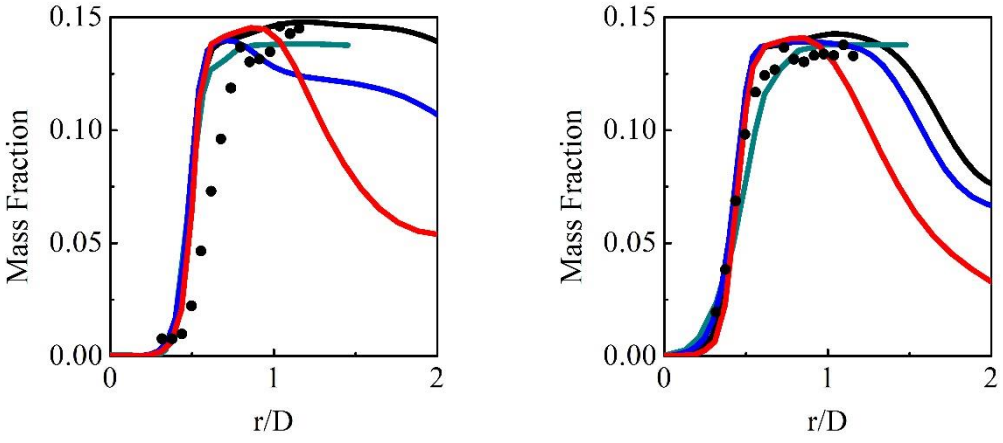

(a) z/D = 2.5

(b) z/D = 4.5

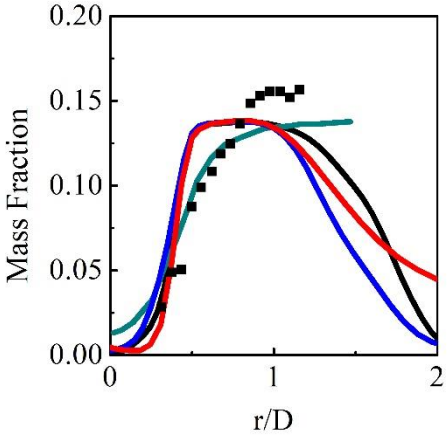

(c) z/D = 6.5

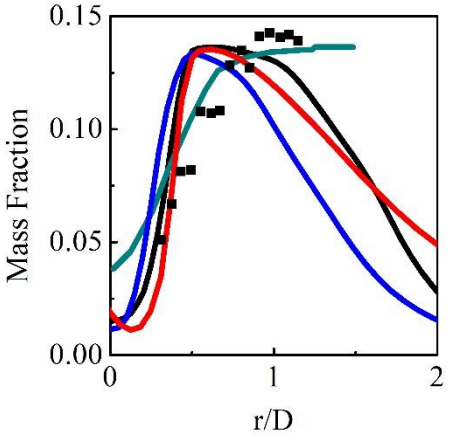

(d) z/D = 8.5

Figure 5.9 Mean profiles of CO_2 mass fraction at different axial locations. The figure notation is the same as Figure 5.6.

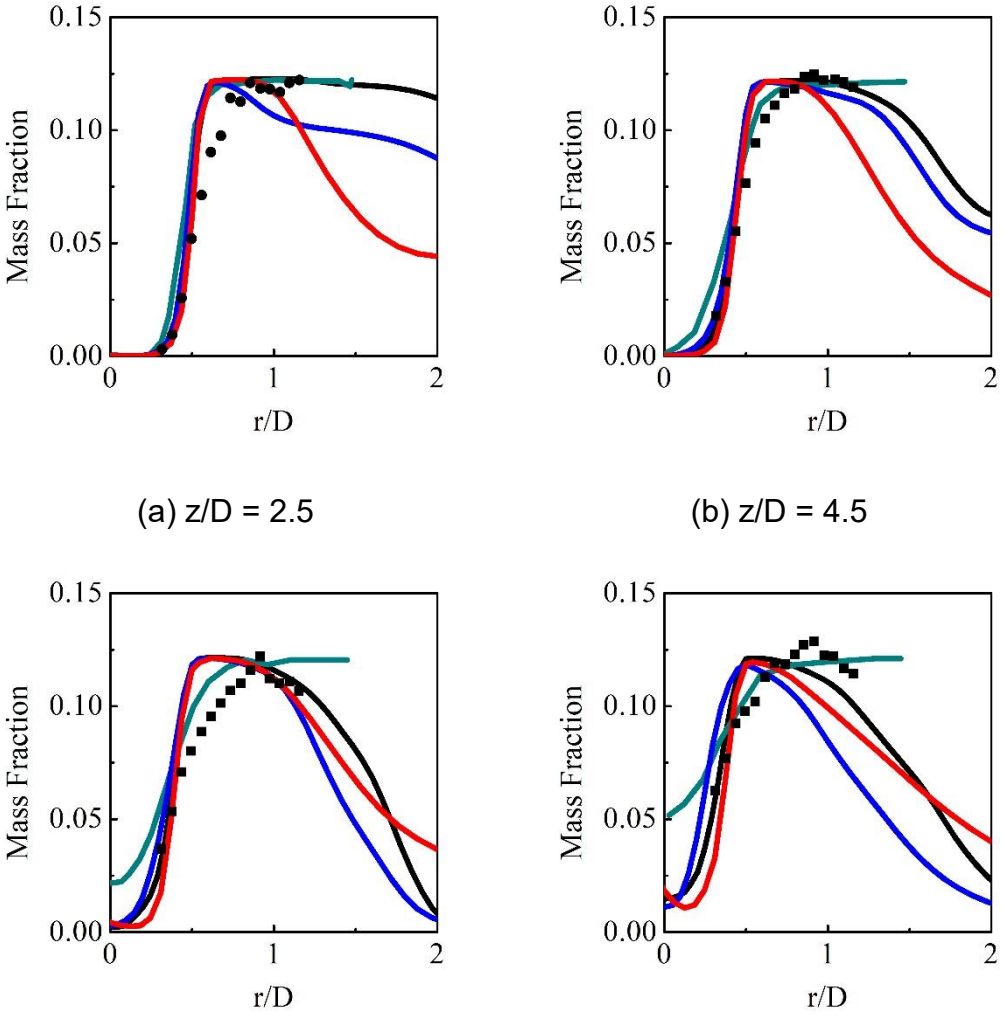

(a) z/D = 2.5

(b) z/D = 4.5

(c) z/D = 6.5

(d) z/D = 8.5

Figure 5.10 Mean profiles of H_2O mass fraction at different axial locations. The figure notation is the same as Figure 5.6.

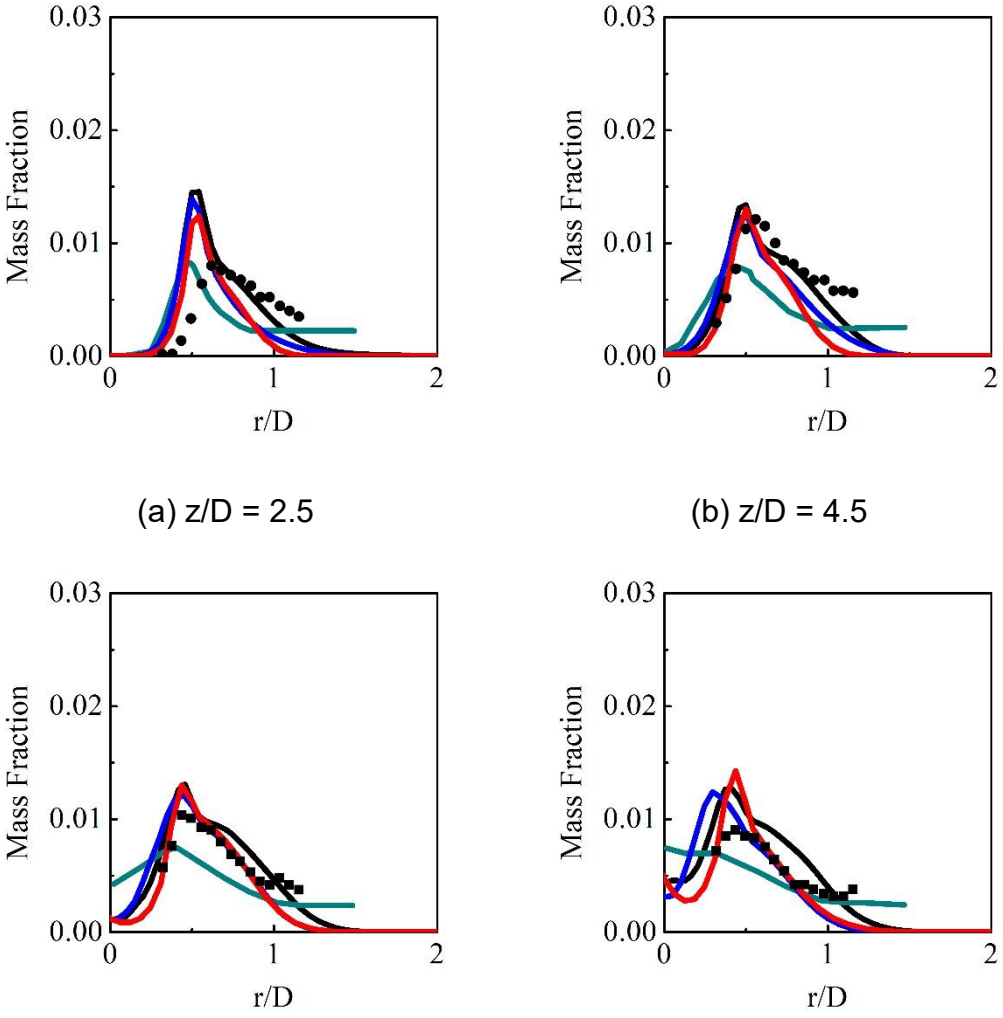

(a) z/D = 2.5

(b) z/D = 4.5

(c) z/D = 6.5

(d) z/D = 8.5

Figure 5.11 Mean profiles of CO mass fraction at different axial locations. The figure notation is the same as Figure 5.6.

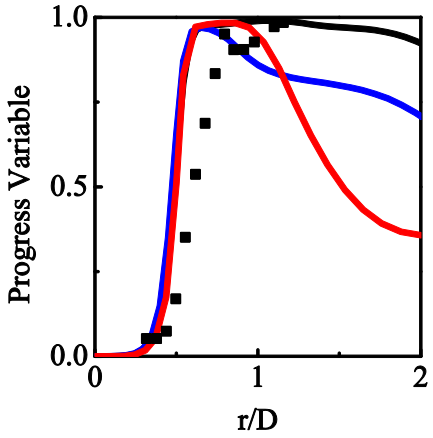

(b) z/D = 2.5

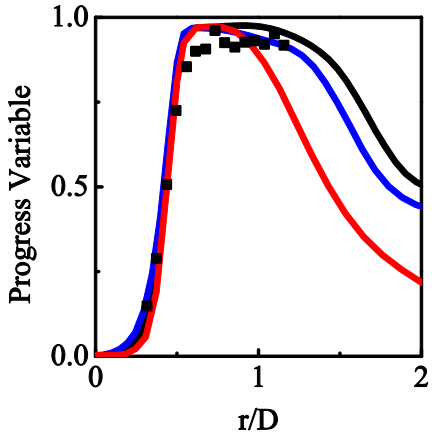

(c) z/D = 4.5

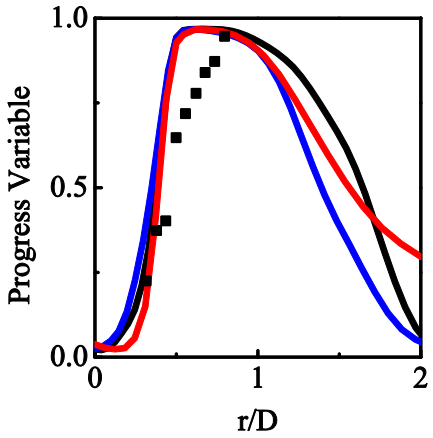

(d) z/D = 6.5

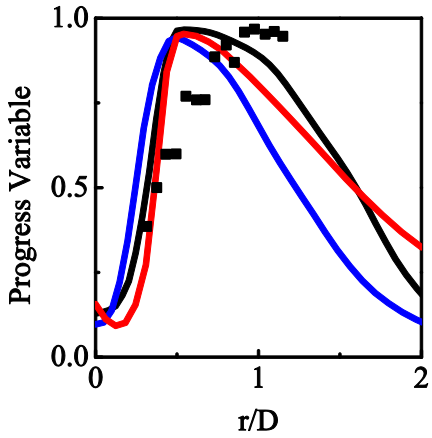

(e) z/D = 8.5

Figure 5.12 Mean profiles of progress viable c^* (species based) at different axial locations. The figure notation is the same as Figure 5.4.

5.4 Summary

A turbulent premixed Bunsen flame was simulated using LES with the series method. Two grid resolutions aligned with polar coordinates are generated, with a square section (o-grid) in the centre to avoid too dense meshes in the centreline. The chemistry is described by a well-established 4-step mechanism with 7 species.

The velocity field was overall reproduced well, with some deficiencies in the upstream area. Species profiles including the intermediate CO were in good agreement with the results. The temperature trend was predicted reasonably, but the maxima are larger than the experimental data. It is largely due to It is largely due to the under-estimation the experimental heat loss in the pilot jet. Progress viable defined by species are displayed and show a good match with the measurements.

Compared with Dormingo`s simulation, the series model behaves similarly well to the ADEF model, except the velocity field where the ESF model produce more accurate results, but the series model obtain better performance in reproducing CH_4, O_2, H_2O, CO_2 and CO.

In relation to the no SGS model, the series model accomplished a much better predicting capability. Refining the mesh resolution, the series model shows a good grid sensitivity.

Compared with the no SGS model, the series model achieved a much better predicting capability. Refining the mesh resolution, the series model shows a good grid sensitivity.

The overall findings demonstrate that series model is capable to reproduce premixed flames in high Reynolds number and provide an accurate prediction of the velocity and species fields.

6 Simulation of a premixed bluff-body stabilized flame

In this chapter, a premixed bluff-body stabilised flame is simulated with the series model in terms of the non-reacting and reacting flows. This flame is characteristic of many important features of practical combustors, for instance, flame anchoring, recirculation areas and shear layers. The emphasis in this part is on sufficiently predicting these unsteady turbulent combustion features, as well as accurately determining the statics profiles such as mean velocity, velocity fluctuation and temperature information.

6.1 Introduction

Premixed turbulent combustion is arguably the most difficult regime to model for Large eddy simulation (LES), as flame scales and flow scales can be widely different. An even more challenging case is premixed turbulent combustion involving solid walls. However, a common method in premixed combustors and laboratory burners to stabilise a turbulent flame is by means of flame holders such as a bluff body, where a recirculation zone of hot products is established to ignite the mixture flows continuously. A key to designing low-emission combustors and burners is better understanding of combustion dynamics, including ignition, vortex shedding, turbulence-kinetics interaction, and flame-

wall interactions including flame-holding. The operation of such devices is often impaired by potentially harmful combustion instabilities, which at the lean limit may cause blow off, and at the rich limit may lead to flashback (Fureby, 2000a). In combustors with bluff-body flame holders, vortex shedding from a shear layer plays a significant role in flame anchoring due to the Kelvin-Helmholtz instability. Although research in this area has been active for over five decades, a throughout fundamental understanding of the relevant phenomena is still lacking, due to the difficulties in conducting spatially and temporally resolved experiments and numerical simulations. In particular, the non-linear interactions between the vortex shedding, heat release and volumetric expansion in the wake (Zettervall et al., 2017) present special difficulties, which often lead to thermos-acoustic instabilities in unsteady flames.

The bluff-body stabilised premixed flame experiment with a rectangular cross-section and a triangular bluff-body performed under the Volvo Flygmotor AB program (Sjunnesson et al., 1991a, Sjunnesson et al., 1991b) has been simulated by many researchers for model validation and lean premixed combustion study. The most used combustion models for reproducing the bluff-body flame dynamics can be divided into three groups the same as the categorisation in the first part. The first type is *geometric approaches*, which is based on flame-front geometry/topology using the flamelet assumption describing the flame as a front much thinner than any other length scale, and employing an effective flame surface to account for flame–turbulence interaction (Giacomazzi et al., 2004). Fureby (Fureby, 2000b) presented the development and application of *a flame-wrinkling LES combustion model* in

which transport equations for a reaction coordinate, a modelled flame-wrinkling density and the laminar flame speed are derived, modelled and solved for, and Cocks (Cocks et al., 2015) also used the same progress variable type model to study the impact of numerics on the predictive capabilities of reacting flow LES. Erickson (Erickson and Soteriou, 2011) focused on the influence of reactant temperature on the dynamics of bluff body stabilised premixed flames with the *flame sheet model,* while Sankaran (Sankaran et al., 2012) employed the same model and studied the key physics of flame blow off. Park and Ko (Park and Ko, 2011) presented the application of *a dynamic G-equation model*, and temperature and velocity results match experiments well. Ghani (Ghani et al., 2015) put the dynamic thickened flame model in practice and confirms the capacity of high order LES to capture not only low-frequency oscillations but also high-order frequency transverse modes in combustion chambers. Ma (Ma et al., 2014, Ma et al., 2013) developed a new algebraic model for Favre-filtered Scalar Dissipation Rate based on the flame surface density model and validated it using this flame.

The second category is models based on turbulent mixing descriptions, constraining the effective reaction rate and describing it in terms of scalar dissipation rate (Giacomazzi et al., 2004). Giacomazzi (Giacomazzi et al., 2004) used the *fractal model* to discover the coupling of turbulence and chemistry, and the model assumes that chemical reactions take place only at the dissipative scales of turbulence near the so-called “fine structures” (eddy dissipation concept). Zettervall (Zettervall et al., 2017) compared the influence of reaction mechanism on flames with *the Partially Stirred Reactor LES model*,

using two well-known global reaction mechanisms and a novel skeletal reaction mechanism, and found that the choice of the reaction mechanism does not significantly influence the instantaneous or time-averaged velocity, whereas the instantaneous and time-averaged species and temperature are influenced.

The third class is statistical methods based on single-point probability density function (pdf) of scalar fields and geometrical flame surface analysis, describing diffusive processes through micro-mixing models that are independent of chemical reactions. Length scale effects are indirectly included, by introducing the pdf as a function of the scalar dissipation rate. Möller (Möller et al., 1996) compared *an eddy-dissipation-kinetic model, a presumed pdf approach and MILES* and revealed a sufficient level of accuracy for all first- and second-order statistical moments available. Jones (Jones et al., 2015) tested the *Eulerian stochastic field method,* and the results show very good agreement with the experimental data demonstrating the capability of the LES method coupled with the SGS-pdf method in representing premixed combustion in complex flame configurations. Gokulakrishnan (Gokulakrishnan et al., 2009) modelled the flame instability and blow-out in bluff-body stabilised flames with the *LES-PDF approach*.

6.2 Test Case Description

The case under consideration is the bluff-body stabilised premixed flame experiment performed under the Volvo Flygmotor AB program. It is relatively simple but includes many features in practical combustors, such as flame

anchoring, recirculation zones, and shear layers. It has been used for LES model validation (Baudoin et al., 2009, Jones et al., 2015, Ma et al., 2014, Wang et al., 2011, Emerson et al., 2011, Ma et al., 2013) and lean premixed combustion study (Zettervall et al., 2017, Erickson and Soteriou, 2011, Cocks et al., 2015, Fureby, 2000a, Kiel et al., 2007, Porumbel and Menon, 2006, Kim and Pope, 2014, Shanbhogue et al., 2009, Ghani et al., 2015). The configuration consists of a 1 m long straight channel with a rectangular cross-section of 0.12 $\times$ 0.24m. The flame is anchored on a bluff body, having an equilateral triangular cross-section (side length H= 0.04 m), located 0.68 m upstream of the exit. A propane and air mixture at 1 atm and 288 K (T_{in}) is introduced at an equivalence ratio of 0.65. The mixture flows at a bulk inlet velocity of U_{in} = 17 m/s, resulting in a bulk Reynolds number of 48000 and Karlowitz number of 62, with an inlet turbulence intensity of 3-4%. In the experiment, temperature was measured by CARS and velocity by LDA(Sjunnesson et al., 1991a).

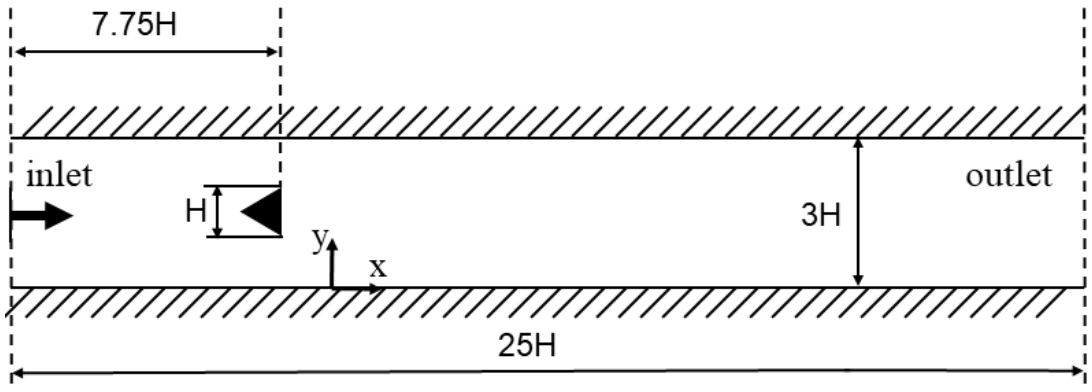

Figure 6.1 Schematic of the Volvo Rig combustor. The interior width in the z-direction is 6H.

The key quantities relevant to the configuration are described in Table 6.1. The grid size is chosen based on two criteria: the resolution of the boundary layer on the bluff body, estimated to be around 5 mm (Cocks et al., 2015), and the Pope energy criterion (Pope, 2001) which suggests that a filter-width to integral length scale ratio of Δ/H = 0.083 should be maintained to resolve 80% of the turbulent kinetic energy. The latter criterion gives a maximum filter width of 3.3 mm. Two grid resolutions of 3 and 1 mm. Respectively, are generated, where the filtered width is the cubic root of the cell volume. The grids employed are nearly isotropic ($\Delta x = \Delta y = \Delta z$) in most regions except near walls, where grids are stretched to capture near-wall motions. All simulations are performed on grids with a span-wise depth of 4H, with periodic boundary conditions. The domain accounts for the combustor section extending 2.5H upstream and 17H downstream of the flame-holder trailing edge. At the inlet, Dirichlet conditions are used for all variables except pressure, for which zero Neumann conditions are employed. At the exit, zero Neumann conditions are specified for all variables except pressure, for which wave-transmissive conditions are used. No-slip conditions are applied to walls of the duct as well as the bluff-body, while zero Neumann conditions are specified for the other variables. The time-step is variable, and the compressible Courant number is lower than 0.2 throughout the simulations. Chemistry is computed using a single-step mechanism for propane/air flames (Peters and Rogg, 2008). Previous comparisons (Zettervall et al., 2017) showed that the choice of the reaction mechanism (simplified or detailed) does not significantly influence the instantaneous or time-averaged velocity, and simplified mechanisms (Cocks et al., 2015, Giacomazzi et al.,

2004, Jones et al., 2015) have achieved good predictions in this configuration. Besides the series model, a no SGS model neglecting the SGS part in the chemical source term ($\overline{\dot{\omega}_\alpha(\varphi_1, \varphi_2, \ldots, \varphi_k)} = \dot{\omega}_\alpha(\overline{\varphi_1}, \overline{\varphi_2}, \ldots, \overline{\varphi_k})$) is employed to be a comparison test. All simulations are performed on the UK national supercomputing service Archer with 480 2.7 Ghz processors.

Table 6.1 Parameters for the combustor configuration

Parameter	Expression	Value
Bluff body side (Characteristic Length)	H	40mm
Integral Length Scale	L_I $(=H)$	40mm
Bulk Inlet Velocity (Characteristic Flow Velocity)	U_{sh}	17m/s
Macroscopic Reynolds Number	Re_{sh}	48,000
Inlet Temperature	T_s	288K
Nominal Pressure	P	101kPa
Kolmogorov Length Scale	$Re_{sh}^{-3/4}H$	12.5μm
Cold Flow Filter Width (Pope's Criterion(Wang et al., 2011))	$\triangle=0.083L_I$	3.3mm
Shear Layer Fluctuation (measured)	$u`$	10m/s
Integral Time Scale	$t_I=h_s/u`$	4ms
Kolmogorov Time Scale	$Re_{sh}^{-1/2}t_I$	18us
CFL Criterion Time Scale	$C_{max}\triangle x/(U_{sh}+U_{sound})$	2.2us

6.3 Results and Discussions

6.3.1 Non-reacting

Before reacting simulation, the reacting flows are computed, with the prominent flow features in the wake region of the bluff-body comprising of the shear layer and the shedding vortices, the recirculation zone, and the stagnation region. The grid resolution is 3mm. Statistical collection is performed over 8 burner flow-through times. Prior to that, 6 burner flow-through times are simulated to ensure the flow is established.

The contours of average axial velocity with the corresponding streamlines are shown in Figure 6.2. Clearly, the flow is characteristic of symmetric strong recirculation regions right behind the bluff body. As know from the values (where axial velocity is less than 0), the recirculating region is sustained up to 1.5*H* downstream of the bluff body. Besides, the strong velocity gradient in the wake indicates Kelvin–Helmholtz instability occurs in these free shear layers.

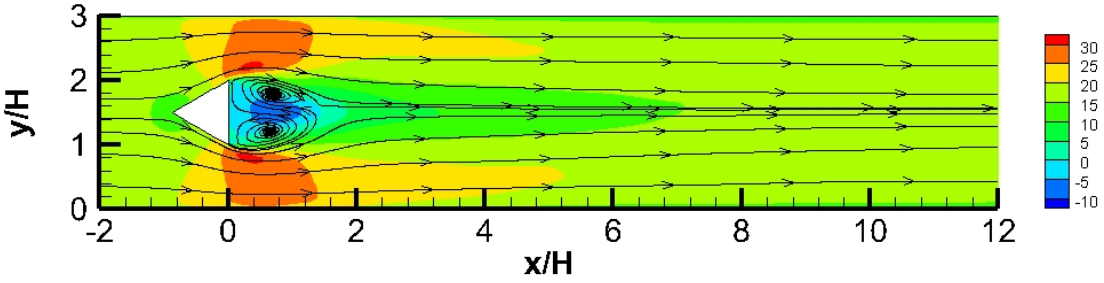

Figure 6.2 Average axial velocity profile with streamlines

Figure 6.3 depicts instantaneous iso-surfaces of vorticity magnitude at levels 1500s^{-1} and 3000s^{-1} coloured by the Z-component of vorticity. It can be seen

that coherent vortices convect downstream, owing to the rotation of vortex sheets generated right behind the bluff body. These primary vortices are shed from the shear layer due to Kelvin–Helmholtz instability as they progress, breaking themselves down into small-scale eddies. In addition, extra vortices are shed from the both walls of the duct, on account of the adverse pressure gradient near the regions of separation. The interactions between the wall and primary vortices give rise to the three-dimensional breakdown and formation of smaller turbulent structures downstream, featuring a typical von-Karmen vortex street.

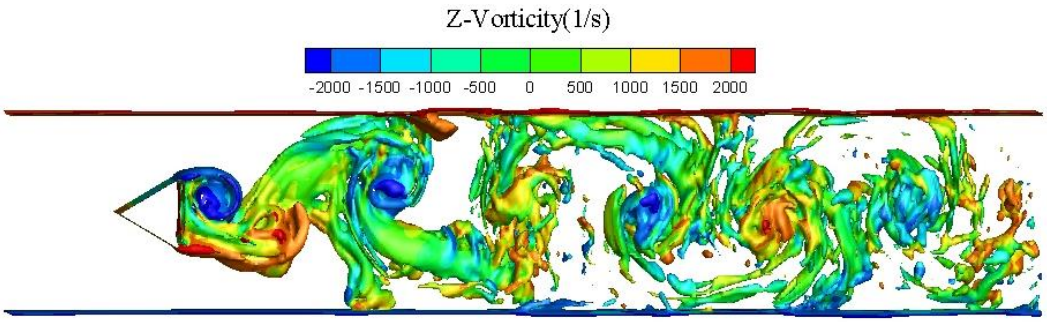

Figure 6.3 Iso-surfaces of vorticity magnitude at levels of 1500 s^{-1} and 3000 s^{-1} coloured by the z-component of vorticity

The average Z-vorticity contours are shown in Figure 6.4. It also can be seen, the flow field is dominated of strong primary recirculation zones behind the bluff body and accompanied by the secondary vortex structures near the walls (near x/H = 3). It is consistent with the observations in the instantaneous contours.

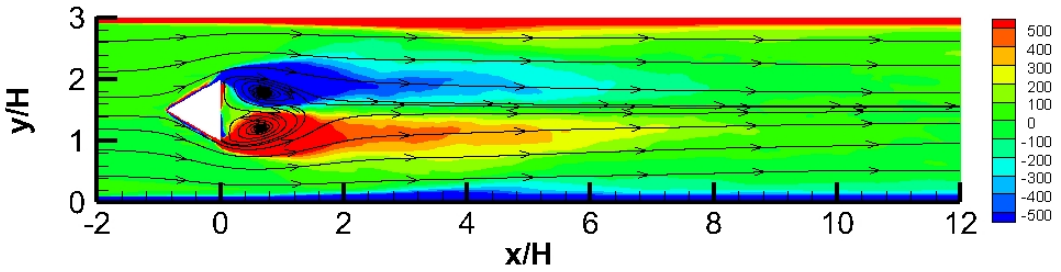

Figure 6.4 Average Z-vorticity distribution

Figures 6.5 and 6.6 present the contours of the rms axial velocity and Reynolds stress term with streamlines. Both illustrate that Strong turbulence primarily take place in the region of recirculation and its suburbs. The strong vortex shedding in the recirculation region due to Kelvin-Helmholtz instability leads significantly to the generation of turbulent kinetic energy in the shear layers.

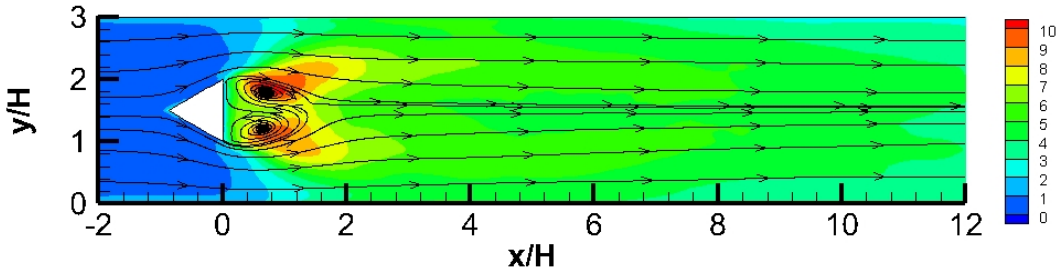

Figure 6.5 rms axial velocity distribution with streamlines of mean velocity

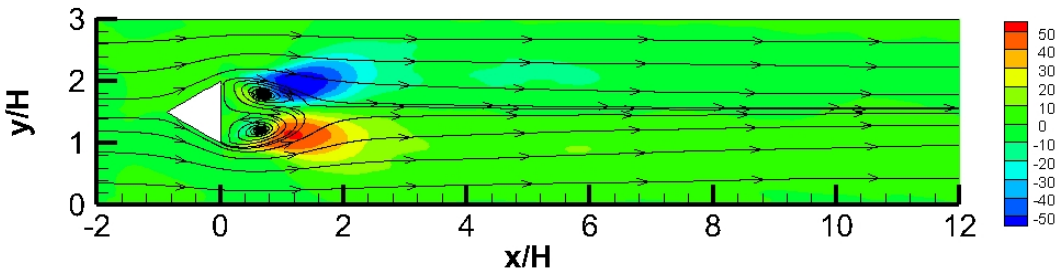

Figure 6.6 Reynolds stress term distribution with streamlines of mean velocity

Figure 6.7 depict respectively the normalized mean axial velocity, and normalized rms axial velocity profiles across the combustor duct at three axial locations. Besides, the Reynolds stress term profiles at different axial locations are presented.

On the whole, the profiles match with the experimental measurement sufficiently well. The mean profile shows that the recirculation region extends to the location (x/H=1.53), beyond where the velocity is positive everywhere in the flow field, which coincides with the observations in Figure 6.2. The rms and Reynolds stress term profile indicate that the strong fluctuations dominate in the shear layer, and decrease as the flow develops downstream.

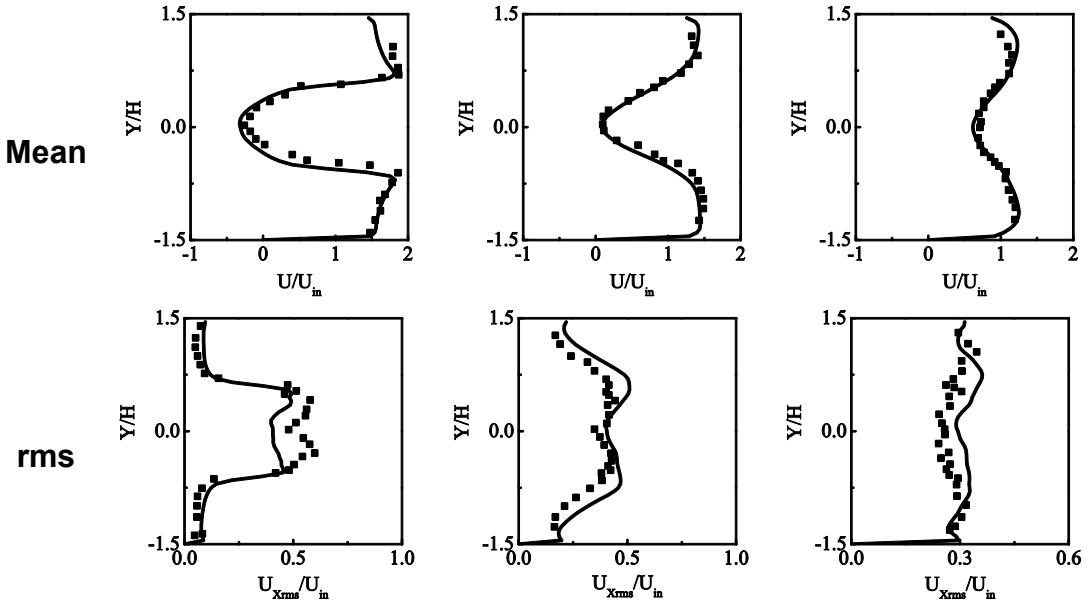

Figure 6.7 Mean and rms velocity profile distributions at different axial locations. Solid line: simulation results (i). Cube scatter: experimental data (Sjunnesson et al., 1991a, Sjunnesson et al., 1991b) (ii).

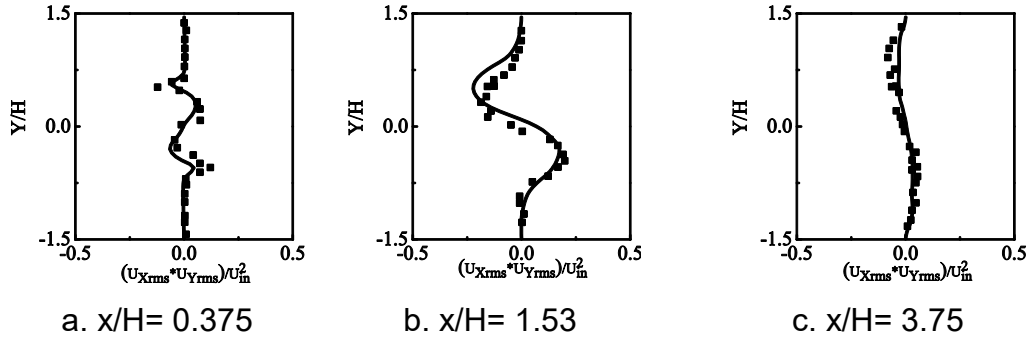

Figure 6.8 Reynolds stress term comparison at different axial locations. Solid line: simulation results (i). Cube scatter: experimental data (Sjunnesson et al., 1991a, Sjunnesson et al., 1991b) (ii).

Figure 6.9 displays the normalized average axial velocity, anisotropy and fluctuation level along the centreline. Here the anisotropy η, and the fluctuation level ζ, are defined as follows:

$$\eta = \frac{u'_{cy}}{u'_{cx}}, \qquad \zeta = \frac{\sqrt{u'^2_{cx} + u'^2_{cy}}}{u_{inlet}} \tag{6.1}$$

where u'_{cx} and u'_{cy} are the axial and transverse velocity fluctuations along the centreline respectively.

The simulation results coincide with the experiments. It can be seen that the mean velocity drops directly near the bluff body, and increase after hitting the peak reverse velocity at x/H = 0.7. The turbulence anisotropy and fluctuation level also experience a roller coaster trend: the former reaches its peak in the stagnation zone, where fluids flow reversely, and the turbulent flows turn more isotropic further downstream; the latter remain a high profile in the recirculation zone, and descend afterwards due to vortex breakdown and turbulence dissipation.

In summary, the flow field are accurately reproduced by the solver, and the 3-mm resolution grids are sufficient to predict the mean and fluctuation velocity trends as well as the key recirculation features.

a) mean velocity profile

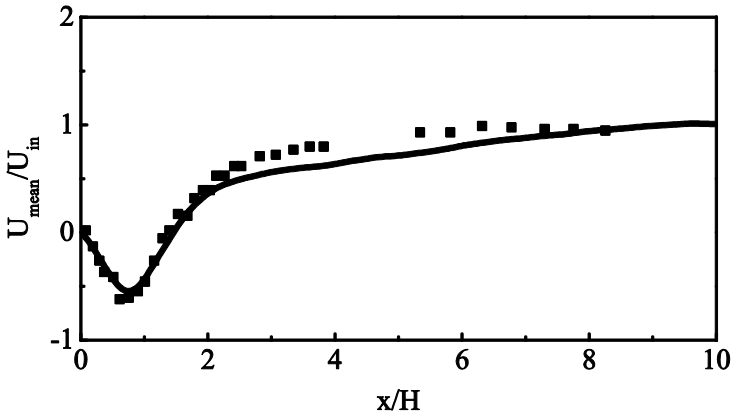

b) anisotropy

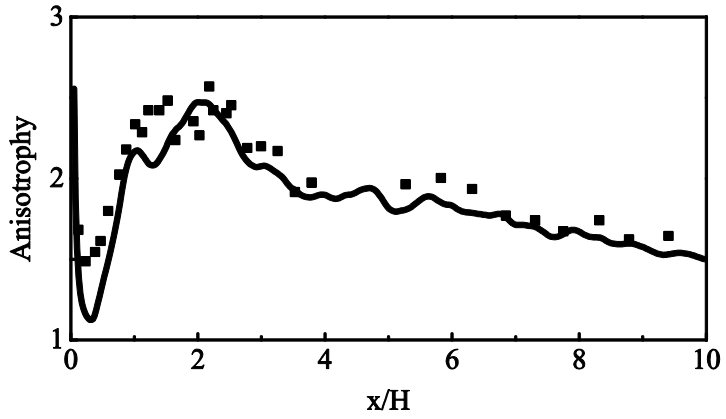

c) fluctuation level

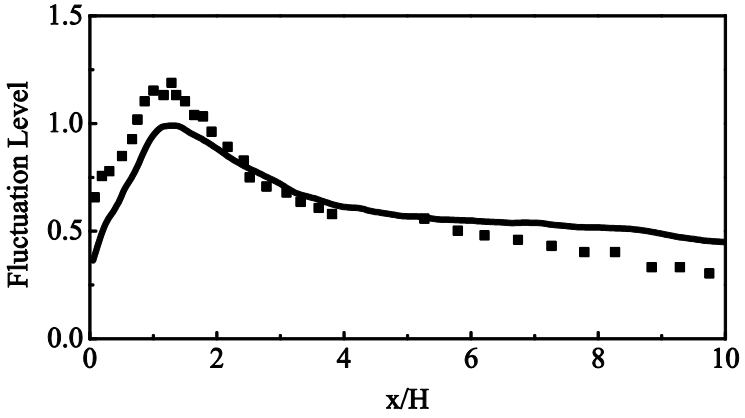

Figure 6.9 centreline profile of velocity flow field comparison. Solid line: simulation results (i). Cube scatter: experimental data (Sjunnesson et al., 1991a, Sjunnesson et al., 1991b) (ii).

6.3.2 reacting flows

Reacting flows are simulated in this part, with 2 grid resolutions 3mm and 1mm. Statistical collection is performed over 6 burner flow-through times based on the inlet bulk velocity. Prior to that, 4 burner flow-through times are simulated to ensure the flows established. All simulations are performed on the UK national supercomputing service Archer with 240 and 720 2.7 Ghz processors for 3mm and 1mm grid resolutions respectively. The total simulation time for no SGS model, series model in coarse grids, and series model in fine grids are respectively 14hrs, 22hrs, and 119hrs.

6.3.2.1 flow-field structures

In this part, the Figure 6.10 shows typical vortical structures after the bluff-body, represented by iso-surfaces of vorticity magnitude. The large-scale coherent vortices are shed from the shear layer due to Kelvin-Helmholtz instabilities, which break down into smaller scale eddies downstream. A von Karman vortex street is established in the wake of the body characterised by nearly symmetric vortex shedding. Observing the temperature distribution in Figure 6.11, hot combustion products inside the recirculation zone incessantly mix with the cold co-flowing mixture, and sequentially ignition occurs in the shear/mixing layers. The ignited flame convects downstream and continues to ignite the neighbouring mixtures by heat transfer. The recirculation region behind the flame-holder, sustaining this continuous re-ignition process,

stabilises the flame. The series model correctly reproduces the flame-anchoring features.

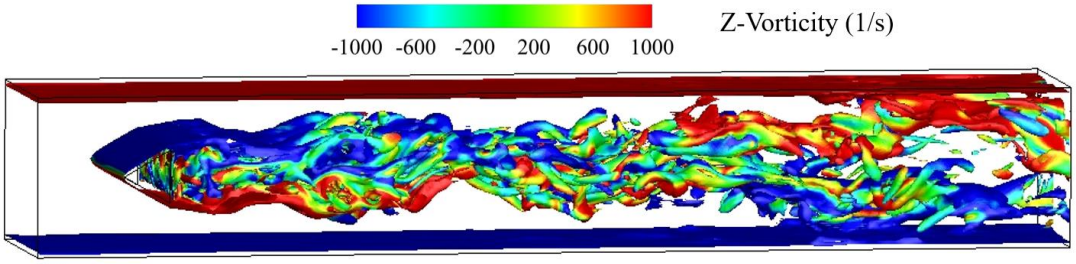

Figure 6.10 Iso-surface of vorticity magnitude level 2000 s^{-1} vorticity colored by the z component of vorticity.

Figure 6.11 depicts the contours of temperature, the reaction rate of C_3H_8 and its SGS part. Identical to vortex shedding in Figure 6.10, flame propagation is presented almost symmetrically at least before *x/H*=6. This behaviour was also reported in previous LES (Cocks et al., 2015, Zettervall et al., 2017, Möller et al., 1996). Chemical reaction takes place in the shear layer between the wake and unburnt mixtures. This reacting zone is identified by the reaction rate of C3H8 here. The SGS contribution to the source term determined by the series model oscillates between -6% and 18 % roughly, and it appears in the reaction zone accordingly, where scalar gradients are large and SGS fluctuations are expected to play a major role. Large SGS contributions first appear between *x/H* = 3.7 in Figure 6.11 (c) in the shear layer, probably due to vortex shedding that enhances the turbulence intensity. Further downstream at *x/H* = 12, strong

SGS levels show up again, where small-scale eddies roll up and merge (see Figure 6.10), indicating important sub-grid turbulence-chemistry interactions.

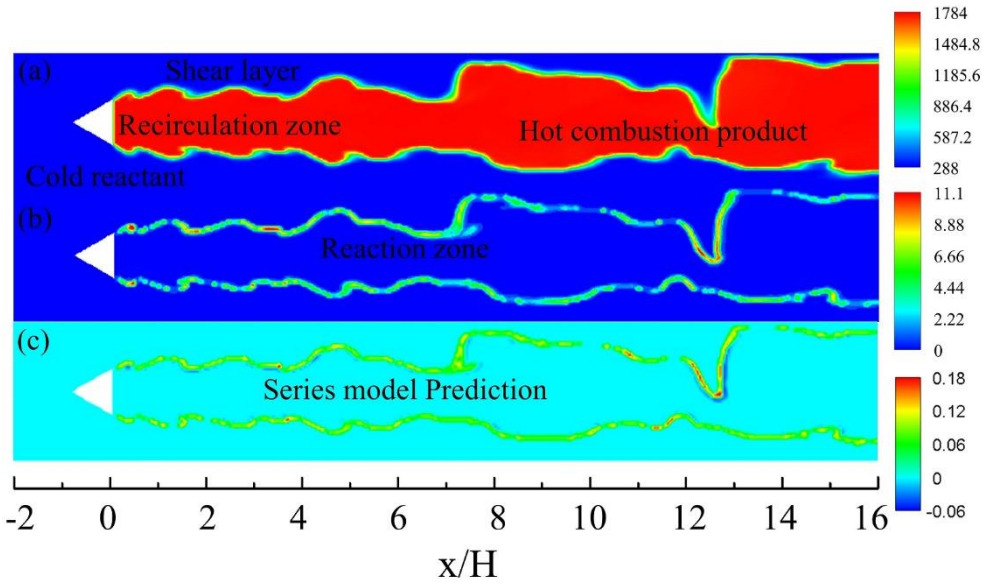

Figure 6.11 Instantaneous contours. a) temperature, b) absolute value of the C_3H_8 reaction rate $|\dot{\omega}(\tilde{c})|$ and c) SGS contribution ratio of C_3H_8 reaction rate, $\dot{\omega}_{SGS}/\dot{\omega}(\tilde{c})$.

Figure 6.12 depicts average Z-vorticity with the corresponding streamlines. A couple of primary vortices in counter rotation prevail right in the recirculation zone behind the flame holder, which account for stabilising flames. Similar to Figure 6.10, no vortex shedding happens near the duct walls. Opposite to the non-reacting, another pair of significant vortices is observed further downstream, caused by the generation of baroclinic vorticity by the flame(Cocks et al., 2015). The direction of rotation is on the contrary to the responding primary vortices. They act a role in suppression of vortex shedding.

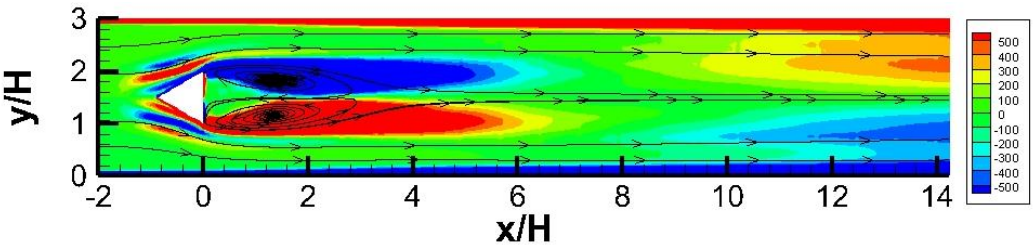

Figure 6.12 Average Z-vorticity

6.3.2.2 Statistical flow-field results

Distributions of mean and RMS axial velocities between the no model approach and series model at 2 different grid resolutions are presented in Figure 6.13. The iso-contour lines are outlined in the mean profile, while the streamlines of mean velocity are plotted in RMS. All results show that the mean flow is dominated by a recirculation zone (indicated by negative axial velocity) behind the flame-holder and strong shear layers originating from the bluff-body corners. The series model predicts a larger recirculation region (from x/H = 3.4, until 3.1) for the fine and coarse meshes, respectively. The recirculation region extends to x/H= 2.7 in the no-model approach. In conjunction with the centreline profile in Figure 6.14, the experimental recirculation length is 3.5H, showing that the series model predicts a recirculation length very close to experimental measurements. Accurate predictions of this region are a key to simulating bluff-body-like combustors as it plays a vital role in anchoring flames and periodically mixing reactants and products. As to RMS profiles, the series model predicts a lower fluctuation level when the grid is refined. The difference between models is obvious in the coarse-grid resolution.

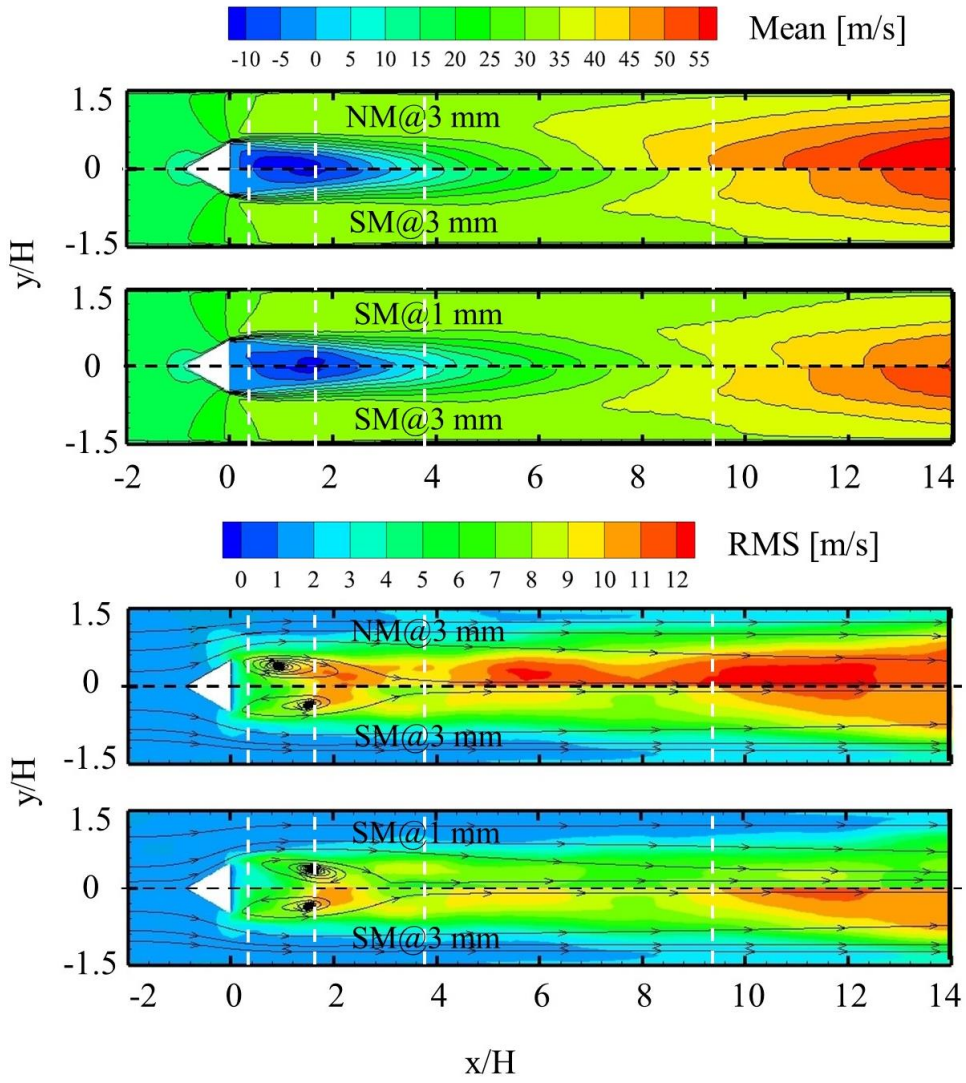

Figure 6.13 Mean (top) and RMS (bottom) axial velocity contours at different grid resolutions. NM is short for no model approach and SM for series model. 1 mm and 3 mm stand for the grid resolutions. These abbreviations are also in effect in the following figures.

The centreline velocity profile is depicted in Figure 6.14. Comparisons of simulated and experimentally measured time-averaged axial velocity profiles along four axial sections (*x/H* =0.375, 1.63, and 3.75 in the recirculation zone, *x/H* = 9.4 in the downstream, these locations are outlined by while dash lines in

Figure 6.13.) through the burner are shown in Figure 6.15. Overall, a reasonably good agreement with experimental data is achieved by the new series model, even at the coarsest resolutions. The model correctly reproduces the velocity transition from U-shape near the bluff body to the V-shape at the end of recirculation zone and the flat profile in the downstream wake. Overall, both models slightly over-estimate the mean velocity downstream. However, the series model gives the closest agreement with experimental data. It could be related to the more intense volumetric thermal expansion (Ma et al., 2014) simulated in these locations. Besides, the overall trends in the RMS velocity are well captured, with two separate peaks located at the shear layers in the recirculation zone. However, the no-model predicts over 3 times as large RMS fluctuations as experimental measurements downstream; the series model result gives less adequate RMS fluctuation peaks at x/H=1.63. The small discrepancies could be attributed to the simplicity of the chemical mechanism in use. Nevertheless, the series model also over-predicts experimental fluctuations downstream but provides good agreement within the recirculation region. It also demonstrates good predictive abilities of the simplified chemistry incorporated into the series model.

In Figure 6.16, the predicted mean temperatures are compared with experimental data. Despite the series model producing the best agreement with experimental data, the peak temperature is slightly over-predicted, which might account for the acceleration prediction downstream.

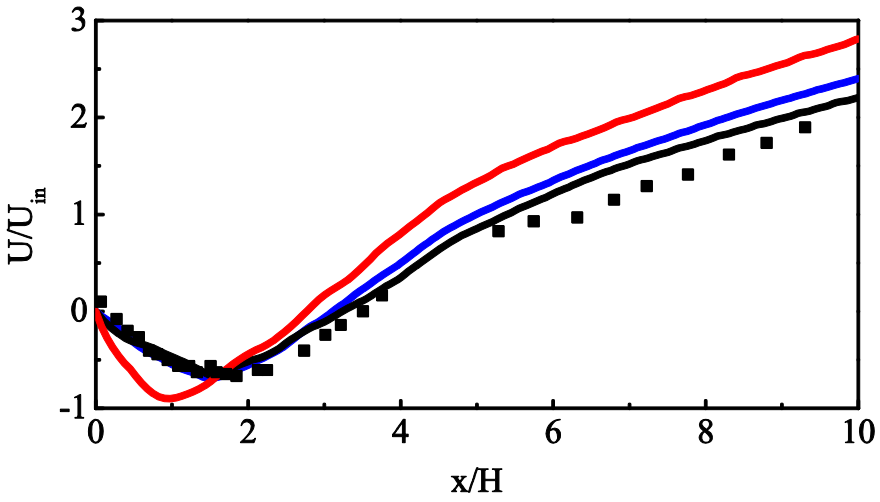

Figure 6.14 Centerline mean axial profile for different models in different grid resolutions. Black solid line: SM@1mm (i). Blue solid line: SM@3mm (ii). Red solid line: NM@3mm (iii). Cube scatter: experimental data (Sjunnesson et al., 1991a, Sjunnesson et al., 1991b) (iv).

Comparing the series model in different grid resolutions, the 1 and 3 mm results are closer, especially for the mean and RMS profile at *x/H* = 3.. As expected, despite neglecting sub-grid fluctuations, the no-model results remain worse than those of the series model. If the grid is further refined, $\Delta \to 0$ *and* $\dot{\omega}_{SGS} \to 0$, and all models are expected to converge to a DNS solution. Due to the scarcity of the relevant experiment measurements, the species information is not compared in this work.

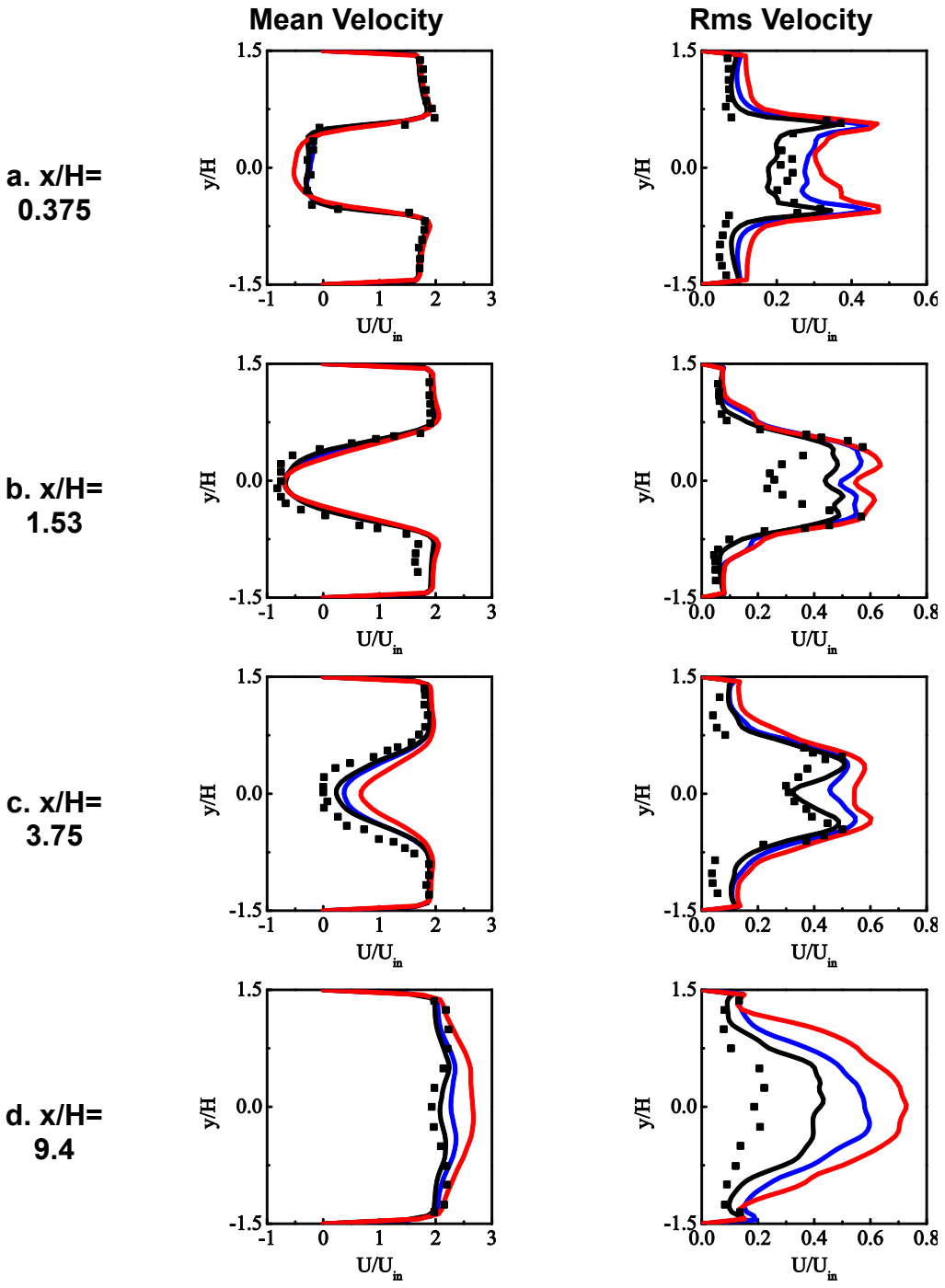

Figure 6.15 Mean (left) and RMS (right) axial velocity profiles for different models in different grid resolutions. Black solid line: SM@1mm (i). Blue solid line: SM@3mm (ii). Red solid line: NM@3mm (iii). Cube scatter: experimental data (Sjunnesson et al., 1991a, Sjunnesson et al., 1991b) (iv).

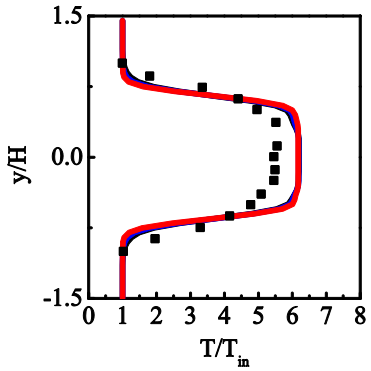

a. *x/H*= 0.375

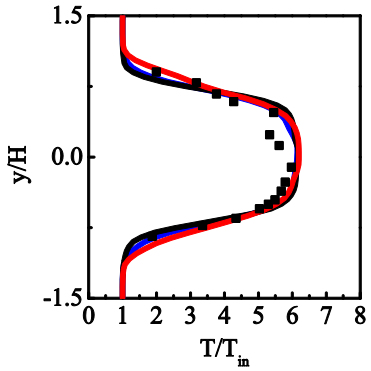

b. *x/H*= 1.53

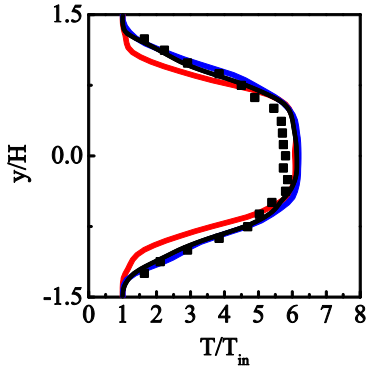

c. *x/H*= 3.75

Figure 6.16 Predicted mean temperature profiles compared with experimental data. Black solid line: SM@1mm (i). Blue solid line: SM@3mm (ii). Red solid line: NM@3mm (iii). Cube scatter: experimental data (Sjunnesson et al., 1991a, Sjunnesson et al., 1991b) (iv).

6.4 Summary

A bluff-body stabilised premixed flame was simulated using LES with the series method in terms of non-reacting and reacting flows. Two grid resolutions are employed with no SGS model as a comparison test. The chemistry is described by a well-established single-step mechanism.

The results show that the series model reproduces correctly key characteristics such as flame anchoring, recirculation zones and shear layers. Statistically, good agreement with experimental data is obtained by the series model, in terms of time-averaged profiles of velocity and its fluctuations, and temperature as well as the size of the recirculation region. Compared with the no SGS model, the series model achieved a much better predicting capability. Refining the mesh resolution, the series model shows a good grid sensitivity.

The overall findings reveal that series model is capable to reproduce the key features of flame anchoring, recirculation zones and shear layers in a combustor-like premixed flame and deliver an accurate prediction of the velocity and temperature fields.

7 Conclusions and Future Work

7.1 Summary

The research scheme in this work aims to derive and develop an innovative series combustion sub-grid model into a robust and reliable modelling technique in the context of LES for turbulent flames.

In the first stage, the mathematical derivation procedures of the series model are addressed. The principle notion is based on Taylor series expansion of the unclosed chemical source term around the filtered value. An important step within is to transform the differentials in the scalar field, which is hardly to be determined, to those in the predictable physical space. In theory, the model is independent of combustion regimes (premixed and non-premixed) and free from extra parameters. Besides, the model has the right properties of limiting behaviour when the filter size approaches Kolmogorov scales.

Numerically, the model is implemented into OpenFOAM, an open-source C++ toolbox for customised CFD numerical solvers. The solution provided by the series approach is coupled with LES governing equations to close the filtered scalar transport equation. The potential error sources of the model are identified, that is, the influence of higher order terms, the scalar gradient term,

the numerical scheme, and the chemical mechanisms. Besides, the control measures to reduce them are also outlined.

The second stage of this work is to address the predicting capability of the series model across different combustion regimes. Around this objective, three classes of well-established experimental flames have been chosen as simulating benchmarks. The first test case is Sandia flame series (Flame D and F) characteristic of non-premixed combustion regimes. Two grid resolutions are employed and no SGS model is used as a comparison. The chemistry is described by a well-established 4-step mechanism with 7 species. The results of the series model present generally good agreement with the experimental data of Flame D and F. The velocity field is captured very well. The mean and rms profiles of the mixture fraction, temperature and mass fractions of CH_4, O_2, CO_2, and H_2O are reasonably accurately reproduced. The discrepancies that arise in the intermediates H_2 and CO as well as the reactants CH4 and O2 could probably be attributed to limitations in the simplified reaction mechanism used in the simulation. Compared with Mustata`s simulation, the series model behaves similarly well to the ESF model in Flame D prediction, except the velocity field where the ESF model produce more accurate results, but the series model obtains better performance in mixture fraction reproducing. Combining the Jones` results, both the series model and ESF model reproduce reasonably good trends of temperature and species fields in Flame F. The main discrepancy of both models comes from the over-prediction of the maximum temperature and species fields, though ESF model behaves better in this regard. This can be improved potentially by increasing the grid resolution and

adopting more detailed chemistry mechanisms. In relation to the no SGS model, the series model accomplished a much better predicting capability.

The second investigated case consists of a turbulent Bunsen piloted flame featured by the turbulent premixed regime. Two grid resolutions are engaged and no SGS model is practised as a comparison. The chemistry is defined by a well-established 4-step mechanism with 7 species. The velocity field is overall reproduced well by the series model, with some deficiencies in the upstream area. Species profiles including the intermediate CO are in good agreement with the experimental data. The temperature trend is predicted reasonably, but the maxima are larger than the experimental data. It is largely due to the under-estimation the experimental heat loss in the pilot jet. Progress viable defined by species show a good match with the measurements. Compared with Dormingo`s simulation, the series model behaves similarly well to the ADEF model, except the velocity field where the ESF model produce more accurate results, but the series model obtains better performance in reproducing CH_4, O_2, H_2O, CO_2 and CO.

The last simulated case is a bluff-body stabilised premixed flame, involving many features of practical combustors such as flame anchoring, recirculation areas and shear layers. Two grid resolutions are engaged, and no SGS model is practised as a comparison. The chemistry is defined by a well-established single-step mechanism. The results show that the series model reproduces correctly key characteristics such as flame anchoring, recirculation zones and shear layers. Statistically, good agreement with experimental data is obtained

by the series model, in terms of time-averaged profiles of velocity and its fluctuations, and temperature as well as the size of the recirculation region. Compared with the no SGS model, the series model achieved a much better predicting capability. Refining the mesh resolution, the series model shows a good grid sensitivity.

In summary, the novel series model has been established and demonstrated to be a very promising LES technique to capture turbulent premixed and non-premixed flames and the combustion dynamics. The model has the correct limiting behaviour: the sub-grid contribution reduces with the square of the filter size, approaching DNS as approaches Kolmogorov scales. It is also free from other parameters than those in the flow field. The accuracy level of the method is determined by the Taylor series order. Due to these significant features, the model can be easily incorporated into other established LES programming framework.

7.2 Future Work

In the future work, the following aspects can be considered.

a, Application to a practical combustor.

In this work, three well-established experimental benchmarks were simulated with the series model. However, they cannot represent all the combustion dynamics encountered in industrial engines or combustors. These devices are of complex geometry and difficult for most present models to simulate. In future,

application to a practical combustor is expected to be performed to fully address the capability of the series model in dealing with complex geometry.

b, Employment of the detailed mechanism.

The detailed mechanisms generally provide a more accurate and precise prediction of reaction rate and other transient flame phenomena. Employment of detailed chemistry is anticipated to broaden the utilisation of the series model.

c, a more adaptive approximation for the scalar gradient term

In poorly resolved flames, the scalar gradient term can be inaccurate. More adaptive approximation like sub-grid mixing model or scalar dissipation like approximation are a potential measure to improve the prediction in very coarse grid resolutions.

d, application to other source terms like atmosphere modelling

The series model is a mathematical approach. In this work, the derivation is applied to the chemical source term. However, it should not be limited to combustion area. In theory, it can be extended to other scalar transport equation containing source terms in the context of large eddy simulation.

e, explore the potential for supersonic combustion and the effects of radiation and soot.

As outlined in Chapter 3.5, the examination scope is limited to low number flows neglecting soot and radiation effect within this work. The future exploration can

have an eye on supersonic flows and expand the applicability of sooting and radiative combustion.

Appendix

A. Publications during PhD studies

Peer-reviewed journal articles

[1] **Zeng W.**, Vogiatzaki K., Navarro-Martinez S., and Luo K. H. Modelling of Sub-grid Scale Reaction Rate Based on a Novel Series Model: Application to a Premixed Bluff-Body Stabilised Flame. *Combustion Science and Technology*.

[2] **Zeng W.**, Vogiatzaki K., Navarro-Martinez S., Wang X and Luo K. H. (Under review). Modelling of Sub-grid Scale Reaction Rate Based on a Novel Series Model: Application to Turbulent, Piloted Non-premixed and Partially Premixed Flames. *Fuel*.

.[3] Feng, M., Jiang, X. Z., **Zeng, W.**, Luo, K. H., & Hellier, P. (2019). Ethanol oxidation with high water content: A reactive molecular dynamics simulation study. *Fuel*, 235, 515-521.

[4] Jiang, X. Z., Feng, M., **Zeng, W.**, & Luo, K. H. (2018). Study of mechanisms for electric field effects on ethanol oxidation via reactive force field molecular dynamics. *Proceedings of the Combustion Institute.*

Conference presentations

[1] **Zeng W.**, Vogiatzaki K., Navarro-Martinez S., and Luo K. H. (2017). A Series Combustion Model for LES. The UK Consortium on Turbulent Reacting Flows, Southampton, United Kingdom.

[2] **Zeng W.**, Vogiatzaki K., Navarro-Martinez S., and Luo K. H. (2017). Assessment of Subgrid-Scale Model Effects on Large Eddy Simulation of a Back-Step Combustor. The 8th European Combustion Meeting of the Combustion Institute, Dubrovnik, Croatia.

[3] **Zeng W.**, Vogiatzaki K., Navarro-Martinez S., and Luo K. H. (2016). Large Eddy Simulation of a bluff-body stabilized premixed flame. The UK Consortium on Turbulent Reacting Flows, Durham, United Kingdom.

References

BARLOW, R. & FRANK, J. Effects of turbulence on species mass fractions in methane/air jet flames. Symposium (International) on Combustion, 1998. Elsevier, 1087-1095.

BAUDOIN, E., YU, R., NOGENMYR, K.-J., BAI, X.-S. & FUREBY, C. Comparison of LES models applied to a bluff body stabilized flame. 47th AIAA Aerospace Sciences Meeting, 2009. AIAA.

BAURLE, R. & GIRIMAJI, S. 2003. Assumed PDF turbulence-chemistry closure with temperature-composition correlations. *Combustion and Flame,* 134**,** 131-148.

BOGER, M., VEYNANTE, D., BOUGHANEM, H. & TROUVÉ, A. Direct numerical simulation analysis of flame surface density concept for large eddy simulation of turbulent premixed combustion. Symposium (International) on Combustion, 1998. Elsevier, 917-925.

BOUDIER, G., GICQUEL, L. & POINSOT, T. 2008. Effects of mesh resolution on large eddy simulation of reacting flows in complex geometry combustors. *Combustion and Flame,* 155**,** 196-214.

BOUDIER, G., GICQUEL, L., POINSOT, T., BISSIERES, D. & BÉRAT, C. 2007. Comparison of LES, RANS and experiments in an aeronautical gas

turbine combustion chamber. *Proceedings of the Combustion Institute,* 31**,** 3075-3082.

BULAT, G., JONES, W. & MARQUIS, A. 2014. NO and CO formation in an industrial gas-turbine combustion chamber using LES with the Eulerian sub-grid PDF method. *Combustion and Flame,* 161**,** 1804-1825.

BUTLER, T. & O'ROURKE, P. A numerical method for two dimensional unsteady reacting flows. Symposium (International) on Combustion, 1977. Elsevier, 1503-1515.

CHAPUIS, M., FEDINA, E., FUREBY, C., HANNEMANN, K., KARL, S. & SCHRAMM, J. M. 2013. A computational study of the HyShot II combustor performance. *Proceedings of the Combustion Institute,* 34**,** 2101-2109.

CHEN, Y.-C., PETERS, N., SCHNEEMANN, G., WRUCK, N., RENZ, U. & MANSOUR, M. S. 1996. The detailed flame structure of highly stretched turbulent premixed methane-air flames. *Combustion and flame,* 107**,** 223-IN2.

CHISHTY, M. A., BOLLA, M., HAWKES, E. R., PEI, Y. & KOOK, S. 2018. Soot formation modelling for n-dodecane sprays using the transported PDF model. *Combustion and Flame,* 192**,** 101-119.

CHOW, F. K., STREET, R. L., XUE, M. & FERZIGER, J. H. 2005. Explicit filtering and reconstruction turbulence modeling for large-eddy

simulation of neutral boundary layer flow. *Journal of the Atmospheric Sciences,* 62**,** 2058-2077.

CLEARY, M., KLIMENKO, A., JANICKA, J. & PFITZNER, M. 2009. A sparse-Lagrangian multiple mapping conditioning model for turbulent diffusion flames. *Proceedings of the Combustion Institute,* 32**,** 1499-1507.

COCKS, P. A., SOTERIOU, M. C. & SANKARAN, V. 2015. Impact of numerics on the predictive capabilities of reacting flow LES. *Combustion and Flame,* 162**,** 3394-3411.

COLIN, O., DUCROS, F., VEYNANTE, D. & POINSOT, T. 2000. A thickened flame model for large eddy simulations of turbulent premixed combustion. *Physics of Fluids,* 12**,** 1843-1863.

CORITON, B., ZENDEHDEL, M., UKAI, S., KRONENBURG, A., STEIN, O. T., IM, S.-K., GAMBA, M. & FRANK, J. H. 2015. Imaging measurements and LES-CMC modeling of a partially-premixed turbulent dimethyl ether/air jet flame. *Proceedings of the Combustion Institute,* 35**,** 1251-1258.

DE, A. & ACHARYA, S. 2009a. Large eddy simulation of a premixed Bunsen flame using a modified thickened-flame model at two Reynolds number. *Combustion Science and Technology,* 181**,** 1231-1272.

DE, A. & ACHARYA, S. 2009b. Large eddy simulation of premixed combustion with a thickened-flame approach. *Journal of Engineering for Gas Turbines and Power,* 131**,** 061501.

DE LAGENESTE, L. D. & PITSCH, H. 2000. A level-set approach to large eddy simulation of premixed turbulent combustion. *CTR Annual Research Briefs*.

DODOULAS, I. & NAVARRO-MARTINEZ, S. 2013. Large eddy simulation of premixed turbulent flames using the probability density function approach. *Flow, turbulence and combustion,* 90**,** 645-678.

DOMINGO, P. & VERVISCH, L. 2015. Large Eddy Simulation of premixed turbulent combustion using approximate deconvolution and explicit flame filtering. *Proceedings of the Combustion Institute,* 35**,** 1349-1357.

DOMINGO, P. & VERVISCH, L. 2017. DNS and approximate deconvolution as a tool to analyse one-dimensional filtered flame sub-grid scale modelling. *Combustion and Flame,* 177**,** 109-122.

DONINI, A., BASTIAANS, R., VAN OIJEN, J., DAY, M. & DE GOEY, L. 2015. An a priori DNS subgrid analysis of the presumed β-PDF model. *International Journal of Hydrogen Energy,* 40**,** 12811-12823.

ELBAHLOUL, S. & RIGOPOULOS, S. 2015. Rate-Controlled Constrained Equilibrium (RCCE) simulations of turbulent partially premixed flames

(Sandia D/E/F) and comparison with detailed chemistry. *Combustion and Flame,* 162**,** 2256-2271.

EMERSON, B., LUNDRIGAN, J., O'CONNOR, J., NOBLE, D. & LIEUWEN, T. Dependence of the bluff body wake structure on flame temperature ratio. 49th AIAA Aerospace Sciences Meeting including the New Horizons Forum and Aerospace Exposition, 2011. 597.

ERICKSON, R. & SOTERIOU, M. 2011. The influence of reactant temperature on the dynamics of bluff body stabilized premixed flames. *Combustion and Flame,* 158**,** 2441-2457.

ESCLAPEZ, L., RIBER, E. & CUENOT, B. 2015. Ignition probability of a partially premixed burner using LES. *Proceedings of the Combustion Institute,* 35**,** 3133-3141.

FAVRE, A. 1969. Statistical equations of turbulent gases. *Problems of hydrodynamics and continuum mechanics***,** 231-266.

FUREBY, C. 2000a. A computational study of combustion instabilities due to vortex shedding. *Proceedings of the Combustion Institute,* 28**,** 783-791.

FUREBY, C. 2000b. Large eddy simulation of combustion instabilities in a jet engine afterburner model. *Combustion science and technology,* 161**,** 213-243.

FUREBY, C., FEDINA, E. & TEGNÉR, J. 2014. A computational study of supersonic combustion behind a wedge-shaped flameholder. *Shock waves,* 24**,** 41-50.

FUREBY, C., NORDIN-BATES, K., PETTERSON, K., BRESSON, A. & SABELNIKOV, V. 2015. A computational study of supersonic combustion in strut injector and hypermixer flow fields. *Proceedings of the Combustion Institute,* 35**,** 2127-2135.

GALLOT-LAVALLÉE, S., JONES, W. & MARQUIS, A. 2017. Large Eddy Simulation of an ethanol spray flame under MILD combustion with the stochastic fields method. *Proceedings of the Combustion Institute,* 36**,** 2577-2584.

GARMORY, A. & MASTORAKOS, E. 2011. Capturing localised extinction in Sandia Flame F with LES–CMC. *Proceedings of the Combustion Institute,* 33**,** 1673-1680.

GE, Y., CLEARY, M. & KLIMENKO, A. 2011. Sparse-Lagrangian FDF simulations of Sandia Flame E with density coupling. *Proceedings of the Combustion Institute,* 33**,** 1401-1409.

GE, Y., CLEARY, M. & KLIMENKO, A. 2013. A comparative study of Sandia flame series (D–F) using sparse-Lagrangian MMC modelling. *Proceedings of the Combustion Institute,* 34**,** 1325-1332.

GEORGIADIS, N. J., RIZZETTA, D. P. & FUREBY, C. 2010. Large-eddy simulation: current capabilities, recommended practices, and future research. *AIAA journal,* 48**,** 1772-1784.

GHANI, A., POINSOT, T., GICQUEL, L. & STAFFELBACH, G. 2015. LES of longitudinal and transverse self-excited combustion instabilities in a bluff-body stabilized turbulent premixed flame. *Combustion and Flame,* 162**,** 4075-4083.

GIACOMAZZI, E., BATTAGLIA, V. & BRUNO, C. 2004. The coupling of turbulence and chemistry in a premixed bluff-body flame as studied by LES. *Combustion and Flame,* 138**,** 320-335.

GICQUEL, L. Y., STAFFELBACH, G. & POINSOT, T. 2012. Large eddy simulations of gaseous flames in gas turbine combustion chambers. *Progress in Energy and Combustion Science,* 38**,** 782-817.

GOKULAKRISHNAN, P., FOLI, K., KLASSEN, M., ROBY, R., SOTERIOU, M., KIEL, B. & SEKAR, B. LES-PDF Modeling of Flame Instability and Blow-Out in Bluff-Body Stabilized Flames. 45th AIAA/ASME/SAE/ASEE Joint Propulsion Conference & Exhibit, 2009. 5409.

HAWKES, E. & CANT, R. 2000. A flame surface density approach to large-eddy simulation of premixed turbulent combustion. *Proceedings of the Combustion Institute,* 28**,** 51-58.

HODZIC, E., JANGI, M., SZASZ, R.-Z. & BAI, X.-S. 2017. Large eddy simulation of bluff body flames close to blow-off using an Eulerian stochastic field method. *Combustion and Flame,* 181**,** 1-15.

HU, Y., OLGUIN, H. & GUTHEIL, E. 2017. Transported joint probability density function simulation of turbulent spray flames combined with a spray flamelet model using a transported scalar dissipation rate. *Combustion Science and Technology,* 189**,** 322-339.

IHME, M. & PITSCH, H. 2008a. Modeling of radiation and nitric oxide formation in turbulent nonpremixed flames using a flamelet/progress variable formulation. *Physics of Fluids,* 20**,** 055110.

IHME, M. & PITSCH, H. 2008b. Prediction of extinction and reignition in nonpremixed turbulent flames using a flamelet/progress variable model: 2. Application in LES of Sandia flames D and E. *Combustion and flame,* 155**,** 90-107.

IHME, M., SHUNN, L. & ZHANG, J. 2012. Regularization of reaction progress variable for application to flamelet-based combustion models. *Journal of Computational Physics,* 231**,** 7715-7721.

JANG, D., JETLI, R. & ACHARYA, S. 1986. Comparison of the PISO, SIMPLER, and SIMPLEC algorithms for the treatment of the pressure-velocity coupling in steady flow problems. *Numerical Heat Transfer, Part A: Applications,* 10**,** 209-228.

JANGI, M., ZHAO, X., HAWORTH, D. C. & BAI, X.-S. 2015. Stabilization and liftoff length of a non-premixed methane/air jet flame discharging into a high-temperature environment: An accelerated transported PDF method. *Combustion and Flame,* 162**,** 408-419.

JANICKA, J. & SADIKI, A. 2005. Large eddy simulation of turbulent combustion systems. *Proceedings of the Combustion Institute,* 30**,** 537-547.

JARAVEL, T., RIBER, E., CUENOT, B. & PEPIOT, P. 2018. Prediction of flame structure and pollutant formation of Sandia flame D using Large Eddy Simulation with direct integration of chemical kinetics. *Combustion and Flame,* 188**,** 180-198.

JIMÉNEZ, C., CUENOT, B., POINSOT, T. & HAWORTH, D. 2002. Numerical simulation and modeling for lean stratified propane-air flames. *Combustion and Flame,* 128**,** 1-21.

JONES, W. & LINDSTEDT, R. 1988. Global reaction schemes for hydrocarbon combustion. *Combustion and flame,* 73**,** 233-249.

JONES, W., MARQUIS, A. & PRASAD, V. 2012. LES of a turbulent premixed swirl burner using the Eulerian stochastic field method. *Combustion and Flame,* 159**,** 3079-3095.

JONES, W., MARQUIS, A. & VOGIATZAKI, K. 2014. Large-eddy simulation of spray combustion in a gas turbine combustor. *Combustion and Flame,* 161**,** 222-239.

JONES, W., MARQUIS, A. & WANG, F. 2015. Large eddy simulation of a premixed propane turbulent bluff body flame using the Eulerian stochastic field method. *Fuel,* 140**,** 514-525.

JONES, W. & NAVARRO-MARTINEZ, S. 2008. Study of hydrogen auto-ignition in a turbulent air co-flow using a Large Eddy Simulation approach. *Computers & Fluids,* 37**,** 802-808.

JONES, W. & PRASAD, V. 2010. Large Eddy Simulation of the Sandia Flame Series (D–F) using the Eulerian stochastic field method. *Combustion and Flame,* 157**,** 1621-1636.

KATOPODES, F. V., STREET, R. & FERZIGER, J. Subfilter-scale scalar transport for large-eddy simulation. 14th Symposium on Boundary Layers and Turbulence, 2000a. American Meteorologic Society Aspen (CO), 472-475.

KATOPODES, F. V., STREET, R. L. & FERZIGER, J. H. 2000b. A theory for the subfilter-scale model in large-eddy simulation. *Environmental Fluid Mechanics Laboratory Tech. Rep***,** K1.

KIEL, B., GARWICK, K., GORD, J. R., MILLER, J., LYNCH, A., HILL, R. & PHILLIPS, S. 2007. A detailed investigation of bluff body stabilized flames. *AIAA Paper No. 2007-168,* 168.

KIM, J. & POPE, S. B. 2014. Effects of combined dimension reduction and tabulation on the simulations of a turbulent premixed flame using a large-

eddy simulation/probability density function method. *Combustion Theory and Modelling,* 18**,** 388-413.

KNIKKER, R., VEYNANTE, D. & MENEVEAU, C. 2004. A dynamic flame surface density model for large eddy simulation of turbulent premixed combustion. *Physics of Fluids,* 16**,** L91-L94.

KNUDSEN, E. & PITSCH, H. 2008. A dynamic model for the turbulent burning velocity for large eddy simulation of premixed combustion. *Combustion and flame,* 154**,** 740-760.

KNUDSEN, E. & PITSCH, H. 2015. Modeling partially premixed combustion behavior in multiphase LES. *Combustion and Flame,* 162**,** 159-180.

KORNEV, N. & HASSEL, E. 2007a. Method of random spots for generation of synthetic inhomogeneous turbulent fields with prescribed autocorrelation functions. *Communications in numerical methods in engineering,* 23**,** 35-43.

KORNEV, N. & HASSEL, E. 2007b. Synthesis of homogeneous anisotropic divergence-free turbulent fields with prescribed second-order statistics by vortex dipoles. *Physics of Fluids,* 19**,** 068101.

KORNEV, N., KRÖGER, H., TURNOW, J. & HASSEL, E. Synthesis of artificial turbulent fields with prescribed second‐order statistics using the random‐spot method. PAMM: Proceedings in Applied Mathematics and Mechanics, 2007. Wiley Online Library, 2100047-2100048.

KRONENBURG, A. & STEIN, O. 2017. LES-CMC of a Partially Premixed, Turbulent Dimethyl Ether Jet Diffusion Flame. *Flow, Turbulence and Combustion,* 98**,** 803-816.

KURON, M., HAWKES, E. R., REN, Z., TANG, J. C., ZHOU, H., CHEN, J. H. & LU, T. 2017. Performance of transported PDF mixing models in a turbulent premixed flame. *Proceedings of the Combustion Institute,* 36**,** 1987-1995.

LABAHN, J. W., STANKOVIĆ, I., DEVAUD, C. B. & MERCI, B. 2017. Comparative study between Conditional Moment Closure (CMC) and Conditional Source-term Estimation (CSE) applied to piloted jet flames. *Combustion and Flame,* 181**,** 172-187.

LACKMANN, T., KERSTEIN, A. & OEVERMANN, M. 2015. A Representative Interactive Linear Eddy Model (RILEM) for Non-Premixed Combustion. SAE Technical Paper.

LANGELLA, I. & SWAMINATHAN, N. 2016. Unstrained and strained flamelets for LES of premixed combustion. *Combustion Theory and Modelling,* 20**,** 410-440.

LANGELLA, I., SWAMINATHAN, N., GAO, Y. & CHAKRABORTY, N. 2015. Assessment of dynamic closure for premixed combustion large eddy simulation. *Combustion Theory and Modelling,* 19**,** 628-656.

LANGELLA, I., SWAMINATHAN, N., GAO, Y. & CHAKRABORTY, N. 2017. Large eddy simulation of premixed combustion: Sensitivity to subgrid scale velocity modeling. *Combustion Science and Technology,* 189**,** 43-78.

LAPOINTE, S. & BLANQUART, G. 2017. A priori filtered chemical source term modeling for LES of high Karlovitz number premixed flames. *Combustion and Flame,* 176**,** 500-510.

LE PICHON, T., SABEL'NIKOV, V., MOULE, Y. & COCHET, A. Assessment of a partially stirred reactor combustion model to predict the lean blow-out limit of a ramjet combustor. 18th AIAA/3AF International Space Planes and Hypersonic Systems and Technologies Conference, 2012. 5962.

LEMPKE, M., GERLINGER, P. & AIGNER, M. Assumed PDF modeling in rocket combustor simulations. Progress in Propulsion Physics, 2013. EDP Sciences, 569-582.

LEWANDOWSKI, M. T. & ERTESVÅG, I. S. 2018. Analysis of the Eddy Dissipation Concept formulation for MILD combustion modelling. *Fuel,* 224**,** 687-700.

LINDSTEDT, R. & VAOS, E. 2006. Transported PDF modeling of high-Reynolds-number premixed turbulent flames. *Combustion and Flame,* 145**,** 495-511.

LYSENKO, D. A., ERTESVÅG, I. S. & RIAN, K. E. 2014. Numerical simulations of the sandia flame d using the eddy dissipation concept. *Flow, turbulence and combustion,* 93**,** 665-687.

MA, M.-C. & DEVAUD, C. B. 2015. A Conditional Moment Closure (CMC) formulation including differential diffusion applied to a non-premixed hydrogen–air flame. *Combustion and Flame,* 162**,** 144-158.

MA, T., GAO, Y., KEMPF, A. M. & CHAKRABORTY, N. 2014. Validation and implementation of algebraic LES modelling of scalar dissipation rate for reaction rate closure in turbulent premixed combustion. *Combustion and Flame,* 161**,** 3134-3153.

MA, T., STEIN, O., CHAKRABORTY, N. & KEMPF, A. 2013. A posteriori testing of algebraic flame surface density models for LES. *Combustion Theory and Modelling,* 17**,** 431-482.

MASRI, A., DIBBLE, R. & BARLOW, R. 1996. The structure of turbulent nonpremixed flames revealed by Raman-Rayleigh-LIF measurements. *Progress in Energy and Combustion Science,* 22**,** 307-362.

MCMURTRY, P. A., GANSAUGE, T. C., KERSTEIN, A. R. & KRUEGER, S. K. 1993. Linear eddy simulations of mixing in a homogeneous turbulent flow. *Physics of Fluids A: Fluid Dynamics,* 5**,** 1023-1034.

MENON, S. & KERSTEIN, A. R. 2011. The linear-eddy model. *Turbulent Combustion Modeling.* Springer.

MÖLLER, S.-I., LUNDGREN, E. & FUREBY, C. Large eddy simulation of unsteady combustion. Symposium (International) on Combustion, 1996. Elsevier, 241-248.

MOUREAU, V., DOMINGO, P. & VERVISCH, L. 2011. From large-eddy simulation to direct numerical simulation of a lean premixed swirl flame: Filtered laminar flame-pdf modeling. *Combustion and Flame,* 158**,** 1340-1357.

MUSTATA, R., VALIÑO, L., JIMÉNEZ, C., JONES, W. & BONDI, S. 2006. A probability density function Eulerian Monte Carlo field method for large eddy simulations: application to a turbulent piloted methane/air diffusion flame (Sandia D). *Combustion and Flame,* 145**,** 88-104.

NAMBULLY, S., DOMINGO, P., MOUREAU, V. & VERVISCH, L. 2014. A filtered-laminar-flame PDF sub-grid-scale closure for LES of premixed turbulent flames: II. Application to a stratified bluff-body burner. *Combustion and Flame,* 161**,** 1775-1791.

NAVARRO-MARTINEZ, S. & KRONENBURG, A. 2009. LES–CMC simulations of a lifted methane flame. *Proceedings of the Combustion Institute,* 32**,** 1509-1516.

NAVARRO-MARTINEZ, S., KRONENBURG, A. & DI MARE, F. 2005. Conditional moment closure for large eddy simulations. *Flow, Turbulence and Combustion,* 75**,** 245-274.

OEVERMANN, M., SCHMIDT, H. & KERSTEIN, A. 2008. Investigation of autoignition under thermal stratification using linear eddy modeling. *Combustion and Flame,* 155**,** 370-379.

PARENTE, A., MALIK, M. R., CONTINO, F., CUOCI, A. & DALLY, B. B. 2016. Extension of the Eddy Dissipation Concept for turbulence/chemistry interactions to MILD combustion. *Fuel,* 163**,** 98-111.

PARK, N. S. & KO, S. C. 2011. Large eddy simulation of turbulent premixed combustion flow around bluff body. *Journal of mechanical science and technology,* 25**,** 2227.

PERRY, B. A., MUELLER, M. E. & MASRI, A. R. 2017. A two mixture fraction flamelet model for large eddy simulation of turbulent flames with inhomogeneous inlets. *Proceedings of the Combustion Institute,* 36**,** 1767-1775.

PETERS, N. & ROGG, B. 2008. *Reduced kinetic mechanisms for applications in combustion systems*, Springer Science & Business Media.

PHILIP, M., BOILEAU, M., VICQUELIN, R., RIBER, E., SCHMITT, T., CUENOT, B., DUROX, D. & CANDEL, S. 2015. Large Eddy Simulations of the ignition sequence of an annular multiple-injector combustor. *Proceedings of the Combustion Institute,* 35**,** 3159-3166.

PITSCH, H. & DE LAGENESTE, L. D. 2002. Large-eddy simulation of premixed turbulent combustion using a level-set approach. *Proceedings of the Combustion Institute,* 29**,** 2001-2008.

PITSCH, H. & STEINER, H. 2000. Large-eddy simulation of a turbulent piloted methane/air diffusion flame (Sandia flame D). *Physics of fluids,* 12**,** 2541-2554.

POINSOT, T. & VEYNANTE, D. 2005. *Theoretical and numerical combustion*, RT Edwards, Inc.

POPE, S. B. 2001. *Turbulent flows*, IOP Publishing.

PORUMBEL, I. & MENON, S. 2006. Large eddy simulation of bluff body stabilized premixed flame. *AIAA paper*.

PRASAD, V. N. 2011. Large Eddy Simulation of partially premixed turbulent combustion.

PROCH, F., DOMINGO, P., VERVISCH, L. & KEMPF, A. M. 2017. Flame resolved simulation of a turbulent premixed bluff-body burner experiment. Part II: A-priori and a-posteriori investigation of sub-grid scale wrinkling closures in the context of artificially thickened flame modeling. *Combustion and Flame,* 180**,** 340-350.

RAMAN, V. & PITSCH, H. 2007. A consistent LES/filtered-density function formulation for the simulation of turbulent flames with detailed chemistry. *Proceedings of the Combustion Institute,* 31**,** 1711-1719.

REYNOLDS, O. 1883. XXIX. An experimental investigation of the circumstances which determine whether the motion of water shall he direct or sinuous, and of the law of resistance in parallel channels. *Philosophical Transactions of the Royal Society of London,* 174**,** 935-982.

RIETH, M., CLEMENTS, A., RABAÇAL, M., PROCH, F., STEIN, O. & KEMPF, A. 2017. Flamelet LES modeling of coal combustion with detailed devolatilization by directly coupled CPD. *Proceedings of the Combustion Institute,* 36**,** 2181-2189.

ROCHETTE, B., COLLIN-BASTIANI, F., GICQUEL, L., VERMOREL, O., VEYNANTE, D. & POINSOT, T. 2018. Influence of chemical schemes, numerical method and dynamic turbulent combustion modeling on LES of premixed turbulent flames. *Combustion and Flame,* 191**,** 417-430.

ROOMINA, M. & BILGER, R. 2001. Conditional moment closure (CMC) predictions of a turbulent methane-air jet flame. *Combustion and Flame,* 125**,** 1176-1195.

ROY, R. N., KUMAR, S. & SREEDHARA, S. 2015. Predictions of lift-off height of turbulent methane and propane flames issuing in cold surroundings

using conditional moment closure coupled with an extinction model. *Combustion and Flame,* 162**,** 1164-1166.

SAGHAFIAN, A., SHUNN, L., PHILIPS, D. A. & HAM, F. 2015. Large eddy simulations of the HIFiRE scramjet using a compressible flamelet/progress variable approach. *Proceedings of the Combustion Institute,* 35**,** 2163-2172.

SALEHI, F., TALEI, M., HAWKES, E. R., BHAGATWALA, A., CHEN, J. H., YOO, C. S. & KOOK, S. 2017. Doubly conditional moment closure modelling for HCCI with temperature inhomogeneities. *Proceedings of the Combustion Institute,* 36**,** 3677-3685.

SALEHI, F., TALEI, M., HAWKES, E. R., YOO, C. S., LUCCHINI, T., D'ERRICO, G. & KOOK, S. 2015. Conditional moment closure modelling for HCCI with temperature inhomogeneities. *Proceedings of the Combustion Institute,* 35**,** 3087-3095.

SALEHI, M. M., BUSHE, W. K., SHAHBAZIAN, N. & GROTH, C. P. 2013. Modified laminar flamelet presumed probability density function for LES of premixed turbulent combustion. *Proceedings of the Combustion Institute,* 34**,** 1203-1211.

SANKARAN, V., PALIES, P., LILJENBERG, S., TEERLINCK, K. & SOTERIOU, M. Stabilization dynamics of bluff-body premixed flames. 50th AIAA Aerospace Sciences Meeting including the New Horizons Forum and Aerospace Exposition, 2012. 352.

SCHNEIDER, C., DREIZLER, A., JANICKA, J. & HASSEL, E. 2003. Flow field measurements of stable and locally extinguishing hydrocarbon-fuelled jet flames. *Combustion and Flame,* 135**,** 185-190.

SCHNEIDER, E., SADIKI, A. & JANICKA, J. 2005. Modeling and 3D-simulation of the kinetic effects in the post-flame region of turbulent premixed flames based on the G-equation approach. *Flow, turbulence and combustion,* 75**,** 191.

SEE, Y. C. & IHME, M. 2015. Large eddy simulation of a partially-premixed gas turbine model combustor. *Proceedings of the Combustion Institute,* 35**,** 1225-1234.

SEWERIN, F. & RIGOPOULOS, S. 2018. An LES-PBE-PDF approach for predicting the soot particle size distribution in turbulent flames. *Combustion and Flame,* 189**,** 62-76.

SHANBHOGUE, S. J., HUSAIN, S. & LIEUWEN, T. 2009. Lean blowoff of bluff body stabilized flames: Scaling and dynamics. *Progress in Energy and Combustion Science,* 35**,** 98-120.

SHEIKHI, M., DROZDA, T., GIVI, P., JABERI, F. & POPE, S. 2005. Large eddy simulation of a turbulent nonpremixed piloted methane jet flame (Sandia Flame D). *Proceedings of the Combustion Institute,* 30**,** 549-556.

SJUNNESSON, A., NELSSON, C. & MAX, E. 1991a. LDA measurements of velocities and turbulence in a bluff body stabilized flame. *Laser Anemometry,* 3**,** 83-90.

SJUNNESSON, A., OLOVSSON, S. & SJOBLOM, B. Validation rig- A tool for flame studies. International Symposium on Air Breathing Engines, 10 th, Nottingham, England, 1991b. 385-393.

STÖLLINGER, M. & HEINZ, S. 2008. PDF modeling and simulation of premixed turbulent combustion. *Monte Carlo Methods and Applications,* 14**,** 343-377.

TRIANTAFYLLIDIS, A., MASTORAKOS, E. & EGGELS, R. 2009. Large Eddy Simulations of forced ignition of a non-premixed bluff-body methane flame with Conditional Moment Closure. *Combustion and Flame,* 156**,** 2328-2345.

TSUI, H. & BUSHE, W. 2014. Linear-eddy model formulated probability density function and scalar dissipation rate models for premixed combustion. *Flow, turbulence and combustion,* 93**,** 487-503.

VILLASENOR, R., CHEN, J.-Y. & PITZ, R. 1992. Modeling ideally expanded supersonic turbulent jet flows with nonpremixed H2-air combustion. *AIAA journal,* 30**,** 395-402.

VOLPIANI, P., SCHMITT, T. & VEYNANTE, D. 2016. A posteriori tests of a dynamic thickened flame model for large eddy simulations of turbulent premixed combustion. *Combustion and Flame,* 174**,** 166-178.

VOLPIANI, P. S., SCHMITT, T., VERMOREL, O., QUILLATRE, P. & VEYNANTE, D. 2017. Large eddy simulation of explosion deflagrating flames using a dynamic wrinkling formulation. *Combustion and Flame,* 186**,** 17-31.

VREMAN, A., ALBRECHT, B., VAN OIJEN, J., DE GOEY, L. & BASTIAANS, R. 2008. Premixed and nonpremixed generated manifolds in large-eddy simulation of Sandia flame D and F. *Combustion and Flame,* 153**,** 394-416.

VREMAN, A., VAN OIJEN, J., DE GOEY, L. & BASTIAANS, R. 2009. Subgrid scale modeling in large-eddy simulation of turbulent combustion using premixed flamelet chemistry. *Flow, Turbulence and Combustion,* 82**,** 511-535.

WANG, G., BOILEAU, M. & VEYNANTE, D. 2011. Implementation of a dynamic thickened flame model for large eddy simulations of turbulent premixed combustion. *Combustion and Flame,* 158**,** 2199-2213.

WANG, H. & KIM, K. 2015. Effect of molecular transport on PDF modeling of turbulent non-premixed flames. *Proceedings of the Combustion Institute,* 35**,** 1137-1145.

WELLER, H. G., TABOR, G., JASAK, H. & FUREBY, C. 1998. A tensorial approach to computational continuum mechanics using object-oriented techniques. *Computers in physics,* 12**,** 620-631.

XIAO, G., JIA, M. & WANG, T. 2016. Large eddy simulation of n-heptane spray combustion in partially premixed combustion regime with linear eddy model. *Energy,* 97**,** 20-35.

YADAV, R., KUSHARI, A., ESWARAN, V. & VERMA, A. K. 2013. A numerical investigation of the Eulerian PDF transport approach for modeling of turbulent non-premixed pilot stabilized flames. *Combustion and Flame,* 160**,** 618-634.

ZETTERVALL, N., NORDIN-BATES, K., NILSSON, E. & FUREBY, C. 2017. Large Eddy Simulation of a premixed bluff body stabilized flame using global and skeletal reaction mechanisms. *Combustion and Flame,* 179**,** 1-22.

ZHANG, H., GARMORY, A., CAVALIERE, D. E. & MASTORAKOS, E. 2015. Large Eddy Simulation/Conditional Moment Closure modeling of swirl-stabilized non-premixed flames with local extinction. *Proceedings of the Combustion Institute,* 35**,** 1167-1174.

ZHANG, P. & WANG, H. 2018. Variance consistent mean shift particle model for treating differential molecular diffusion in transported PDF methods for turbulent reactive flows. *Computers & Fluids,* 170**,** 53-76.

ZHAO, W. 2017. Large-eddy simulation of piloted diffusion flames using multi-environment probability density function models. *Proceedings of the Combustion Institute,* 36**,** 1705-1712.